



Contents lists available at ScienceDirect

Progress in Materials Science

journal homepage: www.elsevier.com/locate/pmatsci



Recent advances in bismuth activated photonic materials



Hong-Tao Sun ^{a,b,*}, Jiajia Zhou ^{c,d,*}, Jianrong Qiu ^{e,*}

^a College of Chemistry, Chemical Engineering and Materials Science, Soochow University, Suzhou 215123, China

^b Division of Materials Science and Engineering, Faculty of Engineering, Hokkaido University, Kita 13, Nishi 8, Kita-ku, Sapporo 060-8628, Japan

^c College of Materials Science and Engineering, China Jiliang University, Hangzhou 310018, China

^d State Key Laboratory of Silicon Materials, Zhejiang University, Hangzhou 310027, China

^e State Key Laboratory of Luminescent Materials and Devices, South China University of Technology, Guangzhou 510640, China

ARTICLE INFO

Article history:

Received 18 January 2013

Accepted 2 February 2014

Available online 5 March 2014

ABSTRACT

Bismuth is one of the most thoroughly investigated main group elements, which has been regarded as 'the wonder metal' because of its diverse oxidation states and profound propensities to form bismuth clusters, resulting from the easy involvement in chemical combinations for the electrons in the p orbital. This peculiarity allows them to behave as smart optically active centers in diverse host materials. Remarkable progress in the research of bismuth activated photonic materials has been seen over the last ten years owing to their unique properties and important applications in areas of telecommunication, biomedicine, white light illumination and lasers. The aim of this review is to present a critical overview of the current state of the art in bismuth activated photonic materials, their features, advantages and limitations as well as the future research trends. We first shortly introduce the fundamental properties of bismuth element including principles of bismuth-related luminescence and characterization techniques available. This is followed by a detailed discussion on the recent progress in the synthesis and characterization of bismuth-activated photonic materials, with an emphasis on material systems emitting in the near-infrared (NIR) spectral region. Furthermore, we describe the representative achievements regarding their prospective applications in broadband NIR optical amplifiers, fiber lasers,

* Corresponding authors. Addresses: College of Chemistry, Chemical Engineering and Materials Science, Soochow University, Suzhou 215123, China (H.-T. Sun), College of Materials Science and Engineering, China Jiliang University, Hangzhou 310018, China (J. Zhou). Tel.: +86 512 6588 2687.

E-mail addresses: timothyhsun@gmail.com (H.-T. Sun), zhzz85@163.com (J. Zhou), qjr@zju.edu.cn (J. Qiu).

bioimaging, and white light-emitting diodes. Finally, we point out what key scientific questions remain to be answered, and present our perspectives on future research trends in this exciting field of sciences.

© 2014 Elsevier Ltd. All rights reserved.

Contents

1. Introduction	3
2. Principles of Bi luminescence	4
3. Synthesis and characterization of Bi doped materials	10
3.1. Synthesis of Bi doped materials	10
3.1.1. Solid state reaction	11
3.1.2. Liquid phase reaction	11
3.1.3. Vapor deposition method	12
3.1.4. Melt-quenching method	13
3.1.5. Vacuum-annealing method	13
3.2. Characterization techniques for Bi	13
3.2.1. X-ray techniques	13
3.2.2. NMR and ESR spectroscopy	15
3.2.3. Photoluminescence spectroscopy	16
3.2.4. Quantum chemistry calculations	16
4. Bi doped visible emitting materials	17
4.1. Bi ³⁺ doped crystals and glasses	17
4.2. Bi ²⁺ doped crystals	18
4.2.1. Strontium tetraborate	18
4.2.2. Borophosphate	19
4.2.3. Strontium phosphate	19
5. Bi doped near-infrared (NIR) emitting materials	21
5.1. Subvalent Bi in liquids	21
5.2. Bi doped amorphous solids	23
5.2.1. Bulk glasses	23
5.2.2. Glass fibers	28
5.2.3. Glass films	30
5.2.4. Amorphous nanoparticles	33
5.3. Bi doped crystalline materials	35
5.3.1. Halide crystals	35
5.3.2. Zeolites crystals	38
5.3.3. Oxide crystals	43
5.4. Molecular crystals containing Bi polyhedra	46
5.5. NIR PL origin: challenges and chances	50
6. Applications	52
6.1. Broadband NIR optical amplifiers	52
6.2. Fiber laser	55
6.2.1. New wavelength laser	55
6.2.2. Tunable fiber laser	56
6.2.3. Pulsed fiber laser	57
6.3. Bioimaging	60
6.4. Phosphors for LEDs	62
7. Conclusions and outlook	64
Acknowledgements	65
References	65

Nomenclature

ILMs	inorganic luminescent materials
RE	rare earth
TM	transition metal
LEDs	light-emitting diodes
WLED	white light-emitting diode
PL	photoluminescence
PLE	photoluminescence excitation
NIR	near-infrared
HF	Hartree–Fock
HFS	Hartree–Fock–Slater
XPS	X-ray photoelectron spectroscopy
XRD	X-ray diffraction
EXAFS	extended X-ray absorption fine structure
XANES	X-ray absorption near edge structure
XAS	X-ray absorption spectroscopy
NMR	nuclear magnetic resonance
ESR	electron spin resonance
PVD	physical vapor deposition
CVD	chemical vapor deposition
MCVD	modified chemical vapor deposition
BE	binding energy
ILs	ionic liquids
FWHM	the full width at half maximum
ADF	Amsterdam Density Functional
DFAs	doped fiber amplifiers
EDFA	erbium doped fiber amplifier
CRI	color rendering index

1. Introduction

The development of inorganic luminescent materials (ILMs) that can overcome the intrinsic limitations of organic fluorophores is an area of considerable current interest across a number of science, engineering and biomedical disciplines [1]. ILMs activated by a small amount of dopants such as rare earth (RE) and transition metal (TM) ions, have received extensive attention and achieved fundamental improvements and novel developments during the past years [2,3]. These materials can be found in a wide range of every-day applications such as fluorescent tubes, white LEDs (light-emitting diodes), plasma displays, scintillators, optical amplifiers, lasers and bioimaging. However, improvements over the last decades have led to above materials operating close to their physical limits. It is not expected that the properties such as the luminescence quantum yield and chemical stability will be significantly improved or that distinctly better materials will be developed in the near future.

Heavier main-group elements have fundamentally different electronic properties from their lighter congeners. Bismuth, with the electronic configuration of $(Xe)4f^{14}5d^{10}6s^26p^3$, is one of the most thoroughly investigated main-group elements, which has been known as ‘the wonder metal’ owing to the easy involvement in chemical combinations for the electrons in its p orbital [4]. Bi exhibits three apparent features as follows: (i) Bi shows a variety of oxidation states such as 0, +1, +2, +3, +5, characterized by multi-type electronic structures. The electrons in the 6p, 6s, or 5d orbital of Bi are rather sensitive to their coordination environments [5]; (ii) Bi shows a profound propensity to form clusters, which widely exist in molten Lewis acids [6–10], molecular crystals [11–36] or porous zeolitic solids [37]; (iii) Bi shows strong spin-orbit coupling effect. These peculiarities allow them to behave as smart optically active centers in diverse host materials [38–41]. Materials activated by Bi display abundant

luminescence characteristics different from the traditional active centers such as lanthanide and TMs. The interest in the photoluminescence (PL) of bismuth-activated photonic materials has thus grown considerably during the last decade, with the concomitant design of novel materials with tunable attributes and modulated properties. This opens up new research directions in materials science and related technologies and has significant implications in developing new photonic materials. Up to now, research work has been disclosed gradually and towards distinct purposes ranging from fundamental aspects of the Bi spectroscopy (e.g., controlling Bi valence states and explaining the related PL mechanism) to the synthesis of novel material systems and the fabrication of functional devices. During the past several years, promising applications of these materials have been successfully demonstrated, such as broadband optical amplifiers, fiber lasers, bioimaging, and phosphors.

The aim of this review is to give a critical overview of different types of bismuth-activated photonic materials, their features, advantages and limitations as well as the future research trends. The literature has been covered until January 2013. We first shortly introduce the principles of Bi luminescence and discuss the characterization techniques available for Bi. This is followed by detailed discussions on the recent progress in the synthesis and characterization of photonic materials activated by Bi^{3+} and Bi^{2+} . Subsequently, we would lay particular emphasis on bismuth-doped near-infrared (NIR) emitting materials, considering the rapid advances in their synthesis and applications over the past ten years as well as highly scientific and technological importance for developing novel photonic materials in the near future. Furthermore, we describe the representative achievements regarding their prospective applications, such as broadband optical amplifiers, fiber lasers, bioimaging, and phosphors. In the last section, we would point out key scientific questions to be answered and present our perspectives on the future research trends for this exciting field of sciences.

2. Principles of Bi luminescence

Bismuth, the heaviest stable element in the periodic table, was first discovered as early as the 15th century, and was established as an element in 1739 by Potts and Bergmann [42], which is most commonly found in nature as the oxide (Bi_2O_3), carbonate ($(\text{BiO})_2\text{CO}_3$) and sulfide (Bi_2S_3), and is also produced as a byproduct of lead, zinc, tungsten and copper mining [43]. Bismuth element has the electronic configuration of $(\text{Xe})4f^{14}5d^{10}6s^26p^3$, whose outer 6s and 6p electrons are valence electrons. Owing to this, Bi element can show multi-type oxidation states such as 0 (outermost electrons: $6p^3$), +1 ($6p^2$), +2 ($6p^1$), +3 ($6s^2$), and +5 ($5d^{10}$). One of the most important features of these ions, especially for Bi^+ , Bi^{2+} , and Bi^{3+} , is their luminescence in the visible or NIR spectral region when excited by ultraviolet, visible or NIR optical sources, arising from their multiplex electronic structures. In general, the absorption and emission bands for Bi^+ , Bi^{2+} , and Bi^{3+} are much broader than those of f-f transitions of RE $^{3+}$, owing to the unsheltered outer electrons. This gives plenty of opportunities for further tuning the spectroscopic characteristics of Bi through rational selection of host materials, facile control of synthesis factors and post-treatments under suitable conditions.

It is well known that Bi^{3+} is the most common and most stable ionic form, in contrast to Bi^+ and Bi^{2+} [5], which exists in a wide range of materials including inorganic crystals (e.g., GaBO_3), glasses (e.g., germanate glass) and organic compounds (e.g., $[\text{Bi}(\text{OC}_2\text{H}_5)_3]$ and $[\text{Bi}(\text{O}-\text{C}_3\text{H}_7)_3]$) [44–52]. The spectroscopy of Bi^{3+} ion which has the $6s^2$ electronic configuration has been investigated extensively in a variety of host lattices. The ground state of the free ion is ${}^1\text{S}_0$, whereas the $6s6p$ excited states give rise to the triplet levels $[{}^3\text{P}_0, {}^3\text{P}_1, {}^3\text{P}_2]$ and the ${}^1\text{P}_1$ singlet state (Fig. 1). The ${}^1\text{S}_0 \rightarrow {}^3\text{P}_0$ is strongly forbidden whereas the ${}^1\text{S}_0 \rightarrow {}^3\text{P}_1$ transition becomes allowed as a result of the spin-orbit coupling that takes place between ${}^3\text{P}_1$ and ${}^1\text{P}_1$. The ${}^1\text{S}_0 \rightarrow {}^3\text{P}_2$ transition is spin-forbidden, which can be allowed by coupling with unsymmetrical lattice vibrational modes; the ${}^1\text{S}_0 \rightarrow {}^1\text{P}_1$ transition is an allowed transition. Bi^{3+} doped materials usually display broad absorption bands in the UV region. The allowed higher energy transition of ${}^1\text{S}_0 \rightarrow {}^1\text{P}_1$ is appropriately $10,000 \text{ cm}^{-1}$ separation in comparison with ${}^1\text{S}_0 \rightarrow {}^3\text{P}_1$ transition, placing near $45,700 \text{ cm}^{-1}$. The absorption bands in the range of 250–400 nm are closely related to the transitions of ${}^1\text{S}_0 \rightarrow {}^3\text{P}_0$ and ${}^1\text{S}_0 \rightarrow {}^3\text{P}_1$ [5]. Luminescence spectrum of Bi^{3+} shows a rather broad blue or green bands ranging from 400 to 600 nm. The full width at the half maximum (FWHM) of the emissions could be as large as 0.54 eV, comparable to other type of s^2-sp transition such as Pb^{2+} ,

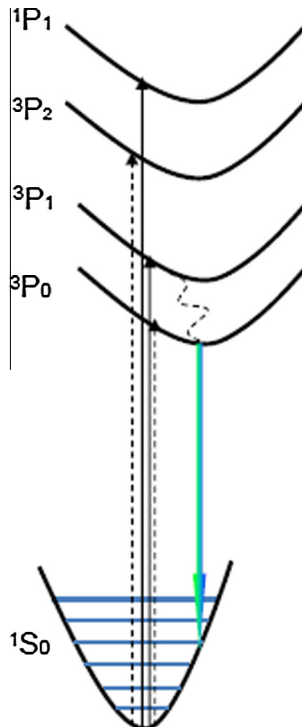


Fig. 1. The configurational coordinate model used to interpret the absorption and emission processes of Bi^{3+} . The horizontal line represents the vibrational levels in each electronic state. The solid and dash vertical lines with up arrows represent the spin allowed and forbidden electronic transitions, respectively. The dash curve and solid line with down arrow represent the nonradiative process from ${}^3\text{P}_1$ to ${}^3\text{P}_0$ and radiative blue or green emission, respectively.

Sn^{2+} , and Sb^{3+} while much broader than those of RE^{3+} . The characteristics of broad absorption and emission bands can be well explained with the configurational coordinate energy diagram (Fig. 1). The potential energy curve of Bi^{3+} in the lattice can be plotted as a function of the distance r between the central cation and surrounding anions. In the potential energy diagram, the coordinate of the excited state minimum is shifted relative to that of the ground state minimum. This shift is very large for $s^2-\text{sp}$ transition, and the excited p state is much wider than the ground s state, thus resulting in such kind of broad emission.

In addition to blue or green emission band from Bi doped materials, it is interesting to note that a narrow orange band was first reported for synthetic $\text{BaSO}_4:\text{Bi}$ in 1886 by Locoq de Buisbaudran [5], but for a long time the PL mechanism was not clear. A century later a convincing interpretation has been done by Hamstra et al. and it was assumed that the luminescence is from Bi^{2+} [53], which has the same $6s^26p^1$ electronic configuration same with those of Tl^{10} and Pb^+ . The detailed time-resolved laser-induced luminescence of $\text{BaSO}_4:\text{Bi}$ suggests that the narrow orange band with a lifetime of 5 μs is closely connected with Bi^{2+} center [54]. In an attempt to further clarify the connection of orange band with Bi^{2+} or Bi^{3+} , Gaft et al. used a step-like thermal treatment of nature barite in air in order to stimulate Bi oxidation with possible change of valence state. It was observed that the narrow orange emission totally disappears after thermal treatment at 700 °C. This, in combination with the time-resolved luminescence results, evidenced that Bi^{2+} contributes to the orange luminescence. Systematical studies done in recent years clearly revealed that Bi^{2+} ion widely exists in crystalline hosts such as SrB_4O_7 [39], $\text{M}^{2+}\text{BPO}_5$ ($\text{M} = \text{Ba}, \text{Sr}, \text{Ca}$) [55], $\text{SrB}_6\text{O}_{10}$ [56], and $\text{Sr}_2\text{P}_2\text{O}_7$ [57]. Its electronic configuration yields a ${}^2\text{P}_{1/2}$ ground state and a ${}^2\text{P}_{3/2}$ excited state. Bi^{2+} displays three UV-vis excitation bands resulting from the electronic transitions of ${}^2\text{P}_{1/2} \rightarrow {}^2\text{P}_{3/2}(1)$, ${}^2\text{P}_{1/2} \rightarrow {}^2\text{P}_{3/2}(2)$ and ${}^2\text{P}_{1/2} \rightarrow {}^2\text{S}_{1/2}$ (Fig. 2). Because

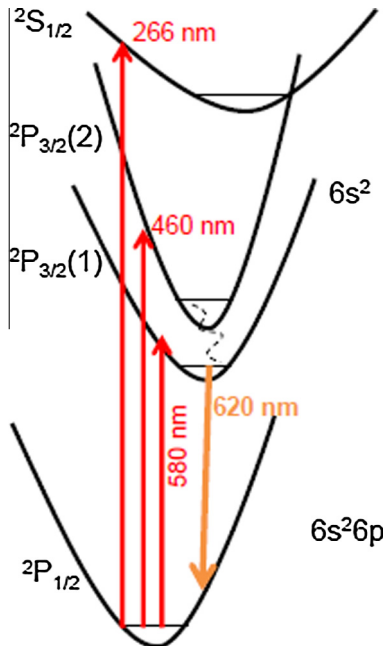


Fig. 2. Configurational coordinate diagram showing emission and excitation transitions of Bi^{2+} .

$2\text{P}_{3/2} \rightarrow 2\text{P}_{1/2}$ transition is interconfigurational, it is formally parity forbidden, which agrees well with the relatively longer luminescence lifetimes.

In comparison to Bi^{3+} and Bi^{2+} , Bi^+ is relatively unstable and can only exist in some peculiar material systems. The synthesis and characterization of materials containing Bi^+ date back to half a century ago [6,8,9,58–60]. In an early work on the investigation of the phase diagram of the bismuth-bismuth trichloride system, Topol et al. first proposed that Bi^+ exists in the molten salts based on the electrochemical measurement [58]. Smith and co-workers systematically studied the host-dependent photophysical properties of Bi containing molten salts by means of spectroscopic analysis, which supports well that Bi^+ could absorb lights in the UV-vis-NIR spectral ranges [59,60]. In molten salts, the ligands coordinated to Bi^+ have not been known but almost certainly they are either halide or haloaluminate ions. Bi^+ has the electronic configuration of $(\text{Xe})4\text{f}^{14}5\text{d}^{10}6\text{s}^26\text{p}^2$, whose electronic property strongly depends on the local environment in the matrices. It has been found that in $\text{AlCl}_3\text{-NaCl}$ molten salt Bi^+ displays characteristic absorption bands peaking at 32500, 30,000, 17,100, 15,200, 14,400, and $11,100 \text{ cm}^{-1}$, whereas in $\text{AlBr}_3\text{-NaBr}$ molten salts these bands are red-shifted (Fig. 3) [8]. In recent several years, the PL of Bi^+ has been investigated in details owing to its tunable and ultra-broadband NIR emission covering the important telecommunication and biological optical windows. It was reported that NIR luminescent Bi^+ can exist in ionic liquid [61] and glass hosts such as $\text{AlCl}_3\text{/ZnCl}_2\text{/BiCl}_3$ glass [62]. Although the spectroscopic properties of Bi^+ have been investigated for several decades, the exact local environment of Bi^+ has not been identified in almost all material systems reported, which greatly hinders the deep understanding of the observed experimental results. Besides the experimental work on Bi^+ , some theoretical considerations have also been made. Keller et al. employed relativistic Hartree-Fock (rel HF) and relativistic Hartree-Fock-Slater (rel HFS) methods to calculate electronic energy levels, ionization potentials, promotion energies to excited states, and atomic and ionic radii of group 15 elements [63]. They estimated that Bi^+ should possess an ionic radius of ca. 1.5 \AA , which is similar to that experimentally determined value (i.e., 1.45 \AA) [64]. In a recent report, it was found that nanoporous materials such as zeolites are excellent templates for obtaining Bi^+ ion [37], which could demonstrate peculiar NIR emission bands because of the intrinsic electronic transitions of Bi^+ substructures.

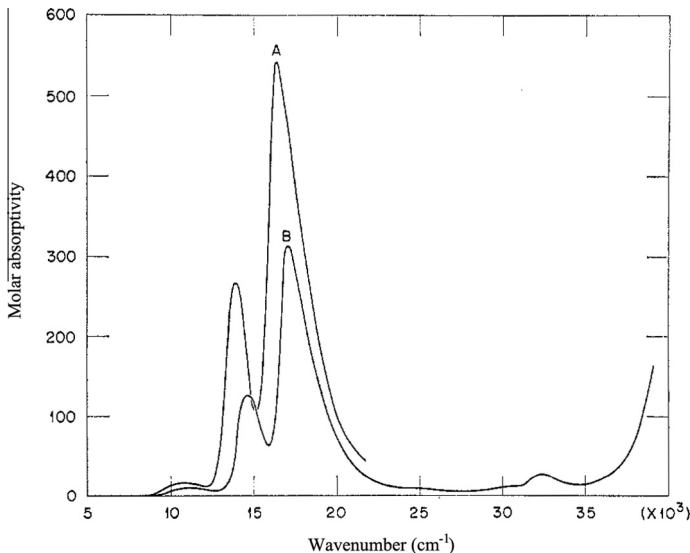


Fig. 3. Absorption spectra of Bi^+ in haloaluminate media. (A) Solvent was molten $\text{AlBr}_3\text{-NaBr}$ eutectic at 250°C . (B) Solvent was molten $\text{AlCl}_3\text{-NaCl}$ eutectic at 310°C . Reproduced with permission from Ref. [8]. Copyright © 1967, American Chemical Society.

All the aforementioned Bi active centers are based on single Bi ion with different oxidation state (i.e., Bi^{3+} , Bi^{2+} , or Bi^+), the formation of which is closely related to the host materials used. It is noteworthy that Bi can form a broad range of positively charged polyhedra, whose structures can be well predicted by polyhedral skeletal electron pair approach [65]. Up till now, many kinds of molecular crystals containing Bi polycations such as Bi_5^{3+} , Bi_6^{2+} , and Bi_8^{2+} , have been identified and systematically characterized [7,11–37]. In general, these materials were synthesized either by molten-salt route or by using superacidic systems, and complex anions, such as $[\text{AlCl}_4]^-$, $[\text{AsF}_6]^-$, and $[\text{HfCl}_6]^{2-}$, act as counterions in crystals (Fig. 4). These Bi polyhedra with different structures and charges display diverse

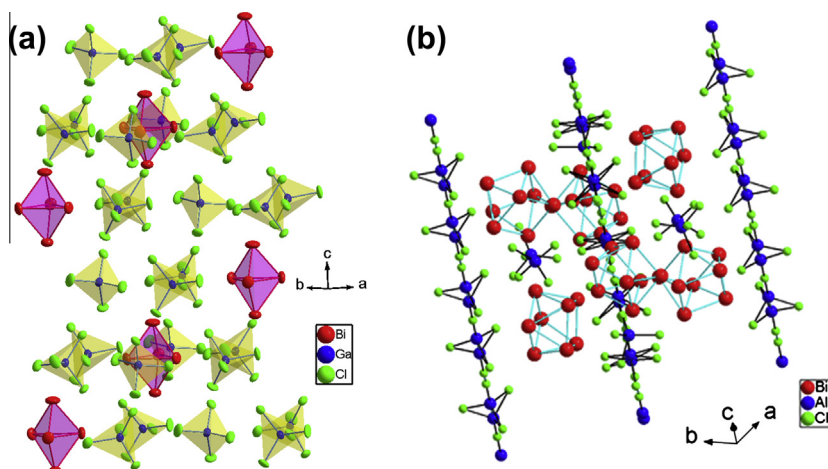


Fig. 4. (a) The crystal structure of $\text{Bi}_5(\text{GaCl}_4)_3$ consisting of triagonal bipyramidal Bi_5^{3+} clusters and tetrahedral $[\text{GaCl}_4]^-$ units. (b) The crystal structure of $\text{Bi}_8(\text{AlCl}_4)_2$ consisting of Bi_8^{2+} polycations and tetrahedral $[\text{AlCl}_4]^-$ anions. Reproduced with permission from Ref. [34,35]. Copyright © 2012, Royal Chemical Society.

photophysical properties inherently different from single Bi active center, which greatly enrich Bi-related electronic structures and present new chances to design and synthesize new applicable material systems. Spectroscopic measurements revealed that Bi_5^{3+} either in molten salts or molecular crystals has broad absorption bands in UV-vis-NIR region [9,33–35]. Furthermore, detailed PL evaluation indicated that Bi_5^{3+} stabilized by $[\text{AlCl}_4]^-$ or $[\text{GaCl}_4]^-$ can convert the absorbed high-energy photons to longer wavelengths, giving rise to the ultrabroad emission ranging from 1 to $2.7\ \mu\text{m}$ [34,35,66]. In contrast, Bi_8^{3+} with an average oxidation state of +0.25 displays broad NIR emission peaking at ca. $1180\ \text{nm}$ [34]. The most attractive advantage of such charged Bi units lies in their broad PL covering the telecommunication and/or biological optical windows or even extending over $2\ \mu\text{m}$.

In addition to positively charged Bi polyhedra, Bi units with negative charges, termed as Zintl ions, represent another intriguing class of systems, which have been intensively studied over the past decades [26–30,67]. To obtain high-quality crystalline materials from Zintl ion-containing solutions, alkali-metal-ion-sequestering agents, such as [2.2.2] crypt were employed by Corbett [68]. The smallest homoatomic Bi polyanion obtained from solution is the dumbbell-shaped $[\text{Bi}_2]^{2-}$, whose charges are balanced by two $[\text{K-crypt}]^+$ cations [26,69] (Fig. 5). Recent results revealed that $[\text{Bi}_2]^{2-}$ could result in broad NIR emission peaking at ca. $1.19\ \mu\text{m}$ [69]. It is worth to note that many of these compounds with Bi polyanions absorb light in the visible range of the electromagnetic spectrum since they are colored, thus giving promise for unique optical properties. To make a deep understanding of the observed photophysical properties of Bi polyanions, great effort on the calculation of their theoretical electronic structures using state-of-the-art quantum chemistry codes has been made. Dai et al. first calculated the theoretical excitation energies of $[\text{Bi}_2]^{2-}$ with $d(\text{Bi-Bi}) = 2.8377\ \text{\AA}$ in $(\text{K-crypt})_2\text{Bi}_2$ using the Beijing density function program, and revealed that the anion should possess at least four excitation bands located at around 1380 , 1062 , 562 , and $399\ \text{nm}$ [28]. In a subsequent work, Sokolov et al. calculated the excitation energies of $[\text{Bi}_2]^{2-}$ using the Gamess (US) quantum-chemical code [70]. The calculated results showed that several transitions from the $^3\text{I}_{1g}$ ground state to the $^3\Sigma$ excited states are allowed and correspond to absorption bands near 880 , 715 , 470 , and below $400\ \text{nm}$ (Fig. 6). Furthermore, it was shown that NIR luminescence bands with wavelengths 1420 – 1520 , 1275 – 1375 , and 1000 – $1060\ \text{nm}$ should occur due to spin-forbidden transitions from three $^1\Sigma$ singlet excited states to ^3I ground state and/or to one of the first two excited ^3I states. Although at present the theoretical results are not totally consistent with the observed facts [69], it is clear that such calculations, in a sense, allow us to roughly predict the photophysical properties of such charged heavy units. By successful combination of theoretical and experimental work, it is believed that more interesting and applicable material systems could be developed.

Until now, extensive studies have been carried out to synthesize and characterize Bi activated materials, and functional applications in fiber lasers [71], bioimaging [72], and phosphors [54–57] have been demonstrated. However, over the past decades other Bi active centers have also been reported in some peculiar systems. Usually, such emitters were termed as Bi molecules or radicals

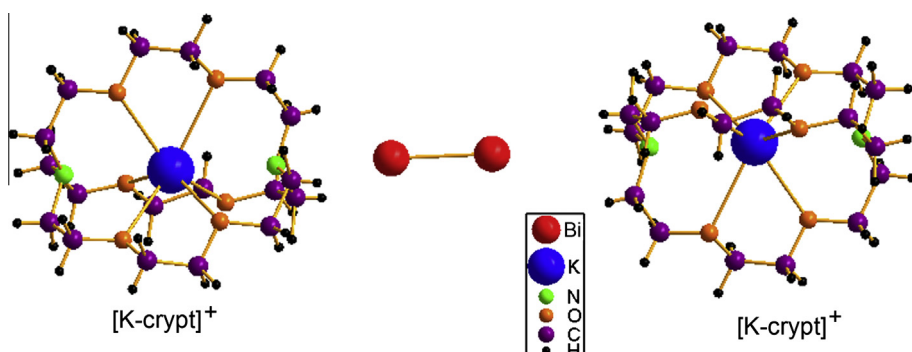


Fig. 5. Part of the structure of $(\text{K-crypt})_2\text{Bi}_2$. Reproduced with permission from Ref. [69]. Copyright © 2012, Royal Chemical Society.

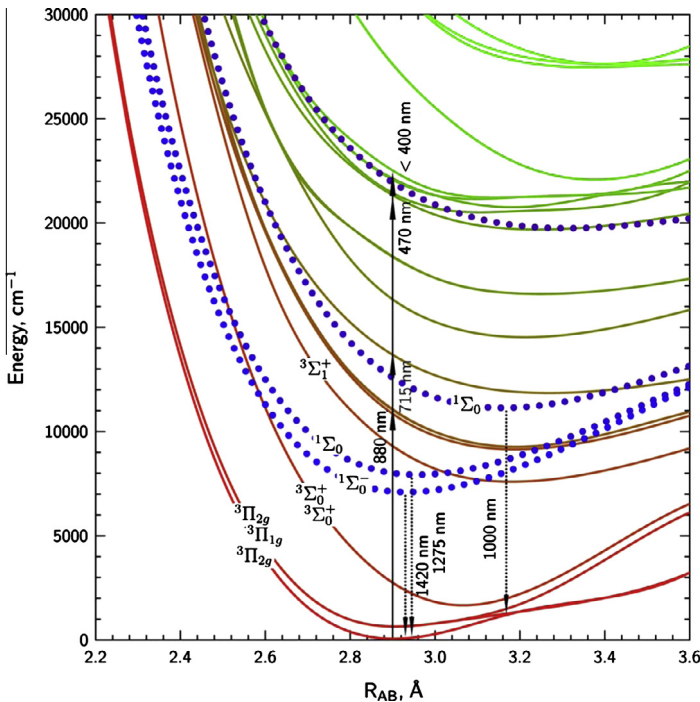


Fig. 6. Total energy curves for low-lying states of $[Bi_2]^{2-}$. Reproduced with permission from Ref. [70]. Copyright © 2009, IOP Publishing.

[73–86]. Fink and coworkers experimentally and theoretically investigated a broad range of Bi related systems such as BiO [73,78], bismuth monohalides [74,76], BiN [75], BiOH [77], and BiNa [79]; all these materials demonstrate NIR emission with multiple sharp peaks, although their emission wavelengths are different. The notable difference between these emitters and Bi^{3+} , Bi^{2+} , Bi^+ , and charged Bi polyhedra lies in the emission lineshape. It has been found that Bi molecules or radicals stabilized by Ar matrices or counterions demonstrate multiple sharp emission peaks, as revealed by laser-induced fluorescence spectroscopy. Interestingly, such emission bands could cover ultrabroad spectral range (e.g., the electronic transitions from BiN molecule is from 700 to 1600 nm, as shown in Fig. 7), while the emissions from Bi^{3+} , Bi^{2+} , Bi^+ , and charged Bi polyhedra show continuous broad emission covering the visible or NIR ranges. This implies that merely employing Bi element with an array of oxidation states may result in abundant emission characteristics in one material system, if one could control the spatial distribution of such centers to effectively suppress the nonradiative energy migration [87]. It is necessary to note that the widely used characterization techniques for Bi molecules or radicals are luminescence and Raman scattering spectroscopy coupled with theoretical calculations. Such analyses make it difficult to obtain an in-depth understanding of the observed photophysical behaviors, since one cannot know the exact structural information of these species and therefore cannot establish exact structure–property relationships. Furthermore, the matrices used for the stabilization of these emitters are a chief barrier for their practical applications, although laser output has been achieved in a certain experimental condition [84]. Based on these considerations, in this review we will not lay our focus on these Bi molecules or radicals. For more background information on these species, the readers are referred to other related papers [73–86].

Experimental results revealed that some glasses and bulk/powdered crystals containing Bi also demonstrated ultrabroad NIR emissions. Since the first report on the observation of NIR emission in bismuth doped aluminosilicate glasses by Fujimoto et al. [88], much effort has been devoted to realize

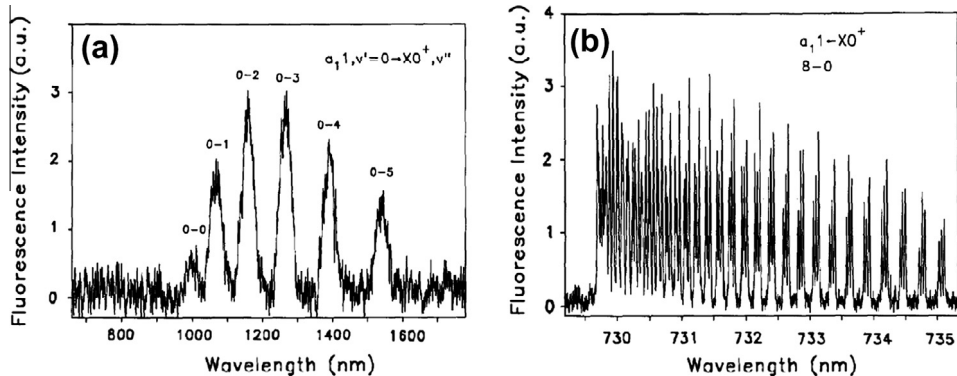


Fig. 7. (a) Fluorescence spectrum of the $u' = 0, v''$ progression of the $a_{1,1} \rightarrow X0^+$ transition of BiN. The spectrum was measured with 5 mm slit widths of the monochromator and a Ge detector equipped with an 830 nm long-pass filter. (b) Medium-resolution scan of the excitation spectrum of the 8-O band. The spectral resolution is $\sim 0.3 \text{ cm}^{-1}$. Reproduced with permission from Ref. [75]. Copyright © 1993, Elsevier Science B.V.

ultrabroad amplification and lasers using such kind of materials [89–94]. Meanwhile, multiple mechanisms have been proposed to explain the ultrabroad emission spectrum, but there is little consensus on the nature of the active sites or the details of the emission mechanism [95]. Although the importance of the hosts has been recognized, their role for the stabilization of Bi centers is still unclear. In this regard, the critical issue involves the unknown local coordination environments of Bi in these materials. This is a great obstacle to the understanding of Bi-related NIR emission behaviors, since most researchers merely reported the PL-related results and did not show definitely convincing and direct evidences related to the local environments of Bi in studied materials [35], owing to the limited characterization techniques available. Great efforts are urgently needed to establish the structure–property relationships in Bi doped glassy materials, which will be helpful to rationally design optical materials with high emission yields and optimal emission wavelengths. In view of the importance of this material system, especially for the applications as laser and amplifier media, we will deal with it in details.

As described above, the photophysical properties of Bi is closely related to their oxidation states, exact local environments in matrices, the doping concentrations, as well as the preparation procedures. This diversity, on one hand, makes it challenging to elucidate the related PL mechanisms of studied systems. On the other hand, it presents abundant parameters available to control the emitter species in a broad range of matrices for the realization of targeted emission characteristics.

The past decades have seen remarkable advancements in the understanding of the emission mechanisms of Bi active centers as well as in the development of new material systems aiming at their practical applications, although a deep insight into the PL mechanism in some systems is still greatly required. The following sections present a critical overview of different types of bismuth activated photonic materials including the basic synthesis and characterization techniques as well as the detailed photophysical properties of these materials.

3. Synthesis and characterization of Bi doped materials

3.1. Synthesis of Bi doped materials

The available data suggests that Bi oxidation states as well as the resulting photophysical properties are closely related to the preparation methods adopted. Bi active centers can form in an array of inorganic and organic matrices, and diverse synthesis approaches have been reported. Additionally, it was found that the preparation atmosphere is one critical parameter for Bi active centers: usually Bi in the samples prepared in air or oxidized atmosphere tends to be +3 and +2 states, although other

species may coexist. In general, Bi activated phosphors were conventionally synthesized via a solid state reaction using powdered raw materials as starting materials. Meanwhile, other methods including liquid phase synthesis, vapor deposition, melt-quenching and low-temperature vacuum-annealing techniques have been developed to obtain luminescent soft, bulk, film and powdered materials, respectively. It is also found that Bi active centers can be tuned by using out-field induced approaches, and such phenomena will be discussed in details in Section 5.2.1.

3.1.1. Solid state reaction

A solid state reaction, also called a dry media reaction or a solventless reaction, is chemical reaction in which only solid raw materials are used. It is the most widely used approach for the preparation of polycrystalline solids from a mixture of solid starting materials. Solids do not react each other at room temperature over normal time scales and it is necessary to heat them to much higher temperatures, often to 1000–1500 °C in order for the reaction to occur at an appreciable rate. The factors determining the feasibility and rate of a solid state reaction include, reaction temperature, time scales and atmospheres, structural properties of the reactants, surface area of the solids, their reactivity and the thermodynamic free energy change associated with the reaction [96,97]. The key advantage of solid state reaction is that it allows the reactants to chemically react without the presence of a solvent. Eliminating the solvent from the reaction means that a solid state reaction produces more product than a normal reaction can. Since there is no solvent, there is no waste to eliminate at the end of the reaction. Thus, solid-state reaction method is recognized as an environmentally friendly technique for the large-scale preparation of a broad range of materials, especially for phosphors. The mechanism of solid-state reactions is diffusion control reaction and hence, repeated grinding and repeated heating are required. Furthermore, the controlled atmosphere is necessary to manipulate the valence of the activator and the stoichiometry of the host lattice [98]. It has been reported that this technique can be employed for the synthesis of Bi³⁺ or Bi²⁺ doped phosphors. For instance, Srivastava synthesized a series of Bi²⁺ doped M²⁺BPO₅-based (M²⁺ = Ba²⁺, Sr²⁺ and Ca²⁺) phosphors using this method [55]. Typically, the mixture of Bi₂O₃, M²⁺CO₃, H₃BO₃ (5 mol% excess) and (NH₄)₂HPO₄ (5 mol% excess) was ball-milled and heated in air at 300 °C (1 h), 700 °C (3 h) and 1000 °C (10 h). Between each heating step the sample was re-homogenized. The final annealing occurred in a reducing atmosphere (99.5%N₂–0.5% H₂) at 1000 °C for a period of 2 h. The synthesized samples with the general composition (M_{0.995}Bi_{0.005}BPO₅), display a white body color [55], owing to the existence of Bi²⁺ ion in the matrices. Other phosphors such as Bi²⁺-doped strontium borates and strontium phosphates can be synthesized using this method [56,57].

Solid state reaction method presents an economic route for the synthesis of low-cost products, which is of vital importance to make them applicable. However, there are several limitations in synthesis of phosphors by such a method. Firstly, this process often results in poor homogeneity and requires high calcinations temperature. Secondly, the grain size of phosphor powders prepared by this method is in several tens of micrometers. Phosphors of small particles must be obtained by grinding the larger phosphor particles [98].

3.1.2. Liquid phase reaction

A liquid phase reaction is chemical reaction in which solvents are used. In comparison with solid state reaction, it does not comprise of the normal mixing, calcinations and grinding operations. This technique can be widely used for the synthesis of subvalent Bi (i.e., the average valence state of Bi is +1 or between +1 and 0) or even negatively-charged Bi species with peculiar optical properties [6–9,33–35,59–61,66,69]. Indeed, the reports of the liquid-phase synthesis and photophysical properties of subvalent Bi date back to half a century ago [6–9,59,60], but it was not until recently that luminescent properties of these species were studied [33–35,61,66,69]. In the 1960s, Smith and coworkers systematically investigated the evolution of Bi oxidation states in molten salt systems [6–9,59,60]. Typically, such experiments consist of mixing reactants such as NaCl, NaBr, AlCl₃, AlBr₃, BiCl₃ and metallic Bi, heating mixed reactants over the eutectic point, and taking the absorption spectra of the obtained liquids. Usually, BiCl₃ was present in large excess. Based on the thorough examination of spectroscopic properties of Bi containing liquids, Smith et al. first proposed that the absorption bands in UV-vis-NIR spectral ranges result from the electronic transitions of subvalent Bi

(e.g., Bi^+ , Bi_5^{3+} , or Bi_8^{2+}) [6–9,59,60]. Such pioneering work leads to more concentrated research work on the synthesis and characterization of material systems containing subvalent Bi in the following decades, and much clearer pictures on the valence states of Bi as well as smart structural units have been reported by Ruck, Kloo and their coworkers [11–24,31,32]. Now it has been recognized that highly Lewis-acidic environments have been considered a necessary prerequisite for the stabilization of Bi cationic clusters since the interactions between the clusters and even moderately strong Lewis bases result in the stabilization of higher, more acidic oxidation states of the element and a concomitant disproportionation of the cluster cation [20]. This stabilizing effect on the clusters in acidic media has been called acid stabilization or anti-coordination chemistry. Very recently, Ruck et al. studied the viability of Lewis-acid ionic liquids for the synthesis of low-valent bismuth compounds. At room temperature, elemental bismuth and bismuth (III) cations synproportionate in the ionic liquid $[\text{BMIM}]^+\text{Cl}/\text{AlCl}_3$ ($[\text{BMIM}]^+$:1-n-butyl-3-methylimidazolium) within minutes. The existence of bismuth polycations in the dark colored solution was proven by Raman spectroscopy. Dark-red crystals of $\text{Bi}_5(\text{AlCl}_4)_3$ were isolated from the ionic liquid [18]. The method allows the synthesis of bismuth cluster compounds under milder conditions than in high-temperature melts and more conveniently and environmentally friendly than in liquid SO_2 with strongly oxidizing, toxic agents like SbF_5 or AsF_5 . In subsequent studies, Sun et al. found that Bi_5^{3+} and Bi^+ emitters stabilized by the Lewis acidic liquid show ultrabroad NIR PL with a lifetime of around 1 μs [61], and high-quality $\text{Bi}_5(\text{AlCl}_4)_3$ crystal prepared by this method exhibits a broadband emission band from 1 to 2.7 μm [33,35].

Liquid phase reaction method provides a facile route to adjusting the oxidation states of Bi, which is important to obtain a deeper understanding of the physiochemical properties of this wonder metal. However, owing to rather air and moisture sensitivity, the materials prepared by this approach cannot be used for practical applications. Thus, it is highly desirable that new methods for the stabilization of such emitters could be developed to obtain air-stable products, which will pave the way for their broad applications in photonics.

3.1.3. Vapor deposition method

Vapor deposition refers to any process where materials in a vapor state are condensed through condensation, chemical reaction, or conversion to form a solid material. Vapor deposition processes usually occur within a vacuum chamber. There are two categories of vapor deposition processes: physical vapor deposition (PVD) and chemical vapor deposition (CVD) methods. Until now, there are several methods reported to prepare Bi active centers in various matrices by using PVD technique. In an early effort, Fink et al. employed PVD method to synthesize various Bi related systems such as BiO [73,78], bismuth monohalides [74,76], BiN [75], BiOH [77], and BiNa [79], all of which show peculiar electronic transitions. In an attempt to prepare NIR-emitting films containing Bi, Sun and coworkers fabricated bismuth glass/Si nanocrystal superlattices [99] and Bi doped Si-rich silica films [100] by using multitarget sputtering method. Note that the films prepared by sputtering method must undergo high-temperature annealing in an inert atmosphere (e.g., N_2 or Ar) to activate Bi centers and eliminate the structure defects [99,100]. Since 2005, CVD technique is widely used to fabricate fiber preforms [71]. Typically, preforms for single-mode fibers were prepared by CVD method by using a silica glass-support tube. The core of preforms was formed by the CVD deposition of targeted elements such as phosphorus, germanium, aluminum or silicon dioxide. Doping with Bi was realized by impregnating a porous layer of the core glass with the solution of bismuth salts. The as-prepared preforms containing Bi were used for fiber drawing at high temperatures. Similar to films prepared by sputtering method, undergoing high-temperature process is prerequisite to activate Bi active centers.

Owing to the potential applications of NIR emitting fibers and thin films in photonic domains, developing more revolutionary fabrication methods will, in a sense, extend their practical applications. For instance, room-temperature method for the preparation of films with high emission yields and good optical quality is greatly expected, which is not only important for energy saving, but also presents new routes to tuning Bi active centers and making it much easier to be integrated with other platforms such as Si.

3.1.4. Melt-quenching method

The melt-quenching method consists of two steps, i.e., melting the mixtures and subsequent quenching of melt to obtain solid materials. In general, one can use powders of the raw materials as the starting materials, which become glassy melts at high temperatures. The melts were then poured onto a cold brass plate and annealed at suitable temperatures (for glasses, at about glass transition temperature) for several hours to relieve internal stresses. Luminescent Bi-doped glasses, which were usually synthesized by melt-quenching method, have been extensively investigated due to their potential applications in solid state lasers, fiber lasers and amplifiers. A broad range of glasses containing Bi^{3+} and NIR-active Bi have been successfully prepared by using this technique [41,88]. The formation of Bi active centers in glasses is closely related to glass compositions. In particular, NIR emitting glasses containing Bi have been extensively studied over the past decade [95]. The preparation as well as optical properties of these glasses will be discussed in details in Section 5.2.

3.1.5. Vacuum-annealing method

Vacuum-annealing method refers to a process where materials are annealed in a vacuum condition. This technique usually acts as a post-treatment method [101]. In a recent study, it was employed for the synthesis of optically active bismuth embedded zeolite Y [37]. Typically, zeolites were stirred in an aqueous solution of Bi^{3+} prepared from $\text{Bi}(\text{NO}_3)_3 \cdot 5\text{H}_2\text{O}$ at room temperature to exchange the Na^+ ions with Bi^{3+} ions. The products were removed by centrifugation, then thoroughly washed with deionized water, and dried in air. The obtained powders were first put into a flask with an adapter, and then inserted into the chamber of a vacuum furnace. The sample was thermally treated at 400°C and 6×10^{-5} Pa for 24 h [37]. By using such thermal treatment, NIR-active Bi centers form in the pores of zeolite framework. As is known, zeolites are crystalline microporous aluminosilicates based on AlO_4 and SiO_4 tetrahedra that are connected by shared oxygen atom bridges. Combinations of these tetrahedral structures lead to over 176 unique zeolite framework types with diverse channels. Thus, it is believed that using this technique more interesting phenomena as well as new Bi NIR emitters are hopeful to be found by suitable choice of zeolite frameworks, which is helpful to deepen the understanding of Bi-related photophysical properties.

3.2. Characterization techniques for Bi

3.2.1. X-ray techniques

X-ray photons are a form of electromagnetic radiation produced following the ejection of an inner orbital electron and subsequent transition of atomic orbital electrons from states of high to low energy. When a monochromatic beam of X-ray photons falls onto a given specimen three basic phenomena may result, namely absorption, scatter or fluorescence. The coherently scattered photons may undergo subsequent interference leading to the generation of diffraction maxima [102]. There are several powerful techniques including X-ray crystallography, X-ray photoelectron spectroscopy (XPS), extended X-ray absorption fine structure (EXAFS), and X-ray absorption near edge structure (XANES).

3.2.1.1. X-ray crystallography. X-ray crystallography is a powerful approach to determining the arrangement of atoms within a crystal, in which an X-ray beam strikes a crystal and causes the beam of light to spread into many specific directions. From the angles and intensities of these diffracted beams, a crystallographer can produce a three-dimensional picture of the density of electrons within the crystal. Since lots of materials containing Bi can form diverse single crystals, this technique is widely adopted to solve the crystal structures [11–24,31–36]. Some crystals with well-defined structures have been systematically investigated and abundant evidences indicate that they are optically active [33–35,66,69].

The most precise method of X-ray crystallography is single-crystal X-ray diffraction (XRD), in which a beam of X-rays strikes a single crystal, producing scattered beams. The single crystal should be sufficiently large (typically larger than 0.1 mm in all dimensions), pure in composition and regular in structure, with no significant internal imperfections such as cracks or twinning. However, sometimes it is difficult to obtain a high-quality crystal of the material under study. In this case, powder XRD becomes an alternative of single-crystal XRD. Crystal structure determination from powder

XRD is possible, but extremely challenging due to the overlap of reflections. The crystal structures of known materials can be refined using the Rietveld method that is a so-called full pattern analysis technique [103]. A crystal structure, together with other parameters related to instrumental and microstructural information is used to generate a theoretical/calculated diffraction pattern which can be compared to the experimental data. A least squares procedure is then used to minimize the difference between the calculated pattern and each point of the observed pattern by adjusting model parameters [104]. A number of programs that can be used in structure determination are GSAS [105], TOPAS [106], DASH [107], and a few others. Very recently, Rietveld method was used for the analysis of the structural characteristics of dehydrated zeolites containing Bi, and for the first time direct experimental evidence on the formation of monovalent Bi (i.e., Bi^+) in zeolite Y is provided [37]. Bi occupies single-type site in the sodalite cages, which is coordinated to three oxygen atoms of the base of the prism. PL results as well as quantum chemistry calculations suggest that the substructures of Bi^+ in the sodalite cages contribute to the ultra broad NIR emission.

3.2.1.2. XPS. XPS is a quantitative spectroscopic technique that measures the elemental composition, chemical state and electronic state of the elements which exist within a material. XPS is a surface chemical analysis technique, which could give the element information at a sample surface with a thickness in the range of 1–10 nm. This technique can be employed for the analysis of Bi element in different hosts. It is necessary to note that the inner-orbital binding energy (BE) of bismuth strongly depends on its coordination environments, as revealed by Morgan et al. [108]. For instance, it was reported that the $4f_{7/2}$ BE of Bi in BiF_3 shifts to higher energy by 1.5 eV relative to that in BiI_3 as a result of the increased substituent electronegativity [108]. As shown in Fig. 8, the BE of $\text{Bi}^{3+}(4f_{7/2}, 4f_{5/2})$ in Bi_2O_3 , determined by lineshape deconvolution, is peaked at 158.9 and 164.1 eV, respectively, whereas those in $\text{Bi}(\text{NO}_3)_3 \cdot 5\text{H}_2\text{O}$ shift to 160.0 and 165.4 eV, respectively. In contrast, the XPS peaks of $\text{Bi}^0(4f_{7/2}, 4f_{5/2})$ in bismuth metal are at 157.0 and 162.3 eV, respectively. This result clearly suggests that a higher oxidation state of Bi results in a larger BE and that the BE is greatly influenced by the exact coordination environment of Bi, even for Bi with the same oxidation state.

In view of these facts, the assignment of oxidation states of Bi should be careful enough when one just takes a XPS spectrum for a sample containing Bi. In general, measuring the BE of Bi in a series of samples [109,110] is helpful to make a reliable assignment or to obtain more meaningful conclusions.

3.2.1.3. EXAFS and XANES. X-ray absorption spectroscopy (XAS) includes both extended X-ray absorption fine structure (EXAFS) and X-ray absorption near edge structure (XANES), which is an element-specific method to investigate the bond angles, bond lengths and coordination numbers. XAS is the measurement of the X-ray absorption coefficient of a material as a function of energy [111].

EXAFS and XANES are powerful tools for the analysis of Bi in various hosts [112–117]. Because Bi possesses many kinds of oxidation states and may have quite complicated bonding possibilities, it is necessary to be careful enough for the structural analysis of Bi containing materials. Otherwise, it is hard or impossible to establish a convincing structure–property relationship. Lyczko et al. systematically investigated a subvalent oxidation state of bismuth in N,N-dimethylthioformamide solution using EXAFS and XANES coupled with other techniques including UV-vis, IR, and cyclic voltammetry (Fig. 9) [115], which is one of several typical works in this area [113–115]. An interesting phenomenon is that at the dissolution of anhydrous bismuth(III) trifluoromethanesulfonate in N,N-dimethylthioformamide (DMTF) a deep red-orange complex with an absorption maxima at 457 nm, is formed. Bismuth (III) is reduced by the solvent to a low-valence oxidation state stabilized by the sulfur-coordinating solvent DMTF. The obtained complex is weakly solvated, as seen by a slightly higher absorption energy of the L_{III} edge than that of the DMTF-solvated bismuth(III) ion (Fig. 9b). The XAS data reveal a dimeric bismuth complex solvated by a single DMTF molecule, where sulfur atom bridges the bismuth atoms.

Given the complexity of the physicochemical properties of Bi, when employing XAS technique, we should pay more attention to the materials themselves as well as the following reasonable analysis; otherwise, one cannot obtain a sound and convincing conclusion, especially in the case of establishing exact structure–property relationship.

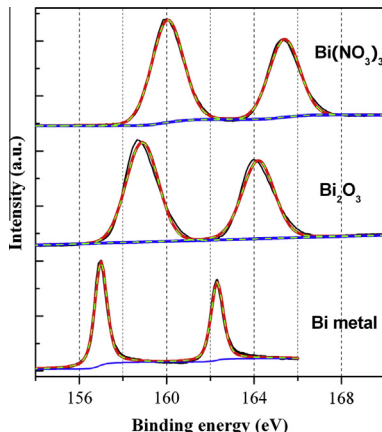


Fig. 8. XPS spectra of Bi metal (Alfa Aesar, 99.999%), Bi_2O_3 (Sigma–Aldrich, 99.8%) and $\text{Bi}(\text{NO}_3)_3 \cdot 5\text{H}_2\text{O}$ (Wako, 99.9%). Shirley or linear type background was subtracted, and then the curves were fitted using a mixed Gauss–Lorentzian function. Note that the background for Bi metal was fitted separately by Shirley function in the range of 154–160 and 160–166 eV. The black, red, green, and blue lines represent experimental data, fitted curves, fitted peaks and backgrounds, respectively. All XPS spectra were taken at room temperature by PHI Quantera SXM (ULVAC–PHI) system equipped with a monochromatic Al K α source. Note that Bi metal is covered with thin oxide layer in condition as received, and sputtered with rotation to remove it before the measurement. The oxide and nitrate samples were measured without these pretreatments. For these spectra, C1s (285 eV) line was used as the internal standard for binding energies of Bi.

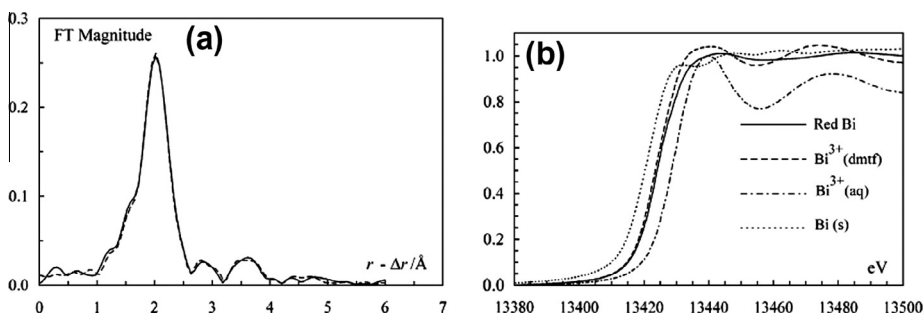


Fig. 9. (a) Fourier transform and the fit of the deep red bismuth DMTF complex. (b) Edge structure of bismuth metal: DMTF solution of the deep red bismuth complex (labeled red Bi); hexakis(*N,N*-dimethylthioformamide)-bismuth(III) ion in solution (labeled $\text{Bi}^{3+}(\text{dmtf})$); hexaaquabismuth(III) ion in aqueous solution (labeled $\text{Bi}^{3+}(\text{aq})$); metallic bismuth (labeled Bi(s)). Reproduced with permission from Ref. [115]. Copyright © 2004, American Chemical Society.

3.2.2. NMR and ESR spectroscopy

Nuclear magnetic resonance (NMR) is a physical phenomenon where magnetic nuclei in a magnetic field absorb and re-emit electromagnetic radiation. NMR allows the observation of specific quantum mechanical magnetic properties of the atomic nucleus. Over the past decades, NMR spectroscopy has been widely used for the studies of crystals and amorphous materials. While X-ray crystallography has been proven to be useful for structural determinations in highly crystalline systems containing Bi [11], NMR has long been considered to be an unsuitable technique for Bi analysis, because of its large nuclear quadrupole moment. In 2009, Hamaea et al. presented the first detailed study of ^{209}Bi solid-state NMR (SSNMR) spectroscopy of extremely broad central transition powder patterns [118]. ^{209}Bi SSNMR spectra of several Bi containing materials (bismuth oxyhalides, bismuth nitrate pentahydrate, nona-aquabismuth triflate, and bismuth acetate) were acquired using frequency-stepped techniques. The ^{209}Bi SSNMR experiments at 9.4 T yield powder patterns with breadths ranging from 0.9 to

14.6 MHz, from which quadrupolar coupling constants between 78 and 256 MHz, were extracted via analytical simulations. The breadths of the quadrupolar-dominated spectra and overall experimental time are greatly reduced for experiments conducted at 21.1 T, which yield high signal-to-noise spectra in which the smaller effects of bismuth chemical shift anisotropy can be clearly observed. The pioneering work demonstrated by Hamaed et al. suggests that ^{209}Bi SSNMR could be used for the characterization of a variety of Bi-containing materials and compounds, especially when Bi concentration is high.

Electron spin resonance (ESR) or electron paramagnetic resonance (EPR) is defined as the form of spectroscopy concerned with microwave-induced transitions between magnetic energy levels of electrons having a net spin and orbital angular momentum. It is a versatile, nondestructive analytical technique which can be used for a variety of applications including: oxidation and reduction processes, bi-radicals and triplet state molecules, reaction kinetics, as well as numerous additional applications in biology, medicine and physics. However, this technique can only be applied to samples with one or more unpaired electrons. A great number of materials contain such paramagnetic entities, which may occur either as electrons in unfilled conduction bands, electrons trapped in radiation damaged sites, or as free radicals, various transition, bi-radical, triplet states, impurities in semiconductors, as well as other types.

For Bi doped materials, ESR is used to examine the possible luminescent center. In 2007, Khonthon et al. observed ESR signal at $g \approx 2.0$ in Bi-doped glasses and glass-ceramics [119]. Consequently, it is suggested that the broad NIR luminescence of Bi-doped glass and glass-ceramics are most likely to be caused by elemental clustering, such dimer with the DALTON quantum chemistry code. The principal values of the g factor tensor were found to be $g_{11} \approx 2.002360$, $g_{22} \approx 2.002377$, $g_{33} \approx 2.193984$ [70], which confirm the rationality of the assumption. However, incompatible results that no ESR signal due to the unpaired electrons in their bismuth-doped silica glass also exist, and corresponding valence states of bismuth ions without unpaired electrons was ascribed to be $\text{Bi}^{3+}(\sim 5\text{d}^{10}6\text{s}^2)$ or $\text{Bi}^{5+}(\sim 5\text{d}^{10})$ [88]. In this regard, the following issues must be well understood. First, there is no reason for the assignment of NIR emission in diverse glass hosts to one kind of Bi emitter [35]. Second, more careful consideration and convincing experimental results are needed to correlate the ESR-active centers with NIR active centers in the studied systems. It is obvious that, only exploiting ESR technique cannot obtain a clear and convincing picture of the PL mechanism related to Bi, since the basic and important issue, i.e., the detailed structural feature of Bi active centers, is not resolved.

3.2.3. Photoluminescence spectroscopy

Photoluminescence (abbreviated as PL) is a process in which a substance absorbs photons (electromagnetic radiation) and then re-radiates photons. Quantum mechanically, this can be described as an excitation to a higher energy state and then a return to a lower energy state accompanied by the emission of photons. PL spectroscopy is a contactless, nondestructive method to probe the electronic structure of optically active centers in many kinds of materials. This technique is widely employed to analyze the PL behaviors of Bi containing systems. One of the advantages of this method lies in the easiness of the identification of Bi active centers, especially for Bi^+ [6–9], Bi^{2+} [55,56], Bi^{3+} [41], Bi_5^{3+} [33,35], Bi_8^{2+} [34], and Bi_2^{2-} [69], in some systems.

3.2.4. Quantum chemistry calculations

In addition to experimental techniques available for Bi, quantum chemistry calculations have been extensively employed to predict the structural and electronic properties of molecules and materials containing Bi. In the 1960s, Smith and the coworkers experimentally studied the behaviors of electronic transitions of a series of subvalent Bi including Bi^+ [8,9,59,60], Bi_5^{3+} [9] and Bi_8^{2+} [7]. To explain the observed phenomena, the theory of ligand field splittings of $p^{2,4}$ configurations and of the relative intensities of $p^2 \leftrightarrow p^2$ electric dipole transitions has been developed. The previously published spectrum of Bi^+ in molten salt media is rationalized very well by this theoretical model with regard to both the positions of the experimental bands and their relative intensities. Corbett et al. explained the absorption properties of Bi_5^{3+} polycation by using the linear combination of atomic orbitals (LCAO)-molecular orbital calculation [10]. The comparison of experimental and theoretical results suggests

this method is fortuitously good to deal with the electronic excitation process of bismuth polycations [10,33–35].

Quantum chemistry calculations have received great attention during the past fifty years, especially in recent twenty years. Until now, a broad range of state-of-the-art quantum chemistry codes have been developed to realize more accurate and convincing prediction of physicochemical properties of material systems. This presents new chances for theoretical calculation of the photophysical properties of Bi species in diverse hosts. Day et al. theoretically investigated the electronic transitions of Bi_5^{3+} , Bi_8^{2+} , and Bi_9^{5+} polycations by means of an ab initio single-excitation configuration-interaction approach [120]. The calculation shows that singlet-triplet transitions, which are made accessible by strong spin-orbit coupling, are responsible for some of the observed absorptions. Ab initio calculations of this kind of Bi species using other quantum chemistry codes were also carried out [19].

In recent several years, density-functional theory is used to calculate the properties of the neutral and cationic Bi_n clusters [34,35,121]. Sun et al. employed the Amsterdam Density Functional (ADF) program package in order to calculate the characteristics of electronic transitions of Bi_5^{3+} and Bi_8^{2+} [34,35]. Detailed quantum chemistry calculations make it possible to assign the observed excitations to some electronic transitions of Bi_5^{3+} and Bi_8^{2+} polycations, especially at shorter wavelengths [34,35].

Besides the theoretical work on positively charged Bi species, there are several reports on the calculation of electronic structures of negatively-charged Bi species. Dai et al. first calculated the excitation energies of $[\text{Bi}_2]^{2-}$ with $d(\text{Bi}-\text{Bi}) = 2.8377 \text{ \AA}$ in $(\text{K-crypt})_2\text{Bi}_2$ using the Beijing density function program, and revealed that the anion has at least four excitation bands located at around 1380, 1062, 562, and 399 nm [28]. In a recent work, Sokolov et al. calculated the excitation energies using the Gamess (US) quantum-chemical code [70]. The authors showed that several transitions from the $^3\Pi_{2g}$ ground state to the $^3\Sigma$ excited states are allowed and correspond to absorption bands near 880, 715, 470, and below 400 nm. Moreover, it was shown that NIR luminescence bands in the wavelength regions of 1420–1520, 1275–1375, and 1000–1060 nm should also occur due to spin-forbidden transitions from the three $^1\Sigma$ singlet excited states to the $^3\Pi$ ground state and/or to one of the first two excited $^3\Pi$ states. However, at present the theoretical results are only approximate and do not completely agree with the experimental facts [69].

Although quantum chemistry calculation of Bi species has been done for nearly a half century, it is obvious that the theoretical works in this field are rather insufficient to explain the observed experimental results. In the following years, great efforts on theoretical calculation of Bi species are needed to deepen the understanding of the observed experimental results in Bi containing materials. Considering the rapid development in the field of quantum chemistry calculations, it is believed that more interesting results will be demonstrated in this regard.

4. Bi doped visible emitting materials

4.1. Bi^{3+} doped crystals and glasses

Bi^{3+} ion belongs to the group of so-called heavy ns² ions (Tl^+ , Pb^{2+} and Bi^{3+}), the photoluminescence of which have been studied in a considerable number of hosts. In the 1960s, Blasse et al. reported the fluorescence of a number of Bi^{3+} -activated phosphors synthesized by high-temperature calcinations, in which only host lattices containing a sublattice of large, trivalent cations are used [122]. Typical features of Bi^{3+} -related electronic transitions are as follows. Firstly, the absorption and emission bands of Bi^{3+} active center located at UV and blue/green regions, respectively. Two absorption bands were found in the case of $\text{Y}_2\text{O}_3-\text{Bi}$, $\text{YOF}-\text{Bi}$, $\text{YOCl}-\text{Bi}$, and $\text{LaOCl}-\text{Bi}$, as shown in Fig. 10. It seems obvious to ascribe these two bands to the transitions $^1S_0 \rightarrow ^3P_1$ and $^1S_0 \rightarrow ^1P_1$. Secondly, the variation of Bi^{3+} absorption bands with the nature of the surrounding ligands is a well-known phenomenon. If the electronegativity of the ligand decreases, the absorption bands shift to lower wavenumbers due to covalence effects [123].

Although luminescence has been reported from Bi^{3+} doped compounds, PL quenching was frequently observed at fractional bismuth concentrations of greater than a few percent [124,125]. Subsequently, blocking of the energy migration between Bi^{3+} system and quenching centers was

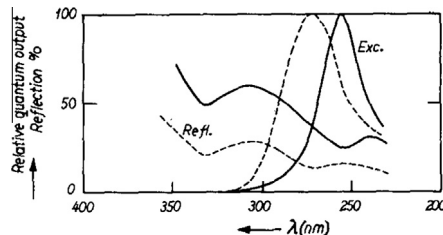


Fig. 10. Diffuse reflection spectra and relative excitation spectra of the fluorescence of YOCl–Bi (solid line) and LaOCl–Bi (broken line). Reproduced from Ref. [122]. Copyright © 1968, American Institute of Physics.

found in $\text{Bi}_4\text{Ge}_3\text{O}_{12}$, where the Stokes shift of Bi^{3+} absorption and emission is large. In addition, non-radiative decay by multiphonon processes is limited by the large $^3\text{P}-^1\text{S}$ energy difference. Crystals of $\text{Bi}_4\text{Ge}_3\text{O}_{12}$ were grown from stoichiometric melts using the Czochralski method by Weber et al. [126]. Intense broadband emission in the visible region was observed under optical and X-ray excitation. The temperature dependence of fluorescence intensity and lifetime for $\text{Bi}_4\text{Ge}_3\text{O}_{12}$ established that significant nonradiative decay appears only at temperatures above ~ 250 K. Nonradiative processes dominate radiative decay at temperatures ≥ 400 K.

Above mentioned bismuth germanate crystal has been used as host materials for Nd^{3+} lasers [127]. Subsequently, energy transfer from Bi^{3+} to Nd^{3+} was reported in germanate glass [45]. The optical characteristics of Bi^{3+} were similar to those of $\text{Bi}_4\text{Ge}_3\text{O}_{12}$. Energy transfer between Bi^{3+} and Nd^{3+} presented in germanate glass may be utilized for the increase of the pumping range of Nd^{3+} glass laser. Although the fluorescence efficiency of Bi^{3+} doped germanate glasses was only 2% at room temperature, the high oscillator strength of Bi^{3+} and the good spectral overlap between the levels $^4\text{G}_{7/2}$, $^2\text{G}_{9/2}$, $^4\text{G}_{9/2}$, $^2\text{D}_{3/2}$, $^4\text{G}_{11/2}$, $^2\text{P}_{1/2}$, $^2\text{D}_{5/2}$, $^4\text{D}_{3/2}$, $^4\text{D}_{5/2}$, and $^4\text{D}_{1/2}$ of Nd^{3+} enable the increase of pumping efficiency several fold. Because of the possibility of sensitization of rare earth fluorescence by Bi^{3+} in various crystals, it is of importance to develop new host materials for lasers in which Bi^{3+} is present at low concentration, in order to prevent concentration quenching. As a result, Bi^{3+} doped germanate, silicate, borate, and phosphate glasses have been reported [128–131].

4.2. Bi^{2+} doped crystals

In 1886, Lecoq de Boisbaudran reported a red luminescence for bismuth in the alkaline-earth-metal sulfates, which was listed as evil from “classical phosphors-Pandora’s box” by Blasse [40]. Half a century later, the red luminescence was confirmed by Kroeger et al. [132] and they suggested that this luminescence may be due to trivalent or pentavalent bismuth. A satisfying explanation came another half century later [53], which suggested that this luminescence was due to Bi^{2+} , a hardly known valence state of bismuth with $6s^26p$ configuration. Similar orange emission from bismuth-doped SrB_4O_7 was also observed by the same group during the same period [39]. Recent studies revealed that Bi^{2+} ion widely exists in crystalline hosts such as strontium tetraborate, borophosphate, and strontium phosphate.

4.2.1. Strontium tetraborate

Strontium tetraborate (SrB_4O_7) is a very suitable host lattice to obtain efficient luminescence from ions which are built on strontium sites, and also considered to be the most suitable hosts for stabilizing, under oxidizing conditions, divalent rare-earth ions (e.g., Eu^{2+} , Sm^{2+} , and Yb^{2+}) [133–136]. This unique property originates from the relatively stiff crystal structures built up by BO_4 units that shield divalent dopant ions from atmospheric oxygen [56].

Bi^{2+} -doped luminescent materials is rather limited, partly owing to difficulties in stabilizing the divalent bismuth ion over its trivalent form. Bismuth in SrB_4O_7 enters the host lattice partly as Bi^{2+} by firing intimate mixtures in N_2 , which shows an efficient orange luminescence with nicely structured spectra at 4.2 K under 480 nm excitation, was firstly reported by Blasse et al. [39].

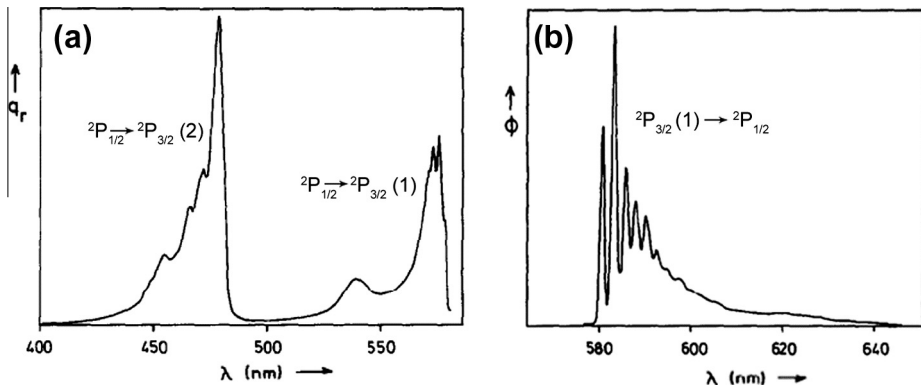


Fig. 11. (a) Excitation spectrum of the orange luminescence of $\text{SrB}_4\text{O}_7:\text{Bi}$ at 4.2 K in the visible spectral region. Emission monitored 598 nm. q_r gives the relative quantum output. (b) Emission spectrum of the orange luminescence of $\text{SrB}_4\text{O}_7:\text{Bi}$ at 4.2 K under 480 nm excitation. ϕ gives the radiant power per constant wavelength interval in arbitrary units. Reproduced from Ref. [39]. Copyright © 1994, Elsevier Ltd.

Corresponding transitions of Bi^{2+} are shown in the following excitation and emission spectra of Fig. 11. The presence of vibrational structure in the Bi^{2+} spectra is interesting. The emission spectrum shows a progression in a mode with a frequency of 72 cm^{-1} . The feature in the emission spectrum at about 625 nm is situated at about 1200 cm^{-1} from the zero-phonon line and can be assigned to the borate stretching modes. The borate deformation modes are expected at about 600 nm and are overlapped by the progression.

Recently, Peng et al. compared the emission between Bi^{2+} -doped SrB_4O_7 synthesized via solid-state reaction in air and $\text{SrB}_6\text{O}_{10}:0.5\%\text{Bi}$ prepared in reducing atmosphere, the orange and red emitting of which were suggested to apply in white LEDs [56,137]. Detailed analyses of (i) optical properties of Bi^{2+} in SrB_4O_7 , (ii) lineshape, nonradiative transitions, and thermal quenching, and (iii) impact of alkaline earth substitution in $\text{SrB}_4\text{O}_7:\text{Bi}^{2+}$ were reported [137].

4.2.2. Borophosphate

In the late 1990s, MBPO_5 ($\text{M} = \text{Ca}^{2+}, \text{Sr}^{2+}$ and Ba^{2+}) synthesized at a reducing atmosphere was proposed by Srivastava as an alternative host for Bi^{2+} to realize red luminescence [55]. Besides the known excitation bands of $^2\text{P}_{1/2} \rightarrow ^2\text{P}_{3/2}$ (2) (blue) and $^2\text{P}_{1/2} \rightarrow ^2\text{P}_{3/2}$ (1) (orange), the allowed $^2\text{P}_{1/2} \rightarrow ^2\text{S}_{1/2}$ optical transition in the excitation spectrum has been observed clearly (without interference from the Bi^{3+} species) for the first time in the $\text{BaBPO}_5:\text{Bi}^{2+}$, whereas $^2\text{P}_{1/2} \rightarrow ^2\text{S}_{1/2}$ could not be seen in $\text{CaBPO}_5:\text{Bi}^{2+}$ and $\text{SrBPO}_5:\text{Bi}^{2+}$.

Recently, the transition of $^2\text{P}_{1/2} \rightarrow ^2\text{S}_{1/2}$ was directly observed in all MBPO_5 ($\text{M} = \text{Ca}^{2+}, \text{Sr}^{2+}$ and Ba^{2+}) compounds by Peng et al. [138], as shown in Fig. 12a, which were even synthesized in air condition. Crystal refinement revealed that in BaBPO_5 , only one Ba^{2+} site was present. As shown in the inset of Fig. 12b, it is surrounded by three types of oxygen, i.e., four O_1 , four O_2 and two O_3 . The average bond length is 2.8687 \AA . Assuming that Bi^{2+} is indeed incorporated into the MBPO_5 lattice only on Ba^{2+} -sites, there should be only a single type of Bi^{2+} emission center present in doped material. This is confirmed by a first order exponential decay curve (Fig. 12b). Excitation at wavelengths 619, 562, 432 and 372 nm always leads to the emission at 641 nm. Emission lifetimes at all these different excitation wavelengths fall within an error range of $\pm 1 \mu\text{s}$ around an absolute value of $22 \mu\text{s}$. Similar behavior is observed for $\text{CaBPO}_5:\text{Bi}^{2+}$ and $\text{SrBPO}_5:\text{Bi}^{2+}$.

4.2.3. Strontium phosphate

Different host materials provide different ligand field strength for Bi^{2+} , where great effect can be found on the excitation and emission spectra. $\alpha\text{-Sr}_2\text{P}_2\text{O}_7$ phase has an orthorhombic unit cell with space group Pnma [139], which also have been used as a host material for Bi^{2+} . In this structure,

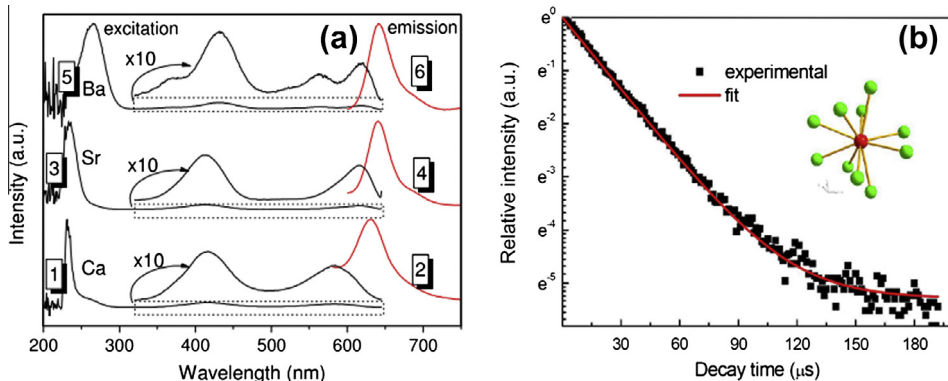


Fig. 12. (a) Excitation and emission spectra of $M_{0.995}BPO_5:0.005Bi$ ($M = Ca^{2+}$ (1, $\lambda_{em} = 660$ nm; 2, $\lambda_{ex} = 416$ nm), Sr^{2+} (3, $\lambda_{em} = 660$ nm; 4, $\lambda_{ex} = 413$ nm) and Ba^{2+} (5, $\lambda_{em} = 660$ nm; 6, $\lambda_{ex} = 430$ nm)) at room temperature. The spectral region of 320–650 nm was amplified 10 times for clarity. (b) Fluorescence decay curve of $Ba_{0.995}BPO_5:0.005Bi$ prepared in air. Excitation and emission wavelengths are 267 nm and 641 nm, respectively. The red curve is a fit of the experimental data to a first order exponential decay equation (lifetime of 22 μ s, correlation coefficient 99.84%). Inset: coordination environment of the Ba^{2+} site (green: oxygen ions; red: Ba^{2+}). Reproduced from Ref. [138]. Copyright © 2009, Optical Society of America.

two types of PO_4 tetrahedrons are linked to each other by corner sharing and P_2O_7 groups are isolated by Sr^{2+} . The average bond lengths of P_1-O and P_2-O are 1.541 and 1.542 Å, respectively; two types of Sr^{2+} sites are both coordinated by nine oxygens with average bond lengths of 2.721 Å for Sr_1-O and 2.679 Å for Sr_2-O , respectively [140].

Early in 1949, Kroeger et al. reported the strong red cathodoluminescence at around 700 nm from Bi-doped $Sr_2P_2O_7$ [132]. Unfortunately, the fluorescence center was ascribed to trivalent bismuth. In 1994, Hamstra et al. confirmed that this emission was due to divalent Bi [53]. Recently, $Sr_{2-x}P_2O_7:xBi^{2+}$ was prepared in CO atmosphere by Peng et al. [57], where x is the concentration of Bi. Upon blue excitation, except for $x = 0$, all samples were found to emit red light, following relaxation of $^2P_{3/2}$ (1) to $^2P_{1/2}$ in Bi^{2+} . Fig. 13a shows the emission spectra of $Sr_{2(1-x)}P_2O_7:0.002Bi^{2+}$ under the excitation of 450 nm. For $x = 0.1$ mol%, the emission peak is located at ~700 nm. At this dopant concentration, it exhibits a pronounced shoulder at ~667 nm. With increasing dopant concentration, intensity of the main peak first increases until it reaches a maximum at $x = 1.0$ mol%. At higher concentration, emission intensity starts to significantly decrease and the shoulder peak gradually disappears. Within the considered concentration range, peak positions remain unaffected from variations in dopant concentration.

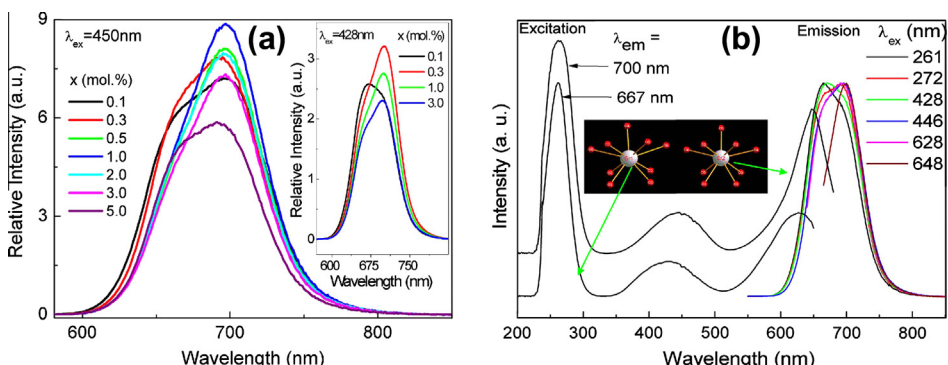


Fig. 13. (a) Emission spectra and (b) excitation and emission spectra of $Sr_{2(1-x)}P_2O_7:0.002Bi^{2+}$. Coordination environments of two types of strontium sites in $Sr_2P_2O_7$ are shown in the inset. Reproduced from Ref. [57]. Copyright © 2010, Optical Society of America.

Unlike previous observations in Bi^{2+} -doped materials, for this phosphate matrix, analyses reveal a strong dependence on excitation wavelength (Fig. 13b). These data suggests that in $\text{Sr}_2\text{P}_2\text{O}_7$ matrix, Bi^{2+} ion is incorporated into two distinct lattice sites. It is assumed that these sites are two Sr sites, Sr (1) and Sr (2), shown in the inset of Fig. 13b.

5. Bi doped near-infrared (NIR) emitting materials

5.1. Subvalent Bi in liquids

The photophysical properties of subvalent Bi in liquid hosts have been investigated thoroughly over the past decades. In the 1960s, Smith et al. studied the behaviors of electronic transitions of subvalent Bi including Bi^+ , Bi_5^{3+} and Bi_8^{2+} , which generally were stabilized in Lewis-acidic environments [6–10,59,60]. There are several peculiar features related to the electronic transitions of these subvalent Bi. First, these species demonstrate not only UV-vis absorption bands, but also NIR ones, whose widths are much broader than those of most RE ions. Second, the oxidation states of these subvalent Bi can be rationally controlled by tuning the composition of the reactants, as shown in Fig. 14.

Although the reports of the synthesis and photophysical properties of subvalent bismuth date back to half a century ago [6–10,59,60], it was not until recently that luminescent properties of these

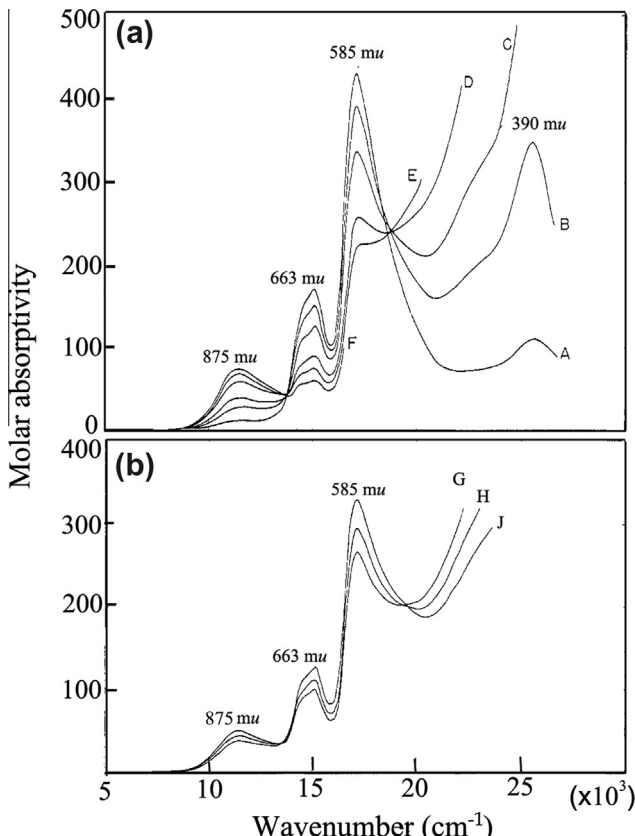


Fig. 14. Spectra of reaction products in the $\text{AlCl}_3\text{-NaCl}$ eutectic at 130°C for various solution compositions. (a) Series of spectra obtained by adding successive amounts of bismuth metal to a solution initially containing 0.117 M BiCl_3 . Values of ME: A, 0.00291; B, 0.00503; C, 0.00715; D, 0.0128; E, 0.0178; F, 0.0259. (b) Series of spectra obtained by adding successive amounts of BiCl_3 to a solution containing 0.00578 M of excess bismuth. Initial molar concentration of BiCl_3 : G, 0.0125; H, 0.0270; J, 0.0588. Reproduced with permission from Ref. [9]. Copyright © 1967, American Chemical Society.

species in liquids were studied. In 2011, Sun et al. found that subvalent bismuth stabilized by Lewis-acidic halogenoaluminate ionic liquids (ILs) shows NIR PL [61]. Raman spectroscopy has been shown to be a powerful tool in the study of compounds containing subvalent Bi, because many bismuth cationic clusters are Raman active [20]. As shown in Fig. 15a, four scattering bands located at 132, 179, 324, and 349 cm⁻¹ were observed. The appearance of 132 cm⁻¹ band suggests that Bi³⁺ exists in the solution since Bi³⁺ usually shows the strongest Raman scattering at ~134 cm⁻¹, attributable to $\nu_1(A_1')$ vibrational mode of Bi³⁺ polycations [20]. UV-vis-NIR absorption spectrum of the solution gives more information on the distribution of subvalent Bi in this system (Fig. 15b). It was found that Bi³⁺ polycations related absorption bands occur at 390, 450 and 870 nm. The band positions are similar to those of Bi³⁺ containing materials such as GaCl₃-benzene and AlCl₃-NaCl systems [20]. In addition to Bi³⁺ related absorption bands, two bands at ~610 and 730 nm were also observed, clearly, which cannot be assigned to Bi³⁺ and Bi²⁺. After thorough comparison of the absorption characteristics of bismuth related active centers, it was found that the appearance of 610 and 730 nm bands can be well explained by the formation of Bi⁺, in the liquid, since Bi⁺ usually displays two strong characteristic absorption bands at ~609 and ~700 nm [20]. The combined evidences of Raman scattering and absorption spectra suggest that, Bi³⁺, alongside with Bi⁺, coexist in the obtained ILs. These subvalent Bi species demonstrate excitation-wavelength dependent NIR emission. When the ILs were excited by 457.9 nm light, corresponding to the electronic transition of Bi³⁺, remarkably broad NIR emission band was observed (Fig. 15c). If the ILs were excited into Bi⁺ absorption band by 690 nm light, a red shift of PL band takes place. This result indicates that multi-type bismuth-related active centers,

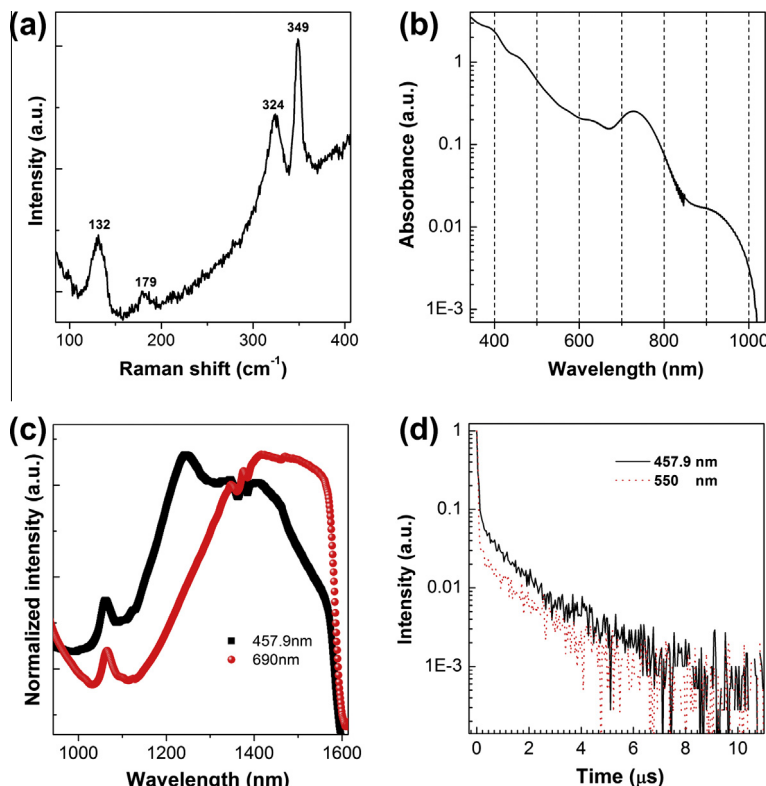


Fig. 15. (a) Raman spectrum of the obtained dark brown ILs containing subvalent Bi. (b) Absorption spectrum of the ILs. (c) PL spectra of the ILs under the excitation of 457.9 and 690 nm. Note that the long-wavelength (>1600 nm) signal is suppressed owing to the drop of InGaAs sensitivity. (d) Decay curves of the ILs at 1250 nm under the excitation of 457.9 and 550 nm. Reproduced with permission from Ref. [61].

rather than singe-type one, exist in the ILs. The experimentally determined PL lifetimes are around 1 μ s (Fig. 15d).

Very recently, Romanov et al. found that Bi NIR emitters could be kept when the chloride liquid becomes bulk glass [62]. This work is intriguing because it bridges the gap between the luminescent liquid and bulk materials containing Bi. In addition to the photophysical properties of liquids containing positively-charged Bi [61], liquid with negatively charged Bi has also been investigated by Dai et al. [28]. Although some techniques such as Raman scattering spectroscopy can be employed for the identification of subvalent Bi, the detailed coordination environments of these species in liquids are not clear in many cases. This is a great barrier for the establishment of the exact structure–property relationship in the liquids containing Bi. By taking advantage of XAS technique, this issue is hopefully solved [115].

5.2. Bi doped amorphous solids

5.2.1. Bulk glasses

Early studies of Bi doped bulk glasses in the 1970s focused on the sensitization of RE ions by Bi^{3+} for lasers [141]. In such a case, it is important to prevent concentration quenching of Bi^{3+} . Therefore, researches on luminescence quantum efficiency of bismuth in various glasses and evaluation of these from the nature of bonding between bismuth and the glass matrices were carried out. Since the discovery of a new broad fluorescence (FWHM: 150 nm, peak at 1150 nm, long lifetime: 650 μ s, quantum yield: 66% with 500 nm excitation) from Bi in SiO_2 glass by Murata et al. in 1999 [142], the investigation on NIR PL from bismuth doped glasses becomes a hot topic. The importance of the NIR PL from bismuth doped glasses has been demonstrated by Fujimoto et al. in 2003 [89]. They discovered a NIR emission from a bismuth doped silica glass and the emission peaking at 1.25 μm with 0.8 μm excitation has a very wide lineshape, the FWHM of which is 300 nm. Meanwhile, the demonstration of an amplification phenomenon in this bismuth-doped silica glass at 1.3 μm with 0.8- μm excitation was shown, and they further pointed out that this infrared emission would be useful as a core material of an optical amplifier at zero-dispersion wavelength. Unfortunately, the transmittance of the glass in the region of 1000–2500 nm was only ~30% at maximum because there were many bubbles in the glass, even though the glass was melted at 1760 °C [88]. Since then, the effect of glass composition, melting atmosphere and co-doping on the infrared luminescent property of various Bi-doped glasses has been studied systematically [62,87,91,92,94,90,93,143–161]. Next section will discuss the photophysical properties of a series of Bi-doped glasses with different compositions.

5.2.1.1. Silica glasses containing a small amount of Al_2O_3 . Silica has laid the foundation of the photonic revolution in the past decades because of its durability and low optical loss over a broad spectral window, and it is still a mainstay of on-a-chip and fiber photonics technology [162–164]. It is a unique material with an unrivalled combination of purity, high temperature resistance, thermal shock resistance, good electrical insulation, optical transparency and chemical inertness. This material is widely used for fiber fabrication, which has a high damage threshold, i.e., a low tendency for phenomena such as laser-induced breakdown.

A bismuth doped silica glass containing a small amount of Al_2O_3 was prepared by melt-quenching method at 1760 °C in air, which showed reddish-brown color [88]. The composition of the glass was Bi_2O_3 : 0.3 mol%, Al_2O_3 : 2.2 mol%, and SiO_2 : 97.5 mol%, which was determined using X-ray fluorescence analysis. A transmittance spectrum is shown in Fig. 16a. There were four main absorption bands at 300 nm (A), 500 nm (B), 700 nm (C), and 800 nm (D) between 200 nm and 2500 nm. There was no luminescence between the visible and infrared regions under excitation at 250 nm, and therefore, the absence of Bi^{3+} luminescence could be confirmed. Broadband NIR luminescence was observed under excitation at 500 nm (Fig. 16b), 700 nm (Fig. 16c) and 800 nm (Fig. 16d). The lifetime detected at 1140 nm was 630 μ s under excitation at 500 nm, which is longer than the lifetime of Bi^{3+} luminescence reported previously.

Interestingly, nanoporous silica glass was applied as a “tolerant” host to stabilize “active” center (bismuth) by Zhou et al. [87]. An alkali borosilicate glass with the composition 61.5 SiO_2 –27 B_2O_3 –8.5 Na_2O –3 Al_2O_3 (in wt%) was used to prepare a nanoporous host by a melt-quenching technique.

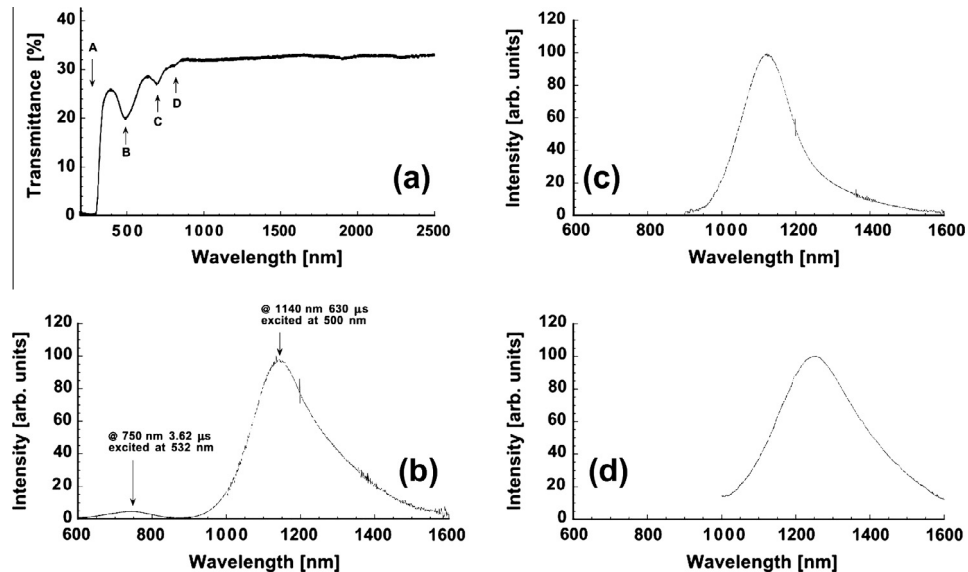


Fig. 16. (a) Transmittance spectrum of bismuth-doped silica glass. (b–d) Luminescence spectra of bismuth-doped silica glass. Excitation at (b) 500 nm, (c) 700 nm, and (d) 800 nm. Reproduced from Ref. [88]. Copyright © 2001, The Japan Society of Applied Physics.

Chemical analysis showed that the proportion of SiO_2 in the porous glass was greater than 96% after phase separation and hot HNO_3 treatment. Bi-doped nanoporous glass was prepared by soaking the nanoporous glass in Bi-containing solutions and then treating it in a special atmosphere. Broad NIR emissions could be observed from the sample treated under Ar atmosphere when excited at 532 nm, 800 nm, and 980 nm. The novel hybrid system by immobilizing active centers in a nanocage structure provides a new platform for the design and fabrication of novel transparent photonic materials. Furthermore, Zhou et al. applied femtosecond laser to irradiate above Bi-doped nanoporous silica glass [165], and proposed that the emission originates from Bi^+ . Owing to the extremely short energy-deposition time, and the elimination of the thermal effect and nonlinear processes enabled by highly localizing laser photons in both time and spatial domains, the reduction processes of $\text{Bi}^{3+} + \text{e}^- \rightarrow \text{Bi}^{2+}$ and $\text{Bi}^{2+} + \text{e}^- \rightarrow \text{Bi}^+$ could be easily controlled by adjusting laser parameters and therefore tuning the concentration of the special active centers. The infrared luminescence can be attributed to the ${}^3\text{P}_1 \rightarrow {}^3\text{P}_0$ electron transition of unusual Bi^+ emission centers.

Recently, for the fabrication of bismuth doped glass fibers as tunable fiber lasers and broadband optical amplifiers, silica glass preform, with a core composition of 2.13 GeO_2 –2.63 Al_2O_3 –95.2 SiO_2 –0.04 Bi_2O_3 (in wt%), was fabricated by modified chemical vapor deposition (MCVD) and solution-doping techniques [166]. Emissions at 1120–1270 nm were observed, which is dependent on excitation wavelengths from 280 nm to 980 nm.

5.2.1.2. Silicate glasses. Realization of laser oscillation in the spectral region between 1150 and 1300 nm from Bi-doped aluminosilicate fiber stimulates detailed investigations on the optical characteristics of Bi-doped silicate glasses. Initially, Suzuki et al. prepared the bubble-free and transparent Bi-doped lithium alumino silicate glasses by melting the mixed raw materials in a Pt-Rh crucible for 2 h at 1873 K in N_2 – O_2 gas flow [147]. It was found that the peak position and width of a broad NIR emission from these glasses could be controlled drastically by the excitation wavelengths. The emission consists of two Gaussian peaks and stimulated emission cross sections at the peaks were calculated to be 7.3×10^{-21} and $2.3 \times 10^{-20} \text{ cm}^2$. The lifetime was 500 μs at 5 K and almost temperature independent up to 350 K.

Meanwhile, Bi-doped alkaline-earth metal silicate glasses and alkali metal silicate glasses were prepared at 1570 °C for 1.5 h in air by Ren et al. [143], in which the relationship between glass host basicity and bismuth NIR luminescence intensity was considered. It was found that increasing the basicity of host glasses resulted in the decrease of NIR PL. Since increasing glass basicity favors the formation of high-valence states of multivalent metal ions, according to the theory proposed by Duffy and Ingram [167], it was believed that bismuth with low-valence states resulted in the infrared luminescence. Furthermore, optical basicities of Na₂O–B₂O₃–SiO₂ system were carefully calculated to analyze the luminescence mechanism by Guan et al. [168]. Visible and NIR luminescence with “boron anomaly feature” in Bi doped sodium borosilicate glasses were observed. As shown in Fig. 17, with the increase of B₂O₃ contents (that is, from sample G1 to G8), the NIR emission first increases and then decreases, with the maximum in sample G5. The decay curve monitored at 1340 nm for sample G5 is presented in the inset of Fig. 17a, and the estimated lifetime is 365 μs. As shown in Fig. 17b, the intensity of the NIR emission at 1340 nm shows the same dependence on B₂O₃ concentration as does the concentration of [BO₄] units. Therefore, [BO₄] units play an important role for the occurrence of NIR luminescence center (labeled as Bi^{x+}). Since each [BO₄] unit possesses a negative charge, an alkali cation or other metallic cation is required to compensate the charge of [BO₄] unit. In the sodium borosilicate glasses, Na⁺ and Bi^{x+} may locate near the [BO₄] unit for charge compensation, and electrostatic interactions could occur between Bi cation and neighboring [BO₄] unit. It is expected that more bismuth with lower valence state will be created with the increase of the number of [BO₄] units in glassy samples.

5.2.1.3. Germanate glasses. Compared with SiO₂-based glass, GeO₂-based glass can be more easily prepared because its melting temperature is evidently lower. Because of the close structural analogy between glassy GeO₂ and SiO₂, it could be inferred that a broad NIR luminescence will exist in bismuth doped germanate glass. Bismuth and aluminum codoped germanate glass was first prepared by Peng et al. using conventional melt-quenching technique at 1550 °C for 20 min in air [94]. The GeO₂: Al, Bi glass samples were reddish brown but transparent and bubble free, with a maximum transmittance of ~80%. The broadband infrared luminescence with maxima at ~1300 nm and a FWHM greater than 300 nm under 808 nm excitation is shown in Fig. 18a. Considering the asymmetric feature of the spectrum, it could be decomposed into four Gaussian peaks with peaks located at 1200, 1300, 1450, and 1600 nm, corresponding to a FWHM of 148, 128, 170, and 94 nm, respectively. Similar result of broadband emission at 1310 nm with a FWHM larger than 400 nm and a fluorescence lifetime longer than 200 μs from Bi/Ta codoped GeO₂ glass at room temperature was also observed (Fig. 18b and c) [93].

Furthermore, Ruan et al. reported that introduction of Tm³⁺ in Bi-doped germanate glass could generate a super-broadband NIR emission with an FWHM of 300 nm (1270–1570 nm) owing to energy

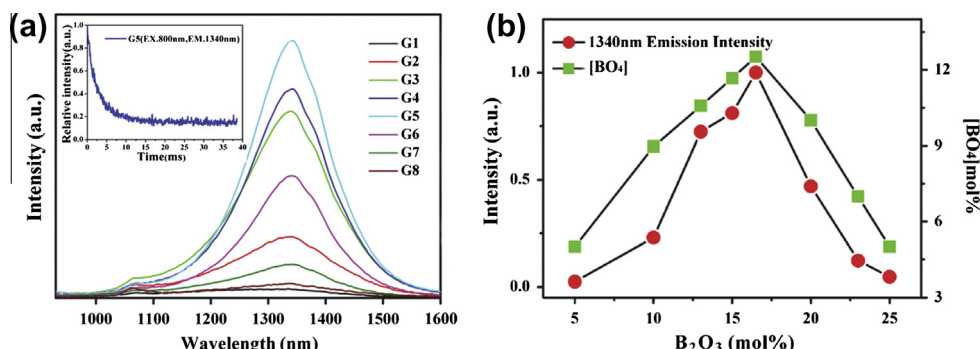


Fig. 17. (a) NIR emission spectra of the samples excited at 808 nm LD. The inset shows NIR fluorescence decay curves of sample G5 (monitoring wavelength is 1340 nm and the corresponding excitation wavelength is 808 nm). (b) Dependence of NIR emission intensity at 1340 nm and [BO₄]% content of the related glasses on B₂O₃ mol%. Reproduced from Ref. [168]. Copyright © 2011, The Electrochemical Society.

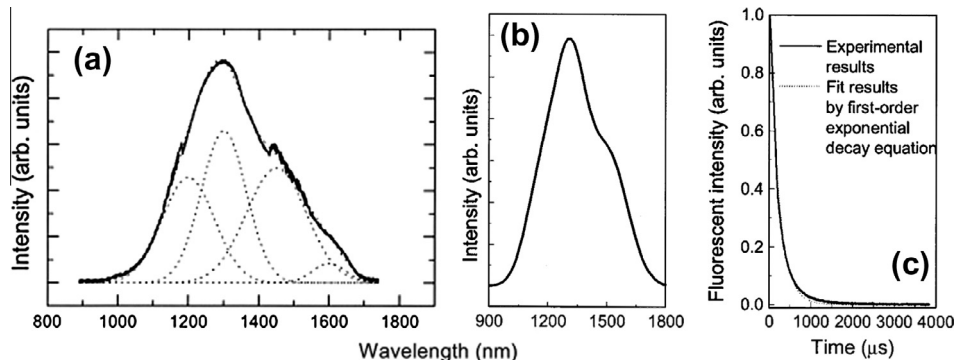


Fig. 18. (a) Fluorescence spectrum of 96GeO₂-3Al₂O₃-1Bi₂O₃ glass pumped by an 808-nm laser. Dotted curves, results of Gaussian fits. (b) Fluorescence spectrum of GTB glass pumped by an 808 nm LD. (c) Fluorescence decay curve of GTB glass pumped by an 808 nm laser diode. The decay was measured by monitoring the emission at 1310 nm at room temperature. The correlation coefficient of the fit by the first-order exponential decay equation ($I = 1.07977e^{-t/222}$) is 0.9956. Reproduced from Ref. [93,94]. Copyright © 2004, 2005, Optical Society of America.

transfer from bismuth ions to Tm³⁺ [169]. The efficient energy transfer from Bi-related centers to Tm³⁺ was confirmed by apparent change of Tm³⁺ emission intensities and fluorescence lifetimes before and after codoping. The highest energy transfer efficiency was estimated to be ~50%. Additionally, it was found that Bi-related NIR emitters can also be produced in other oxide glass systems such as phosphate and borate glasses [91,92].

5.2.1.4. Fluoride glasses. Based on previous studies [6–10,33–35,37,61], subvalent Bi species can be exploited as powerful NIR emitters. Considering the stabilization effect from weakly coordinating ions, fluoride glasses, which are based primarily on Lewis acidic ZrF₄, AlF₃, GaF₃ or InF₃ should be very attractive matrices to stabilize subvalent Bi species. Moreover, it was shown that BiF₃ can be introduced into fluoride glasses with noticeable amounts, producing glasses with compositions ZrF₄-BiF₃-RF (R = Li, Na, K) [170], ZrF₄-BiF₃-BaF₂, ZrF₄-BiF₃-PbF₂ [171] and InF₃-BaF₂-BiF₃ [172], so it seems that only partial reduction of Bi³⁺ to subvalent Bi is needed to convert such glasses to materials with effective NIR PL for applications in telecommunication and laser fields.

From this point of view, bismuth-zirconium-sodium-fluoride glass with composition 45ZrF₄-45BiF₃-10NaF was prepared by Romanov et al. [159]. Stoichiometric mixture of ZrF₄, BiF₃, NaF and NH₄HF₂ was heated to 750 °C within 15 min in closed glassy carbon crucible. NIR PL spectra at different excitation wavelengths show the same lineshape (Fig. 19a) with maxima near 1200 nm. This is in contrast with NIR PL properties of Bi-doped SiO₂ based glasses, whose emission spectra are varying with different excitation wavelengths and several emitting centers were postulated [173–175]. Fig. 19b shows that the NIR PL decay at room temperature is well approximated by linear dependence in coordinates (log(intensity) vs. time^{1/2}). It is the indication that at room temperature the main channel of excited subvalent Bi disappearance is Förster excitation transfer to some quenchers via dipole-dipole interaction.

5.2.1.5. Chloride glasses. To thoroughly understand the real contribution of all subvalent Bi to NIR luminescence in different bismuth-doped materials, chloride glass with composition AlCl₃-ZnCl₂-BiCl₃ was studied by Romanov et al. [62]. The manipulations with the starting chlorides were performed in argon-filled glovebox (<2 ppm H₂O) due to their extreme hygroscopicity. The proper amounts of chlorides (60% molar ZnCl₂, 38% molar AlCl₃, 2% molar BiCl₃, approximately 4 g batch) were placed into L-shaped fused silica cell. The NIR luminescence spectra of subvalent bismuth containing AlCl₃/ZnCl₂/BiCl₃ glass at room temperature and 77 K are shown in Fig. 20a. At room temperature, two bands peaked at 1080 nm and 1300 nm were observed when excited at 532 nm. At 77 K, these two bands in luminescence spectrum became stronger and sharper and another broad luminescence band from 1300 to 2500 nm (maxima at ca. 2000 nm) appears. The PLE spectra of the three bands are shown

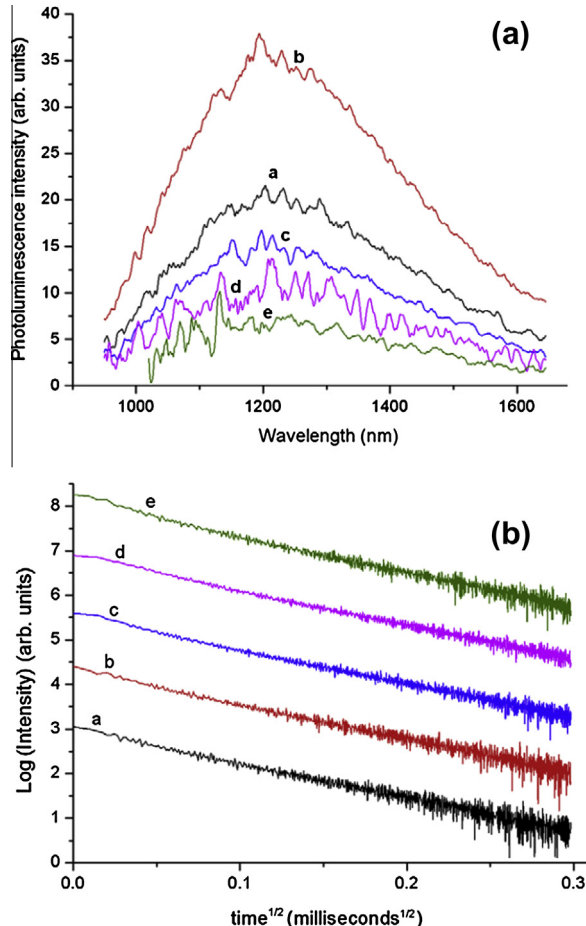


Fig. 19. (a) Spectra of the room temperature NIR photoluminescence from partially reduced $57\text{ZrF}_4\text{-}18\text{BiF}_3\text{-}25\text{BaF}_2$ fluoride glass, excited at different wavelengths: a, 400 nm; b, 430 nm; c, 535 nm; d, 655 nm; e, 700 nm. (b) Temporal decay of NIR photoluminescence at 300 K from partially reduced $57\text{ZrF}_4\text{-}18\text{BiF}_3\text{-}25\text{BaF}_2$ fluoride glass. The luminescence was excited by 10 ns pulse of 532 nm radiation. The decay plots are shown in coordinates ($\log(\text{intensity})$ vs. $\text{time}^{1/2}$) for the emission at different wavelengths: a, 1170 nm; b, 1250 nm; c, 1350 nm; d, 1500 nm; e, 1600 nm. The decay plots are shifted along vertical axis for clarity. Reproduced from Ref. [159] Copyright © 2011, Elsevier B.V.

in Fig. 20b. All excitation spectra rise at $\lambda < 350$ nm due to charge transfer transition of chlorine-coordinated Bi^{3+} followed by energy transfer to all NIR-luminescent species. Besides this common UV feature, the excitation spectrum for the first band, monitored at 1060 nm, consists of two well resolved peaks at 580 and 660 nm, which are well assigned to Bi^+ absorption spectrum in chloroaluminate and chlorogallate systems. The luminescence excitation spectrum of 1300 nm band is represented by the single peak at 580 nm and it may originate from Bi^+ complex: $\text{Bi}^+\text{-nBi}^{3+}$. Finally, the luminescence excitation spectrum for long-wavelength emission at 1900 nm is similar to Bi_5^{3+} absorption spectrum (peak near 800 nm and steep rising at $\lambda < 500$ nm) [33–35]; two peaks assigned to Bi^+ are also present in 1900 nm luminescence excitation spectrum. This fact can be explained by initial Bi^+ excitation followed by energy transfer from excited states of Bi^+ to Bi_5^{3+} polycation. Since the emission behavior of Bi^+ is nearly identical with previous work [8,61], it is believed that Bi^+ is one NIR emitter contributing to signal shorter than 1100 nm. And also, this work is helpful to deepen the understanding of the formation of Bi NIR active centers in solid systems, although more work is needed to further confirm the existence of Bi_5^{3+} .

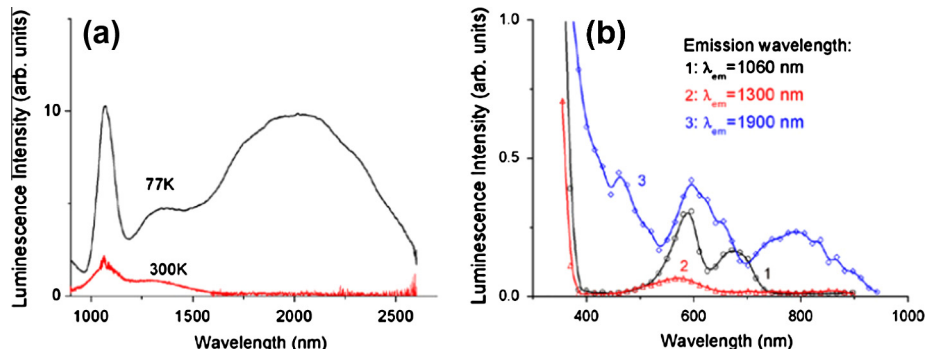


Fig. 20. (a) Photoluminescence spectra of $\text{AlCl}_3/\text{ZnCl}_2/\text{BiCl}_3$ glass, measured at 77 and 300 K (excitation wavelength $\lambda_{\text{ex}} = 532 \text{ nm}$). The spectrum at 77 K composed from two separate measurements: at short waves (with InGaAs detector), and at long waves (with InSb detector); (b) PLE spectra, measured for three luminescence bands. Spectra of the first and the second bands ($\lambda_{\text{em}} = 1060 \text{ nm}$ and $\lambda_{\text{em}} = 1300 \text{ nm}$, respectively) were measured at 300 K. Excitation spectrum of the third band ($\lambda_{\text{em}} = 1900 \text{ nm}$) was measured at 77 K. Reproduced from Ref. [62]. Copyright © 2012, Optical Society of America.

5.2.1.6. Chalcogenide glasses. Chalcogenide glasses exhibit low phonon energy, which allows the observation of certain transitions in RE dopants, or other unusual emissions from V^{3+} and Ti^{3+} which are not observed in traditional glasses [176–178]. Yang et al. gave the first report on the broadband infrared emission of Bi/Dy co-doped chalcogenide glasses [150]. Samples with compositions (mol%) of $70\text{GeS}_2\text{--}9.5\text{Ga}_2\text{S}_3\text{--}20.5\text{KBr}\text{:}0.1\text{Dy}$, $70\text{GeS}_2\text{--}9.5\text{Ga}_2\text{S}_3\text{--}20\text{KBr}\text{--}0.5\text{Bi}_2\text{S}_3\text{:}0.1\text{Dy}$ were melted at different temperatures (melting temperature (MT) = 860, 880, 900, 910, 920, 930, 940 °C) for 10 h in a sealed quartz tube, and then quenched in air. The observed NIR emission showed strong dependence on the MT. Absorption and luminescence spectra of Bi/Dy co-doped glass samples prepared at different MTs (860, 900, 910, 920, and 930 °C) are presented in Fig. 21. In Fig. 21b, the band at 1230 nm could be attributed to Bi ion emission, and 1310 nm originates from the f-f transition of Dy^{3+} ions. The enhanced emissions from both Bi and Dy ions are observed with decreasing MTs, which corresponds well with the increased absorption baselines. The Bi/Dy co-doping can display mutually enhanced emissions. The lower MT favors the formation of low-valence bismuth ions in chalcogenide glasses, which are believed to be the origin of infrared luminescence at 1230 nm. Similar NIR emission at 1260 nm from low-valence bismuth in $80\text{GeS}_2\text{--}20\text{Ga}_2\text{S}_3\text{:}0.5\text{Bi}$ glass was observed by Dong et al. [179].

Subsequently, Hughes et al. reported another Bi-doped chalcogenide glass [149]. The sample was prepared by mixing 70% gallium sulfide, 23% lanthanum sulfide, 6% lanthanum oxide, and 1% bismuth sulfide in a dry-nitrogen purged glove box. The batch was transferred to a furnace using a custom built closed atmosphere transfer pod and then melted at 1150 °C for around 24 h in a silica tube furnace, with an initial ramp rate of 20 °C min^{-1} and under a constant argon atmosphere (flow of 200 ml min^{-1}). The melt was rapidly quenched to form a glass. The glass was then annealed at 400 °C for 12 h. In this sample, emission with a FWHM of 600 nm which is flattened and covers the telecommunication window was observed. The excitation wavelength, QE and lifetime of this emission were 1020 nm, 17% and 160 μs, respectively. The maximum QE was 32% at 900 nm excitation. At cryogenic temperatures, the FWHM reached 850 nm with 974 nm excitation and two new bismuth emission bands at 2000 and 2600 nm were observed. Emission measurements taken with excitation wavelengths of 480–1300 nm revealed four absorption bands at 680, 850, 1020 and 1180 nm. The 1180 nm absorption band was previously unobserved.

5.2.2. Glass fibers

The necessity of expanding the spectral range of fiber optic communication requires the mastering of the second telecommunication window from 1.2 to 1.35 μm, which is characterized by rather low optical losses and a low chromatic dispersion of silica glass. The observation of broadband luminescence in NIR region from 1.1 to 1.7 μm in a number of Bi-doped glasses, as introduced in Section 5.2.1,

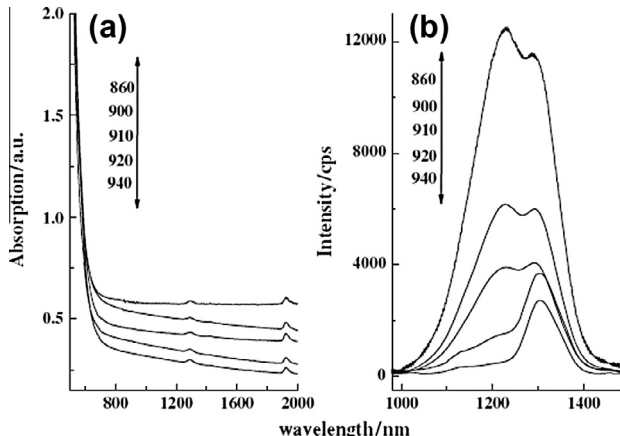


Fig. 21. (a) Absorption spectra and (b) luminescence spectra of $70\text{GeS}_2\text{-}9.5\text{Ga}_2\text{S}_3\text{-}20\text{KBr}\text{-}0.5\text{Bi}_2\text{S}_3\text{:}0.1\text{Dy}$ samples prepared at different melting temperatures (MTs), pumped by 808-nm laser diode. Reproduced from Ref. [150]. Copyright © 2007, The American Ceramic Society.

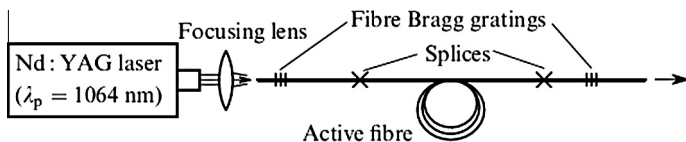


Fig. 22. Laser scheme with a resonator formed by fiber Bragg gratings. Reproduced from Ref. [71]. Copyright © 2005, Kvantovaya Elektronika and Turpion Ltd.

gives rise to the opportunity to prepare a series of novel optical fibers for optical fiber amplifiers and tunable lasers.

The first Bi-doped silica-based optical fibers were fabricated by Dianov et al. [71,180] and Haruna et al. [181] in 2005 using MCVD technique. The core of preforms was formed by CVD of aluminum and silicon oxides. Doping with bismuth oxide was performed by impregnating a porous layer of the core glass with the solution of bismuth salts. The molar concentration of bismuth oxide in the core glass did not exceed 0.1%. The scheme of bismuth fiber laser is shown in Fig. 22. CW lasing was obtained at wavelengths 1146, 1215, 1250, and 1300 nm upon pumping at 1064 nm. The cut-off wavelength of the active fiber was $\sim 1 \mu\text{m}$, and the absorption coefficient at the pump wavelength was 55 dB. Pairs of Bragg gratings with the reflectivities of 3 and 20 dB for the above wavelengths were written in germanosilicate fibers with a cut-off wavelength at $1.1 \mu\text{m}$. The two-mode character of propagation of radiation in these fibers resulted in partial optical losses in splices with the active fiber. The lasing parameters were measured at 1146 nm and 1215 nm. The maximum output power obtained upon pumping by $\sim 5 \text{ W}$ was 460 mW at 1146 nm (Fig. 23) and 400 mW at 1215 nm. The lasing threshold at 1146 nm and 1215 nm were 420 mW and 890 mW, respectively.

Further investigation of such fibers, including a number of samples with new core glass compositions and with improved optical characteristics was reported by Dianov's group [182]. A series of preforms was prepared by CVD with a silica substrate tube (Table 1). Aluminum was used as a dopant in silicate preforms to provide Bi luminescence and to create a core-cladding index difference of 0.006–0.03. Ge and P were added for the study of their influence on the spectroscopic properties of Bi centers. Bi and Al were incorporated by a solution technique or from vapor phase. Other dopants were deposited from the vapor phase. The fibers exhibited broadband luminescence spectra with FWHMs up to 200 nm, corresponding to emission maxima in the region of 1050–1200 nm and lifetimes of about

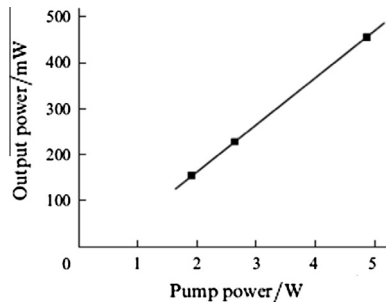


Fig. 23. Dependence of the output power of the fiber laser at 1146 nm on the pump power at 1064 nm coupled to the fiber. Reproduced from Ref. [71]. Copyright © 2005, Kvantovaya Elektronika and Turpion Ltd.

Table 1

Fiber preforms fabricated by MCVD technique, followed by doping Bi and Al. Reproduced from Ref. [184]. Copyright © 2006, Optical Society of America.

Sample	Core glass composition (mol%)	Bi concentration (at.%) doping technique	Loss at 1000 nm (dB/m)
1	88.2SiO ₂ –1Al ₂ O ₃ –6.6GeO ₂ –4.2P ₂ O ₅	<0.02, solution	0.2
4	83.8SiO ₂ –15Al ₂ O ₃ –1.2GeO ₂	<0.02, solution	2.1
5	96.7SiO ₂ –3.3Al ₂ O ₃	0.15, solution	≈20
17	94.2SiO ₂ –5Al ₂ O ₃ –0.8GeO ₂	<0.02, vapor	2.2
25	98.5SiO ₂ –2Al ₂ O ₃	<0.02, vapor	1.06
33	95SiO ₂ –5Al ₂ O ₃	<0.02, solution	1.8
430	75GeO ₂ –19SiO ₂ –5Ta ₂ O ₅ –1P ₂ O ₅	<0.02, vapor	~0.02

1 ms, which makes them become promising media for fiber lasers and amplifiers operating in the second telecommunication window.

To extend the luminescence band of Bi-doped fibers to longer wavelengths, some advances have been made by using glass compositions of fiber cores as follows [183]: (a) alumina-free Bi-doped phosphogermanosilicate glass [184–187]; (b) Bi-doped germanosilicate glass [188]; (c) Bi-doped phosphosilicate glass [193]; (d) aluminogermanosilicate glass and aluminosilicate glass [189,190]. Then, optical properties of a series of Bi-doped fibers were studied [191–196]. There have been many reports in this regard, e.g., first achievement of three-dimensional luminescence spectra for Bi-doped optical fibers with various compositions in a wide spectral range (450–1700 nm) [197], first fabrication of a holey Bi-doped pure-silica optical fiber [198], and first trial of the fabrication of photonic crystal fiber made of bismuth-based glass [199].

5.2.3. Glass films

The birth of dry fiber makes it possible for optical transmission systems to operate over the entire wavelength range from 1260 nm to 1625 nm [200]. Thus, the development of broadband amplifiers and tunable laser sources to cover the 1.2–1.6 μm telecommunication window becomes a key objective to permit the whole optical transmission window of silica fiber to be utilized and to achieve an efficient wavelength-division multiplexing transmission network. This may be the main reason that Bi doped aluminosilicate glasses have received considerable attention during the past years [88]. Clearly, realizing ultrabroad PL in glass films doped with Bi ions is critical for the application of this type of material in integrated photonics.

In 2010, Sun and coworkers successfully realized NIR emission in bismuth glass/Si nanocrystal superlattices [99]. The superlattices were prepared by sputter-deposition of thin Si rich SiO₂ (Si-SiO₂) and Bi-doped aluminosilicate glass layers alternatively on fused quartz substrates by using a multi-target sputtering apparatus. After deposition, the films were thermally treated in N₂ at 950 °C for 20 min. Fig. 24a displays the cross-sectional high-resolution transmission electron microscopy

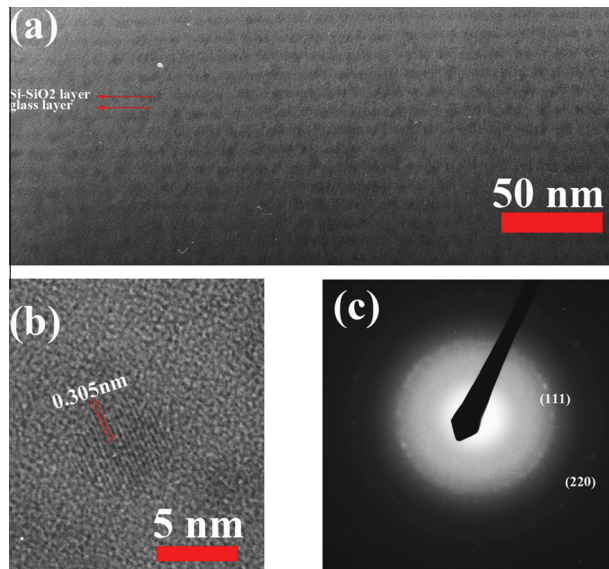


Fig. 24. (a) Cross-sectional HRTEM image of the annealed superlattices. (b) HRTEM image of one individual Si nc with clearly resolved lattice fringe of (111) planes. (c) Electron diffraction pattern of the sample. Reproduced with permission from Ref. [99].

(HRTEM) image of the annealed superlattices, which clearly demonstrates well-preserved layer upon layer structure and some dark regions appear. HRTEM image and electron diffraction pattern taken in the dark region suggest the formation of Si nanocrystals in the superlattices (Fig. 24b and c). It is noteworthy that some nanocrystals form in the interfaces between glass and Si-SiO₂ layers.

As shown in Fig. 25, the emission from the superlattices under 325 nm excitation is much stronger than that from the glass film. It is interesting to note that these two samples demonstrate quite different PL bands. To further elucidate the enhancement mechanism, PL excitation (PLE) spectra of the glass film and superlattices were taken [99]. A broad band peaked at around 500 nm can be observed for the glass film (Fig. 26). Interestingly, the shape of PLE band for the glass film in the range

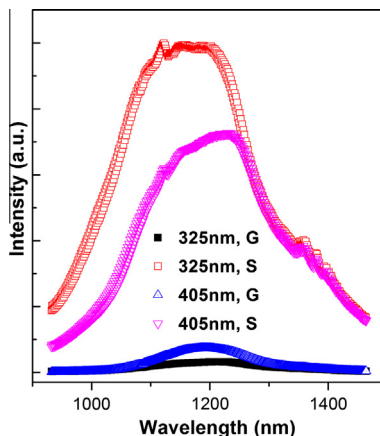


Fig. 25. NIR PL spectra of the annealed glass film (G) and superlattices (S) under the excitation of 325 and 405 nm. Reproduced with permission from Ref. [99].

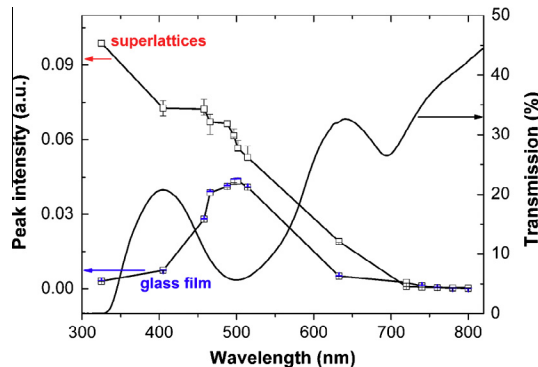


Fig. 26. PLE spectra of the glass film and the superlattices (left scale) and transmission spectrum of the bulk glass with the thickness of 3.6 mm (right scale). We measured the wavelength dependence of NIR PL from the glass film and the superlattices, and the PL peak intensities, divided by the excitation power at different wavelength, were used for drawing the PLE spectra. Note that the lines in the PLE spectra were drawn for guiding the eye. Reproduced with permission from Ref. [99].

of 400–650 nm is quite similar to that of the absorption band for the bulk glass. Thus, the band peaked at 500 nm in the PLE spectrum of the glass film result from the absorption of Bi active centres. In contrast, the superlattices show a completely different PLE spectrum: it shows no distinct structure, indicating that the excitation is not a direct absorption by Bi active centres.

Based on HRTEM, PL and PLE results, the following mechanism for the NIR emission in the superlattices is proposed [99]. Given the size of Si nanocrystals in the superlattices, the band gap energy should be ~ 800 nm. As Bi active centres have broad absorption bands at ~ 700 , 800 and 1000 nm, thus the sensitized excitation of Bi active centres by energy transfer from Si nanocrystals occurs, resulting in the strong enhancement of the PL and very broad PLE band continuously increasing to shorter wavelength; moreover, this sensitization effect leads to broad and flat NIR emission from the superlattices.

The report on the observation of NIR emission in the superlattice structure represents the first work dealing with Bi doped NIR emitting films, which may pave the way for the development of waveguide-type broadband NIR amplifiers [99]. However, this structure has intrinsic drawbacks as follows [99,100]. First, the PL lifetime is $\sim 1 \mu\text{s}$, suggesting abundant defects in it. Second, the glass layer is multicomponent, which limits the thermal processing temperature, since high temperature annealing destroys the structure. Usage of multicomponent glass is also a disadvantage for future integration of the structure into Si optoelectronic devices because of the low compatibility of several elements with the conventional CMOS process. In 2011, Sun and coworkers proposed a simple structure consisting of a very small number of elements which exhibits more efficient and longer-lived luminescence. The structure is Bi-doped Si-rich silica films [100]. Bi-doped Si-rich silica films were prepared by a co-sputtering method. SiO_2 , Si, and Bi-doped silica glass ($\text{SiO}_2:\text{Bi}_2\text{O}_3 = 50:50$ (mol%)) were simultaneously sputter-deposited on fused quartz substrates by using a multi-target sputtering apparatus.

Fig. 27a and b displays the NIR PL spectra for the samples annealed at 900 and 1300 °C, respectively. When excess Si is doped, broad PL emissions appear in the NIR range and the PL intensity strongly depends on Si concentration. This host dependence suggests that excess Si is prerequisite for the formation of NIR active Bi in SiO_2 . It is also found that the spectral shape is influenced by the annealing temperature (T_a). When T_a is low, the FWHM is very large (~ 320 nm), and it becomes sharper at higher T_a . At 1300 °C, the FWHM is 150 nm, which is comparable to those reported for Bi-doped multicomponent bulk glasses [88]. In Fig. 27c, the NIR PL peak intensity is plotted as a function of the excess Si concentration and the annealing temperature. The intensity is the largest when the annealing temperature and the excess Si concentration are ~ 1100 °C and ~ 25 mol%, respectively. Additionally, it was found that the longest decay time is about 700 μs [100]. This value is much longer than those in our previous work on Bi-doped multicomponent glass/Si nanocrystals multi-layers, confirming a higher quality of the present samples [99,100].

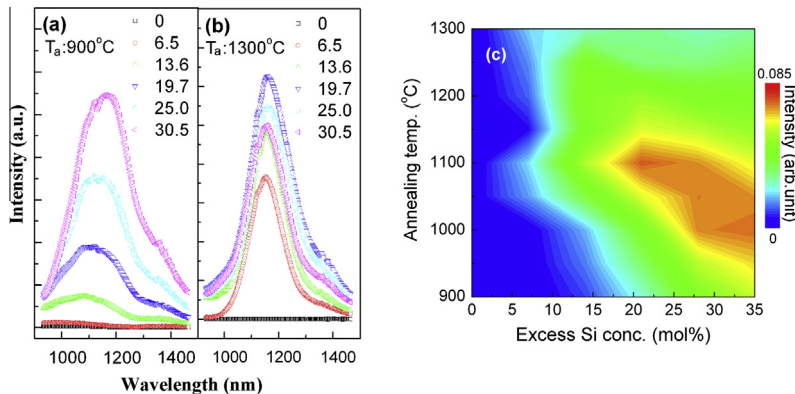


Fig. 27. Typical NIR PL spectra excited at 488.0 nm for the samples annealed at (a) 900 and (b) 1300 °C. Excess Si concentration is changed from 0 to 30.5 mol%. (c) PL peak intensity as a function of the excess Si concentration and the annealing temperature. Reproduced with permission from Ref. [100].

In order to deepen the understanding of the PL behaviors in Bi doped Si-rich silica, visible PL spectra of the samples annealed at 1000, 1100 and 1250 °C were recorded (Fig. 28a–c). Fig. 28d and e plots the PL peak energy and the intensity as a function of the excess Si concentration and the annealing temperature. The PL peak shifts to longer wavelength with increasing Si concentration and T_a . These dependences are very similar to those of Si-rich silica films without Bi doping and are explained by the growth of larger Si nanocrystals in silica. Based on these evidences, the PL is considered to arise from Si nanoclusters, and the shift may be explained by the increase of the size of the clusters. The large width of the PL may be due to large distribution of the size and the structure of Si nanoclusters. PLE results give more information on the energy transfer process in this system. When T_a is 1100 °C, a broad signal monotonously increasing to shorter wavelengths dominates the PLE spectra, indicating that, in addition to the direct excitation, an efficient indirect excitation process exists [100].

The combined evidences suggest that excess Si in silica acts as an agent to activate Bi NIR centers and as energy donors to transfer the excitation energy to Bi active centers [100]. Furthermore, the degree of the interaction between Bi NIR centers and Si nanoclusters depends on the excess Si concentration and the annealing temperature. In particular, this Si-compatible structure greatly relax the requirement of the excitation sources for the realization of some functional applications since it can demonstrate broad excitation bands by tuning some preparation parameters.

Very recently, Morimoto et al. systematically studied the luminescence properties of multilayer structures consisting of Bi-doped silica thin films and different kinds of spacer, i.e., Si, silica, and Si-rich silica layers [201]. The results show that at a low annealing temperature Bi-related NIR active centers form at the interface between Bi-doped silica and Si-rich silica (or silicon) due to the reduction of Bi^{3+} to Bi-related active centers by silicon, while at a high annealing temperature the obtained films show similar emission behaviors to bulk glasses. Interestingly, this approach for obtaining NIR active Bi can be extended for the fabrication of bulk glasses, as obviously revealed by Dai et al. in an independent work [202].

It is noteworthy that high-temperature annealing is required to activate Bi NIR active centers in the superlattices [99,201] or Si-rich silica [100]. For practical applications, room-temperature method for the preparation of films activated by Bi is greatly expected, which is not only important for energy saving, but also presents new routes to tuning Bi active centers and makes it much easier to be integrated with other platforms.

5.2.4. Amorphous nanoparticles

For *in vivo* and deep tissue imaging, NIR emitting nanoparticles offer lots of advantages over visible emitting ones because the absorption and light scattering of biological media and tissue autofluorescence are minimal in the NIR region of the electromagnetic spectrum [203]. Thus, development of

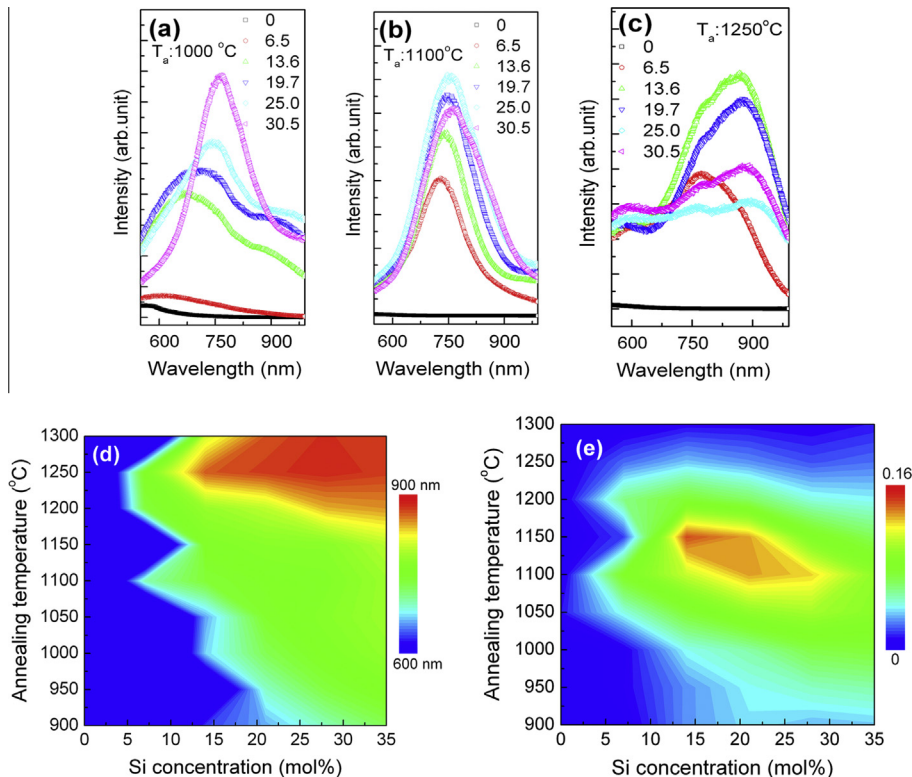


Fig. 28. Typical visible PL spectra excited at 325 nm for the samples annealed at (a) 1000, (b) 1100 and (c) 1250 °C in a N₂ atmosphere. Excess Si concentration is changed from 0 to 30.5 mol%. (d) PL peak wavelength and (e) the intensity as a function of the excess Si concentration and the annealing temperature. In (d), the color bar indicates that the wavelength becomes longer as the color shifts from blue to red, while in (e), it indicates that the intensity is larger as the color shifts from blue to red. Reproduced with permission from Ref. [100].

nontoxic and biocompatible nanoparticles emitting in the NIR region, especially in the second biological window (1.0–1.4 μm) is urgently needed [203]. Bi activated materials demonstrate broad excitation and emission bands in the NIR region [7–10,88]. However, realizing NIR emission in Bi doped materials is challenging owing to the fact that a suitable coordination environment for Bi is prerequisite. In 2011, Sun et al. successfully prepared NIR emitting aluminosilicate nanoparticles by using zeolite as templates [72]. Briefly, well-dispersed nanosized zeolites were prepared, Bi was doped into the pores of zeolites by a simple ion-exchange process, and the powers were thermally treated at a high temperature to obtain Bi active centers. To improve the biocompatibility, finally silica layer was coated outside the particles by a Stöber method.

The as-prepared zeolites are composed of faujasite (Fau) and Linde Type A (LTA) nanocrystals, which shows a broadly distributed size of 53 ± 25 nm and only few of which have a size over 100 nm (Fig. 29a and b). After removal of the tetramethylammonium cation organic template at 580 °C, the crystalline structures were kept well. The bismuth doped zeolites were then annealed at 870 °C in an Ar atmosphere condition and the sample becomes amorphous (Fig. 29c). Fig. 29d clearly shows that nanoparticles are encapsulated by a thin SiO₂ shell with a thickness of ~9 nm. The ratio of the concentrations of nanoparticles to TEOS was optimized to prevent homogeneous nucleation of silica and to control the silica shell thickness of the core–shell nanoparticles [72].

The resulting nanoparticles demonstrate peculiar photophysical properties. Firstly, the nanoparticles display two broad absorption bands covering the visible and NIR regions (Fig. 30a), resulting from

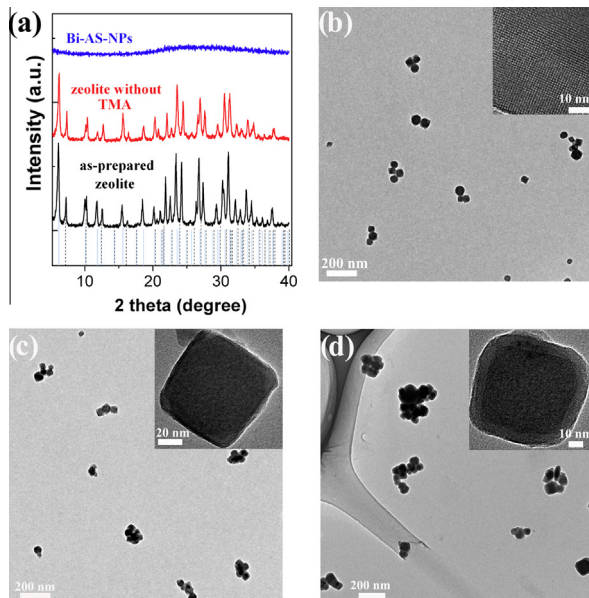


Fig. 29. (a) XRD spectra of the as-prepared zeolites, zeolites removed the template, and Bi doped aluminosilicate nanoparticles. The solid and dotted vertical lines represent the diffraction peaks of Fau and LTA zeolites, respectively. (b) TEM images of the as-prepared zeolites. (c) TEM images of Bi doped aluminosilicate nanoparticles. (d) TEM images of silica coated aluminosilicate nanoparticles. Reproduced with permission from Ref. [72].

the electronic transitions of Bi-related infrared-active centres. Secondly, the NIR emissions of the core–shell nanoparticles, under the excitation of 514.5 and 690 nm, appear in the range of 930–1560 nm (Fig. 30b), and excitation bands occur not only in the visible range of 300–650 nm, but in the NIR region of 650–800 nm. Thirdly, examination of the PL decay curve found that the nanoparticles show an effective lifetime of 232 μ s (Fig. 30c), which is much longer than those of most semiconductor quantum dots and traditional dyes. The quantum efficiency of the nanoparticles dispersed in solution is as high as 14.6%. Fourthly, these nanoparticles exhibit rather great photostability in contrast to fluorescein or the well-known NIR cyanine fluorophores (Fig. 30d).

Until now, there is only one work related to the synthesis of NIR emitting nanoparticles containing Bi for bioimaging [72]. Developing new synthetic methods for obtaining well-dispersed luminescent nanoparticles containing Bi is of vital importance for their applications as biomarkers.

5.3. Bi doped crystalline materials

5.3.1. Halide crystals

Solid state lasers emitting in bands II (2.7–4.3, 4.5–5.2 μ m) and III (8–14 μ m) of the atmospheric transparency spectral range are being developed since at least 15 years ago [204]. Because most of these applications require highly brilliant and/or important peak power laser sources, several RE³⁺-doped low phonon energy (<400 cm⁻¹) chloride and bromide crystals, such as APb₂X₅ (A = K, Rb; X = Cl, Br) or CsCdBr₃, stand out as promising laser gain media in the mid-infrared (MIR) spectral range [205,206]. The main reason that the APb₂X₅ (A = K, Rb; X = Cl, Br) family of laser hosts has triggered a continuous breed of publications since 2001 lies in the non-hygroscopicity of the crystals, which turns out to be unusual among chlorides and bromides host crystals with luminescent properties [207–213].

The first discovery of NIR luminescence from bismuth doped halide crystal was in RbPb₂Cl₅:Bi (RPC:Bi) single crystal [214]. Cylindrical boule, of 60 mm length and 10 mm diameter, of the RPC crystal doped with bismuth was grown by the vertical Bridgman method. The stoichiometric polycrystalline compound of RPC was synthesized by melting high-purity RbCl and PbCl₂ mixture, and then the

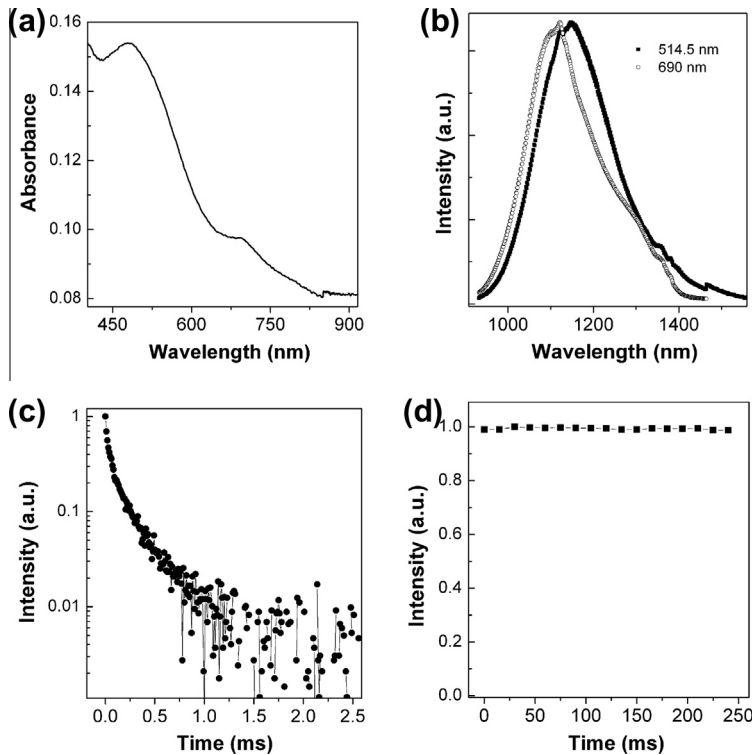


Fig. 30. (a) Absorption spectrum of the core–shell nanoparticles. (b) NIR PL spectra of the core–shell nanoparticles in PBS solution, which were excited by a 514.5 nm line of an Ar⁺ laser and 690 nm light of a laser diode. (c) Decay curve of the core–shell nanoparticles in PBS solution. (d) Photostability evaluation of the core–shell nanoparticles dispersed in a PVP film. The excitation power and spot diameter are 410 mW and 1 mm, respectively. Reproduced with permission from Ref. [72].

obtained compound was purified by the zone-refining technique. The charging material for RPC:Bi crystal growth was prepared by adding either bismuth chloride (BiCl_3) or mixture of metallic bismuth with ammonium chloride to the purified RPC polycrystalline compound. The excitation spectrum was recorded under detection of the signal at 1080 nm, as shown in Fig. 31a. It was found that there are four intense bands in the excitation spectrum at room temperature. The three excitation bands centered at 630, 715, and 767 nm have two weak counterparts at 630 and 715 nm in the room temperature absorption spectrum and five more pronounced counterparts at 637, 659, 701, 735, and 789 nm in an absorption spectrum taken at $T = 4.7$ K. One more band centered at 915 nm was found at cryogenic temperature. Meanwhile, under the laser excitation at 919 nm the same luminescence spectrum as under excitation at 633 and 808 nm was detected. The kinetics of the luminescence was recorded at the wavelength of the luminescence maxima (Fig. 31b). The decay curve had a pure single exponential feature, corresponding to a decay time of 140 μs . All these facts suggest that the NIR luminescence should belong to one luminescence center.

Later on, Bi-doped BaF_2 crystal was also grown by the temperature gradient technique and its spectral properties were investigated by Ruan and coworkers, where two broadband emissions centered at 1070 and 1500 nm were observed [215]. Other halide crystals like CsI have also been systematically studied as host for bismuth to clarify the Bi-related ultra-broadband NIR photoluminescence, and reasonable model has been proposed by Su et al. [216,217]. Interestingly, broad NIR emission was also observed from Bi-doped $\text{Ba}_{10}(\text{PO}_4)_6\text{Cl}_2$ prepared in reductive atmosphere [218].

Recently, Romanov et al. reported the observation of bismuth-related PL in ternary halide crystals KAICl_4 and KMgCl_3 [219], where assignment of the emitting center to Bi^+ was given. The proper

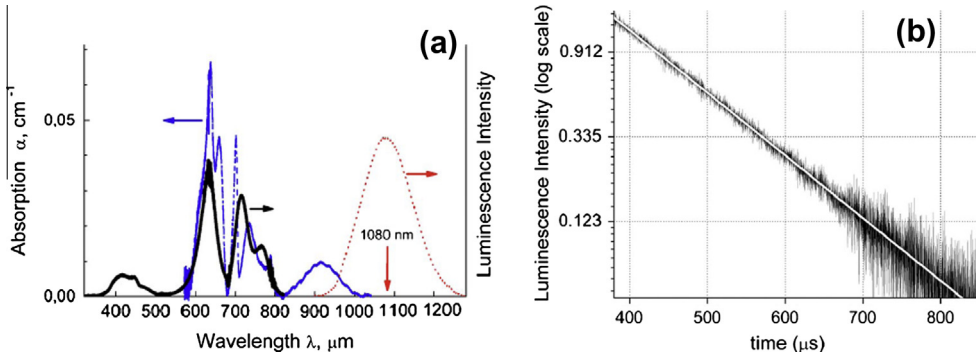


Fig. 31. (a) Absorption spectrum at $T = 4.7$ K, excitation of the luminescence spectrum, and the luminescence spectrum at $T = 300$ K. (b) Kinetics of RPC:Bi luminescence measured under 808 nm excitation, and the exponential approximation. Reproduced from Ref. [214]. Copyright © 2008, Optical Society of America.

amounts of dry chlorides AlCl_3 (99.999%), MgCl_2 (99.99%), KCl (99.998%), BiCl_3 (99.998%) and bismuth metal were mixed in argon-filled glovebox (<2 ppm H_2O) and placed into fused silica cells. Then, the cell was evacuated and sealed at the preformed waist. The cells were heated at 250 °C ($\text{Bi}^+:\text{KAICl}_4$) or 500 °C ($\text{Bi}^+:\text{KMgCl}_3$) until all solids were melted and bismuth metal was consumed. At this point the transparent colored liquid had formed. This melt was slowly cooled to room temperature, forming desired ternary chloride phases. The luminescence spectrum of doped KAICl_4 crystals along with luminescence excitation spectrum is shown in Fig. 32. The shape of luminescence spectrum was independent on excitation wavelength. The temporal decay was single exponential with lifetime of 525 μs at room temperature. The characteristic two-peaked luminescence excitation spectrum is similar to Bi^+ absorption spectrum in chloroaluminate melts [9] and to Bi^+ luminescence excitation spectrum in $\text{AlCl}_3/\text{ZnCl}_2/\text{BiCl}_3$ glass [62]. All these arguments help to infer that single NIR luminescent Bi^+ center was contained in KAICl_4 . As the ionic radius of Al^{3+} is too small to permit the substitution with any possible bismuth valence state, the only remaining possibility is the isomorphous substitution of Bi^+ for K^+ . The observation of NIR luminescence in Bi^+ doped KAICl_4 opens the possibility to design other potassium-containing Bi^+ -doped crystals for potential laser action. To investigate this possibility, Bi^+ -doped KMgCl_3 was crystallized from melt with composition: 54.5% mol MgCl_2 , 44.5% mol KCl , 1% mol BiCl_3 . Bi metal was also added in proportion $\text{Bi}/\text{BiCl}_3 = 0.03$. The prepared $\text{Bi}^+:\text{KMgCl}_3$ ternary chloride also demonstrates NIR luminescence (Fig. 32), similar to $\text{Bi}^+:\text{KAICl}_4$, but slightly blue-shifted. The luminescence excitation spectrum is also similar to $\text{Bi}^+:\text{KAICl}_4$, but relative intensities and positions of

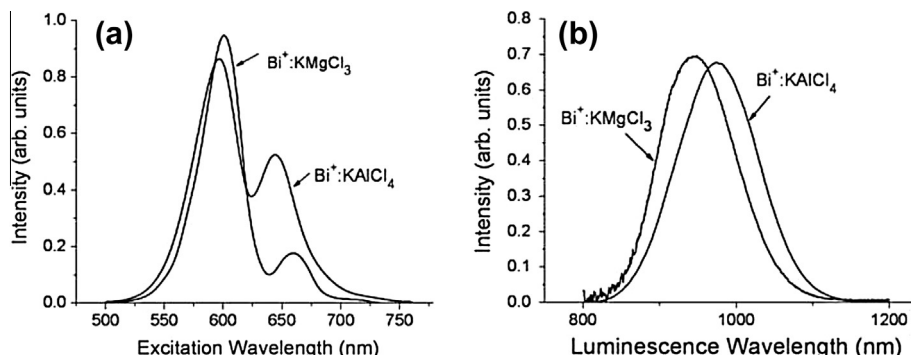


Fig. 32. Luminescence excitation spectra (a) and photoluminescence (b) spectra of $\text{Bi}^+:\text{KAICl}_4$ and $\text{Bi}^+:\text{KMgCl}_3$ ternary chloride crystals at room temperature. Reproduced from Ref. [219]. Copyright © 2012, Elsevier B.V.

two peaks are somewhat different. Two peaks in excitation spectrum are red-shifted relative to $\text{Bi}^+:\text{KAlCl}_4$. The lifetime of $\text{Bi}^+:\text{KMgCl}_3$ luminescence was $\sim 400\ \mu\text{s}$ at room temperature. It is evident that the same Bi^+ center (but in different crystal lattice) cause the luminescence in this case. Furthermore, it was found that the emission behavior of $\text{Bi}^+:\text{KAlCl}_4$ strongly depends on the temperature; lower temperature favors a narrow and blue-shifted emission band [220]. The systematic results reported by Romanov et al., in combination with an earlier report on the observation of NIR PL signal in ionic liquids [61], indicate that Bi^+ is one NIR emitter with emission peaks shorter than 1100 nm.

5.3.2. Zeolites crystals

Zeolites are aluminosilicate molecular sieves with pores of molecular dimensions. In recent years, their potential as host materials for luminescent guest species has been evaluated, and the corresponding results prove that appropriately functionalized zeolites and related structures are a promising new class of luminophores [221]. Since 2009, Sun et al. have found that this porous structure is an excellent host for NIR active Bi [37,221–224]. Depending on the preparation methods used, it can be classified as two groups, i.e., Bi embedded zeolites thermally treated at a high temperature and prepared in a high-vacuum condition.

5.3.2.1. Bi embedded zeolite Y and sodalite thermally treated at high temperatures. In 2009, Sun et al. reported a facile and novel strategy to realize strong, air-stable, long-lived, ultrabroadband and tunable NIR PL from Bi embedded faujasite-type zeolites and their derived amorphous nanoparticles [221]. As displayed in Fig. 33a, all samples show strong ultrabroadband emission from 930 to 1630 nm with a FWHM of 160 nm. The peak wavelength is at 1145 nm. With increasing temperature, the PL intensity monotonously increases (Fig. 33a and d). It is also found that the PL shows spectral tunability: the peak wavelength and shape of PL closely depend on the excitation wavelength (Fig. 33a and b). In the mother zeolites, NIR PL under the same excitation condition was not observed, indicating that the PL is from bismuth-related infrared-active centres instead of intrinsic structural defects of zeolites. Fig. 33c demonstrates the fluorescence decay curves of the annealed products. The $1/e$ lifetime at 300 K increases from 80 ns to 430 μs from 800 to 1000 °C (Fig. 33d).

Additionally, the zeolites annealed at 900 and 950 °C display three strong and broad bands with maximum at around 430, 540, 710 nm and a weak band at 630 nm, while that annealed at 800 °C only displays two broader bands with maximum at 530 and 715 nm [221]. Thermogravimetric analysis reveals that the water content in the annealed zeolites decreases notably with increasing annealing temperature. Based on the lines of evidences described, it was proposed that Bi acts not only as luminescence active centres, but as blocks of selectively closing down the ‘in-out windows’ of water molecules, i.e. bismuth active centres can be sealed in a low-vibrational environment by bismuth agglomerates even when the sample still contains a large amount of water (Fig. 34). Besides, it is found that efficient superbroad NIR luminescence can be realized in Bi doped high-silica nanocrystalline zeolites thermally treated in N_2 atmosphere [222], and the emission intensity is closely related to the Al/Si ratio (the larger the Al/Si ratio, the stronger the emission) [221,222,225]. Furthermore, compared with zeolites with more Al, Bi-doped high-silica zeolites do not show remarkable absorption bands, resulting from the low-concentration active Bi in it [221,222]. All reported results suggest that high-temperature annealing in an inert atmosphere is one feasible route to obtaining NIR active Bi in this porous structure, and that thorough investigation of Bi doped zeolites Y with higher Al concentration may lead to a much clearer picture on the emission mechanism in this system.

In a subsequent study, to gain a more detailed insight into NIR PL mechanism and Bi distribution in the as-annealed and hydrated Bi-embedded zeolites, these samples were characterized by using extensive techniques including UV-vis-NIR diffuse reflectance, Raman, and steady-state NIR PL spectroscopy [224]. In particular, Raman spectra give abundant information on the distribution of Bi. As shown in Fig. 35, FAU zeolites display characteristic scattering bands in the range of $200\text{--}600\ \text{cm}^{-1}$. These bands can be assigned to T-O-T bending modes (T is Si or Al). New bands develop at 138 and $160\ \text{cm}^{-1}$ for Bi doped zeolites thermally treated in air and Ar atmospheres. It was reported that most cationic bismuth clusters show their characteristic scattering peaks. For instance, Bi_5^{3+} shows the strongest Raman scattering at $\sim 134\ \text{cm}^{-1}$ [20]. It is noteworthy that bismuth compounds can also display bands in the low-frequency range of $100\text{--}200\ \text{cm}^{-1}$. It was revealed by Denisov et al. that Bi_2O_3

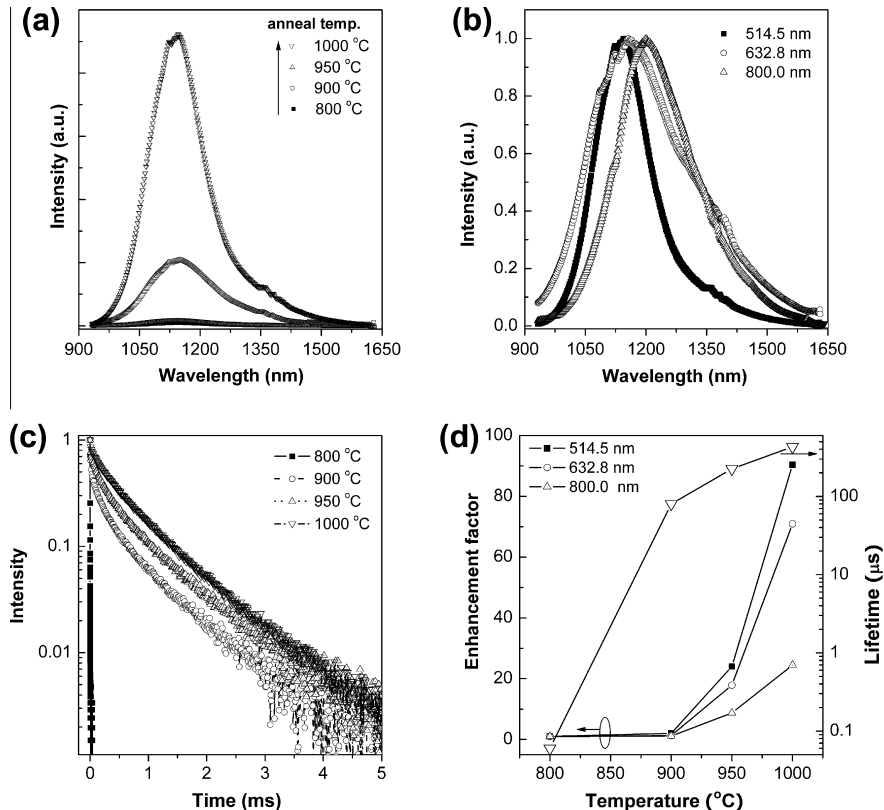


Fig. 33. (a) Ultrabroadband NIR PL spectra of the zeolites annealed at the indicated temperature in Ar atmospheric condition, which were excited by a 514.5 nm line of an Ar⁺ laser at a power of 0.014 mW. (b) Normalized NIR PL of the sample annealed at 1000 °C under 514.5, 632.8 and 800 nm excitation. (c) Fluorescence decay curves of the annealed samples at 300 K. The detected wavelength is 1145 nm. (d) (left axis) Annealing temperature dependence of enhancement factor of PL when excited by 514.5, 632.8 and 800 nm. Enhancement factors at different excitation wavelength were calculated by dividing integrated PL intensities at different temperature by that at 800 °C; (right axis) Temperature dependence of 1/e lifetime at 1145 nm. Reproduced with permission from Ref. [221].

shows strong Raman scattering at ~ 138 and ~ 150 cm⁻¹ [226]. It is found that both NIR active and inactive zeolites doped with Bi show Raman bands at nearly identical frequencies. This indicates that the 138 and 160 cm⁻¹ bands are mainly attributable to Bi₂O₃ instead of Bi active centers such as Bi₅³⁺. These results suggest that Bi₂O₃ clusters form in the zeolites, which can act as blocks for separating Bi active centers from O₂ and H₂O. In Ref. [224], Sun et al. first tentatively proposed that Bi polycations such as Bi₅³⁺ may be one optically active center, based on the observation of some absorption bands in the range of 400–450 nm [221,224].

Since the sodalite cages are rather important for the stabilization of NIR active Bi, Sun et al. further studied the NIR emission in bismuth-embedded sodalite nanocrystals by using steady-state and time-resolved PL and Raman scattering spectroscopy [223]. Bi-X-Y samples demonstrate annealing-temperature and concentration dependent PL (Fig. 36), where X and Y are bismuth molar ratios and annealing temperatures, respectively. With increasing annealing temperature, the NIR emission of Bi-0.6-Y series, peaked at ~ 1146 nm, first increases and then decreases; Bi-0.6-925 sample displays the strongest emission (Fig. 36a). It is found that Bi-1.33-Y series show quite different PL evolution in comparison to Bi-0.6-Y ones (Fig. 36b and c): when annealing temperatures are not higher than 875 °C, the samples display NIR emission with a peak wavelength of 1146 nm. Further increase of temperature results in a

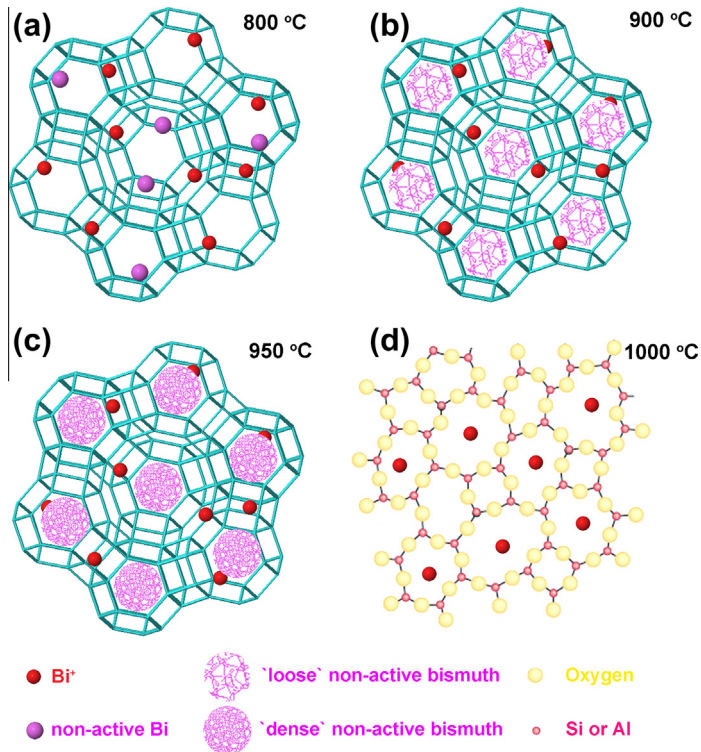


Fig. 34. Schematic illustration of the structure transformation of the zeolites annealed at different temperatures. (d) shows the 2-dimensional representation of the structure of an aluminosilicate network. Note that 'loose' and 'dense' just represent small and large possibilities of sealing the pores of zeolites by bismuth agglomerates. Reproduced with permission from Ref. [221].

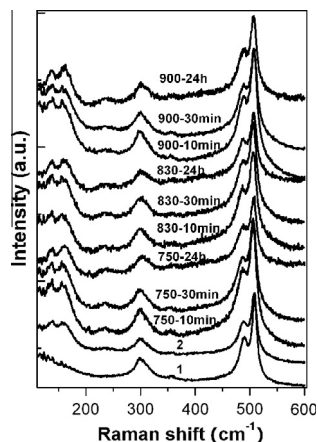


Fig. 35. Raman spectra of the samples annealed at 750, 830, and 900 °C. The products were denoted as $x-y$, where x and y represent the annealing temperature and exposure time in air, respectively. The mother zeolites (1) and Bi doped zeolites (2) annealed at 750 °C in air were used as references. Unfortunately, Raman spectra of the dehydrated samples suffer from strong fluorescence and Raman bands cannot be identified. Reproduced with permission from Ref. [224].

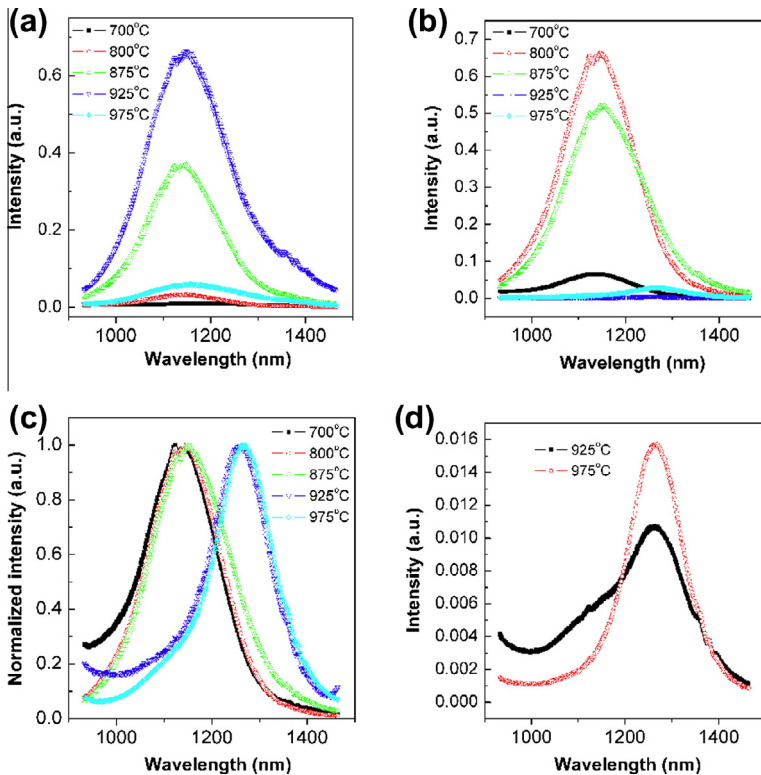


Fig. 36. (a) NIR PL spectra of Bi-0.6-Y samples. (b) NIR PL spectra of Bi-1.33-Y samples. (c) Normalized PL spectra of Bi-1.33-Y samples. (d) NIR PL spectra of Bi-2.13-925 and Bi-2.13-975 samples. PL measurements were carried out with the excitation of 488 nm line of an Ar⁺ laser. Note that the spectra in (a), (b) and (d) were taken under the same excitation condition and vertical labels represent the PL intensities; Bi-2.13-Y (Y = 700, 800, and 875) samples do not show PL. Reproduced with permission from Ref. [223].

red shift of peak wavelength of ca. 120 nm. Bi-2.13-925 and Bi-2.13-975 samples also display this kind of NIR emission (Fig. 36d). This result indicates that not only thermal treatment, but also bismuth concentration in hosts is an important parameter affecting Bi active centers.

Although Raman scattering results give new insight on Bi active centers in zeolite pores [223], the exact PL mechanism is still not clear because of the lack of structural analysis of such systems. It is obvious that the critical issue involves the unknown local coordination environments of Bi in zeolite frameworks [221–225]. This is a great obstacle to the understanding of Bi-related NIR emission behaviors.

5.3.2.2. Bi embedded zeolite Y thermally treated in high-vacuum condition. To obtain a clearer picture on the distribution of Bi in zeolite Y framework, Sun et al. employed high-resolution synchrotron XRD at the BL15XU NIMS beam line of SPring-8 to obtain high-quality diffraction patterns of dehydrated zeolite Y prepared by a vacuum-annealing method [37]. Crystal structure refinement by Rietveld method has been performed using the software package GSAS [105] (Fig. 37). Based on the refinement result, the total amounts of Na and Bi per unit cell are 26.0(3) and 8.4(0), respectively, which are in good accordance with those determined by ICP-OES analysis. Obviously, Bi occupies single-type site in the sodalite cages, which is coordinated to three oxygen atoms of the base of the prism. Taking the ionic radius of the O²⁻ to be 1.32 Å, the radius of Bi was calculated to be 1.465 Å, indicating that the valence state of Bi is +1. This means that, if Bi⁺ occupies all four sites S_V in the sodalite cage, then

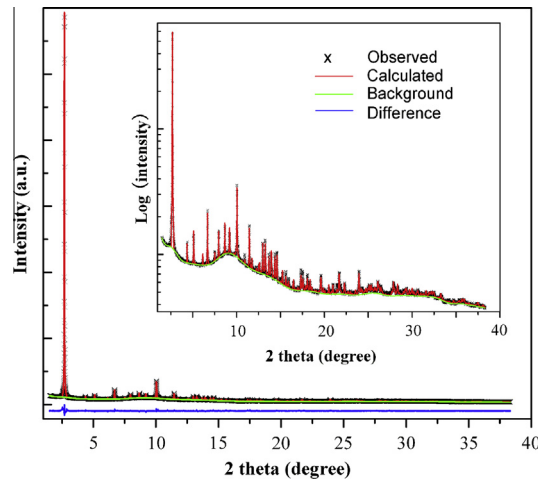


Fig. 37. The Rietveld fit to the high-resolution synchrotron XRD pattern of dehydrated Bi embedded zeolite Y. Plots show the observed and calculated powder patterns. A difference curve is shown at the bottom of the diagram. The inset shows a logarithmic-scale version of the graph. Reproduced with permission from Ref. [37].

approximately 26.3% of the sodalite cages will contain Bi_4^{4+} . However, owing to the low loading level, it is possible that these sites I' are only partially occupied by Bi^+ . That is, depending on the occupancy probability, Bi^+ has chances to form the substructures of Bi_n^{n+} ($n = 1\text{--}4$) in the sodalite cages, where n stands for the number of Bi^+ per sodalite cage [37].

The sample displays a broad emission band from 932 to 1600 nm under the excitation of 488 nm, with a peak wavelength at 1150 nm and a FWHM of 230 nm (Fig. 38). It was found that the emission lineshape of this sample strongly depends on the excitation wavelength; the peak wavelength shifts to 1247 nm when the sample was excited by 786 nm light. In combination with XRD analysis, it is believed that this excitation-wavelength dependent down-converted NIR emissions result from the coexistence of multi-type Bi^+ substructures in the zeolite framework.

To shed light on the origin of the PL from Bi^+ containing dehydrated zeolite Y, quantum chemistry calculations using the ADF program package were performed [37]. The experimentally determined geometries of Bi_n^{n+} ($n = 2, 3$ and 4) obtained from the XRD refinement were used for the following calculations. Spin-orbit coupling was taken into account for all calculations. The calculated absorption

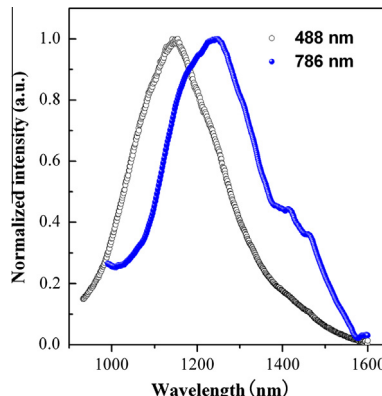


Fig. 38. Steady-state PL spectrum from the dehydrated sample under the excitation of 488 and 786 nm. Reproduced with permission from Ref. [37].

spectra of Bi_4^{4+} , Bi_3^{3+} and Bi_2^{2+} in the sodalite cage are displayed in Fig. 39. It is noted that Bi_4^{4+} unit displays intense high-energy bands, with peaks at 548, 626, and 968 nm, whereas forbidden-like ones at 1237 and 1265 nm (Fig. 39a). Similar phenomena are also observed for Bi_3^{3+} and Bi_2^{2+} units (Fig. 39b and c). The feature of electronic transitions of Bi^+ could be obtained through the analysis of the absorption spectrum of Bi^+ in $\text{AlCl}_3\text{-NaCl}$ molten salt [6]. All these experimental and theoretical evidences obtained indicate that the observed NIR emission was from the electronic transitions of the substructures of Bi^+ in the sodalite cage of zeolites Y.

It is noteworthy that, for the first time, this work presents direct experimental evidence on the formation of Bi^+ in solid materials through the analysis of high-resolution synchrotron powder XRD data. Furthermore, it was revealed that the substructures of Bi^+ residing in the sodalite cages contribute to the observed ultrabroad and tunable NIR PL [37]. This work not only inspired great interest in the exploration of more generic evolution rules of Bi oxidation states, but also raised new possibilities for the design and synthesis of novel photonic material systems using charged elemental clusters as optically active centers. It is noted that zeolites can be exploited as templates accommodating Bi and other kind of active centers such as rare earth ions. In such a case, energy transfer occurs easily between these centers, making it possible to excite rare earth ions by broadband optical sources [227–230].

5.3.3. Oxide crystals

The first bismuth-doped oxide single crystal which shows NIR luminescence was SrB_4O_7 [231]. Indeed, this crystal was reported to be host crystal for realization of unique orange-red luminescence

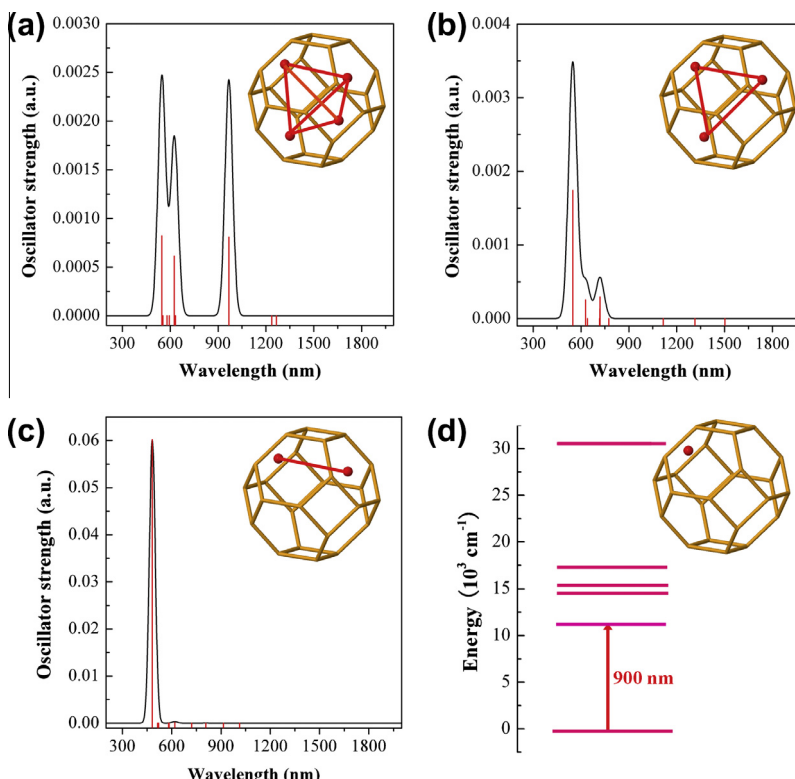


Fig. 39. Theoretical absorption spectra for Bi_4^{4+} (a), Bi_3^{3+} (b) and Bi_2^{2+} (c). Note that the red vertical lines in (a), (b) and (c) are the oscillator strengths corresponding to specific transitions of Bi_4^{4+} , Bi_3^{3+} and Bi_2^{2+} units, respectively. The energy level diagram of Bi^+ shown in (d) was drawn according to the experimental absorption spectrum of $\text{AlCl}_3\text{-NaCl}$ molten salt containing Bi^+ (Ref. [6]). Reproduced with permission from Ref. [37].

of Bi^{2+} [39]. Moreover, SrB_4O_7 compound has a congruent melting point, which can be prepared with the forms of both glass and single crystal. Bi-doped SrB_4O_7 compounds were synthesized by solid-state reaction at 850 °C in N_2 atmosphere for 5 h. Platinum crucible was used. Polycrystalline Bi-doped SrB_4O_7 materials were prepared through cooling the melting in N_2 atmosphere at the rate <5 °C/h. SrB_4O_7 crystals were grown in N_2 atmosphere by the conventional Czochralski method [231]. The powder was put into a platinum crucible 60 mm in diameter and 80 mm in height. Platinum wire was used as seed, and the pulling and rotation rates were 0.1–0.3 mm/h and 5–20 rpm. As a result, NIR-emission could be observed from the polycrystalline material, but not from single crystals, suggesting that emission centers may exist at grain boundaries.

Su et al. subsequently investigated the spectroscopic properties of as-grown and γ -irradiated Bi-doped $\alpha\text{-BaB}_2\text{O}_4$ ($\alpha\text{-BBO}$) single crystals [232]. The Bi-doped $\alpha\text{-BBO}$ single crystals were grown by traditional Czochralski method in a N_2 atmosphere. NIR emission was observed only in the irradiated Bi: $\alpha\text{-BBO}$ crystals, peaking at 1139 nm with an FWHM of 108 nm, accompanied with a shoulder at about 1350 nm, as shown in Fig. 40a, under excitation of 808 or 980 nm. The decay curve of the

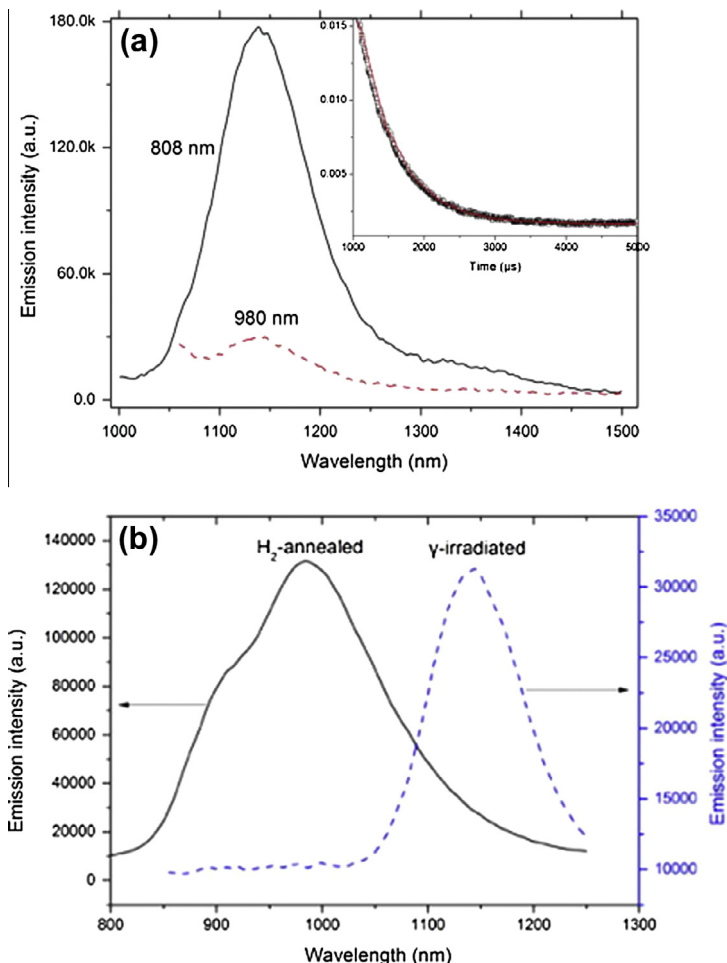


Fig. 40. (a) NIR emission spectra of the γ -irradiated $\text{Bi}:\alpha\text{-BBO}$ crystal upon 808 nm and 980 nm LDs exciting, respectively. The inset is the decay curve of the emission at 1139 nm. (b) NIR emission spectra of H_2 -annealed and γ -irradiated $\text{Bi}:\alpha\text{-BaB}_2\text{O}_4$ crystals under excitation of 808 nm LD. Reproduced from Ref. [232,233]. Copyright © 2009, 2010, Optical Society of America.

emission at 1139 nm is shown in the inset of Fig. 40a, which can be fitted with the first-order exponential mode with lifetime of 526 μ s. The most probable mechanism for the NIR emission in the γ -irradiated Bi: α -BBO crystal should be Bi $^{+}$. Under γ -irradiation, the electrons can be easily released from the defect centers of V $_{\text{Ba}}$ ⁺ and would freely drift in the lattice. Then Bi $^{3+}$ ions could capture free electrons and turn into Bi $^{2+}$, further Bi $^{+}$, accompanied with the production of a new center of V $_{\text{Ba}}$ ⁺. The involved process can be expressed as V $_{\text{Ba}}$ ⁺ \rightarrow V $_{\text{Ba}}$ + 2e, Bi $^{3+}$ + e \rightarrow Bi $^{2+}$, and Bi $^{2+}$ + e \rightarrow Bi $^{+}$. To study the thermal stability of the NIR luminescent centers (i.e., Bi $^{+}$ ions), heat annealing in N₂ atmosphere at 500 °C was performed for 3 h on the γ -irradiated Bi: α -BBO crystal. No NIR emission can be observed after annealing under excitation of 808 or 980 nm LD. This indicates that the trapped electrons in Bi $^{+}$ ions can be released by thermal activation, which would be recaptured by V $_{\text{Ba}}$ ⁺ centers. That is, the Bi $^{3+}$ in α -BBO crystal is a shallower electron trap relative to V $_{\text{Ba}}$ ⁺ centers.

The same luminescent phenomenon of this Bi-doped α -BBO crystal was also observed by Xu et al. [233]. γ -irradiation, electron-irradiation and H₂-annealing are effective methods to produce NIR luminescence in Bi: α -BaB₂O₄ crystal, which produce free electrons in crystal lattice to reduce Bi $^{3+}$ ions to low-valence. As shown in Fig. 40b, heat-annealing in H₂ atmosphere succeeded in producing broadband NIR luminescence in Bi: α -BaB₂O₄ crystal, with center wavelength of 985 nm and FWHM of 187 nm under excitation of 808 nm LD. For comparison, the central wavelength and FWHM of γ -irradiated Bi: α -BaB₂O₄ crystal were 1140 nm and 108 nm, respectively. Other Bi-doped alkaline earth oxide crystals, like Ba₂P₂O₇ [234] was studied by Peng et al. The luminescence peaks around ~1.1 μ m with a FWHM of ~140 nm and a lifetime of >600 μ s from two different lattice sites. NIR emission centers can be generated and removed reversibly by treating the polycrystalline material in CO atmosphere or air, respectively, at 1100 °C. This reveals directly lower valence bismuth as NIR emission centers.

Using γ -irradiation method, Xu et al. investigated the broadband NIR luminescence in Bi-doped Y₄GeO₈ Crystals [235]. Doped and un-doped samples of Y₄GeO₈ were prepared via solid state reaction. Samples were synthesized by the following steps: (a) sintering at 1350 °C for 4 h in air; (b) after synthesized according to (a), the samples were exposed to γ -ray from a ⁶⁰Co source with a dose rate of 100 Gy/h for total doses of 10 kGy at room temperature; (c) the samples were synthesized according to (a) and (b), then they were thermally treated at different temperature (100, 200, 300, 350 °C) in N₂ atmosphere for 2 h. Sample nomenclature is XA, XR or XRT, whereby "X" represents the concentration of Bi in mol% (0, 0.25, 0.5, 0.75, 1.0, 2.0, 3.0), "A", "R" and "RT" mean that the samples were synthesized according to ways (a), (b) and (c), respectively, "T" is thermal treatment temperature in path (c) (T = 100, 200, 300, 350 °C). Fig. 41a shows XRD patterns of Y_{4(1-X)}GeO₈:4xBi, which are consistent with JCPDS card 21–1446. XRD results show the synthesized phosphors are of pure phase, which has an orthorhombic unit cell structure. No phase change occurred in the samples after γ -ray irradiation. A slight shift of the peak position for $2\theta = 29.77^\circ$ to a smaller diffraction angle is detected from the pattern of 1A compared with that of 0.5 A (inset of Fig. 41a). This indicates the increase of lattice parameters with more Bi $^{3+}$ in the crystals, confirming the assumption that some Y $^{3+}$ ions (1.02 Å) are replaced by Bi $^{3+}$ ions (1.17 Å).

NIR emission spectra are shown in Fig. 41b. Bi-doped samples after γ -ray irradiation exhibit broad NIR photoluminescence at 1155 nm. The FWHM of sample 1R is 330 nm, which is similar to that of Bi-doped germanate glasses [236]. The peak position remains unchanged with changing dopant concentration. The inset shows the relation between the emission intensity and nominal Bi concentration, maximum intensity appears at the concentration of 1 mol%. NIR emission intensity depends strongly on the thermal treatment temperature. As the temperature goes up from 100 to 350 °C, the NIR emission becomes weaker and weaker and disappears at 350 °C. There is no NIR emission in sample 0R, 1A and 1R350. Examination of the luminescence behavior of Sample 1RL shows that no apparent change was observed after preserving sample in air at room temperature for 2.5 months, indicating the γ -ray induced luminescence is stable at room temperature.

As shown in Fig. 41c, no apparent ESR signal can be detected in γ -ray unirradiated samples 0A and 1A, while the γ -ray irradiated sample 0R shows signals at g₁ = 2.008 and g₂ = 1.993, which are attributed to holes and free electrons generated in the host matrix, respectively. In the sample 1R, the signals at g₁ and g₂ vanish and decrease compared with those of un-doped sample. Generally, multivalent ions can act as both electron and hole trapping center. Based on this, it is inferred that most holes and

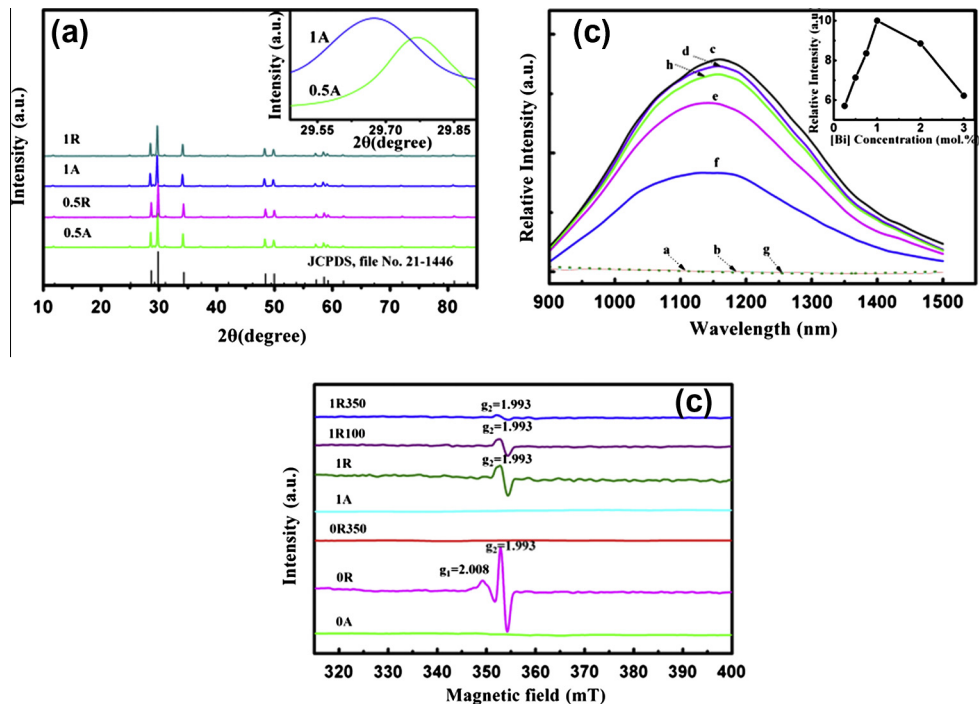


Fig. 41. (a) XRD patterns of γ -ray unirradiated and irradiated samples (0.5A, 0.5R, 1A, 1R) and Standard JCPDS card 21-1446. The inset shows enlarged (500) diffraction peak of 0.5A and 1A. (b) NIR emission spectra of (a) 1A, (b) OR(dot line), (c) 1R, (d) 1R100, (e) 1R200, (f) 1R300, (g) 1R350, (h) 1RL excited by 808 nm LD (1RL was prepared by preserving sample 1R at room temperature in air for 2.5 months). The inset shows the relative NIR luminescence intensity as a function of x for γ -ray irradiated $(Y_{1-x}Bi_x)_4GeO_8$ ($x = 0.0025, 0.005, 0.0075, 0.01, 0.02, 0.03$) crystals excited by 808 nm LD. (c) ESR spectra of γ -ray unirradiated, irradiated and heat treated samples: 0A, OR, OR350, 1A, 1R, 1R100 and 1R350. Reproduced from Ref. [235]. Copyright © 2011, The Electrochemical Society.

a part of free electrons generated by the γ -ray irradiation may be captured by Bi^{3+} to form Bi^{5+} and Bi^+ , respectively, which agrees with the valence state change of transition metal ions in glasses irradiated by femtosecond laser. As the thermal treatment temperature increases, the holes and free electrons were released and recombined with each other, leading to the decrease of the signal intensity of g_2 and the concentration of Bi^{5+} and Bi^+ , which is in consistent with the decrease of NIR emission intensity of γ -ray irradiated Bi-doped samples shown in Fig. 41b. In 1R350, only the signal at g_2 remains, a part of electron trapping centers still exist stably in the γ -ray irradiated Bi-doped samples.

5.4. Molecular crystals containing Bi polyhedra

Molecular crystals containing Bi polyhedra can be divided into two groups based on the charges Bi units possess, i.e., crystals containing Bi polycations [11–24,31–35] and polyanions [26–30]. In contrast to the rapid progress of synthetic approaches of molecular crystals containing Bi, their optical properties, especially the PL property, has not attracted significant attention in the research community.

In 2011, Sun et al. first reported that $Bi_5(AlCl_4)_3$ crystal exhibits extremely broad NIR PL with a FWHM of >510 nm and an effective PL lifetime of $4.1\ \mu s$ at 1160 nm [33]. One advantage of this material system is that its structure is simple, and can be well characterized by widely used techniques such as XRD and Raman spectroscopy. As shown in Fig. 42a, all the XRD patterns can be indexed as the rhombohedral structure in agreement with the standard diffraction pattern (CSD No: 420082).

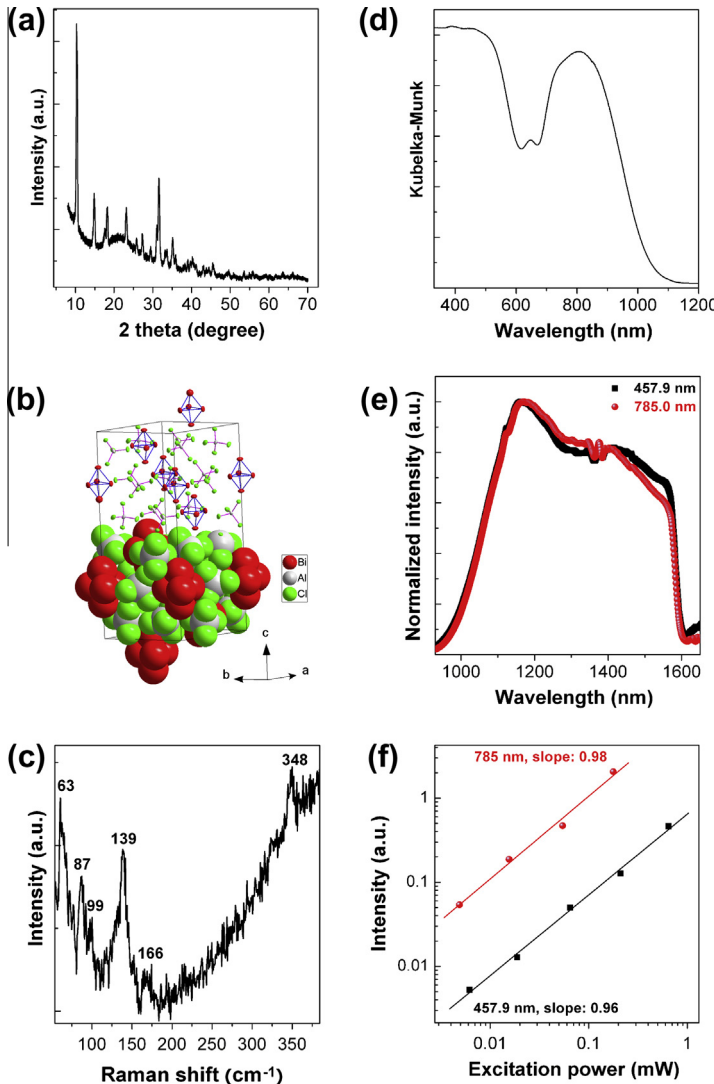


Fig. 42. (a) XRD spectrum of $\text{Bi}_5(\text{AlCl}_4)_3$ crystal. (b) View of space-filling and ellipsoid with 50% probability of $\text{Bi}_5(\text{AlCl}_4)_3$ crystal. (c) Raman spectrum of $\text{Bi}_5(\text{AlCl}_4)_3$. (d) UV-vis-NIR diffuse reflectance spectrum of $\text{Bi}_5(\text{AlCl}_4)_3$ crystal. (e) PL spectrum of $\text{Bi}_5(\text{AlCl}_4)_3$ crystal under the excitation of 457.9 and 785.0 nm. Note that the long-wavelength (>1600 nm) signal is suppressed owing to the drop of InGaAs sensitivity. (f) Log-log dependence of the NIR emission intensity on excitation power under the excitation of 457.9 and 785 nm. Reproduced with permission from Ref. [33].

The $\text{Bi}_5(\text{AlCl}_4)_3$ crystal is built from Bi_5^{3+} trigonal bipyramids and $[\text{AlCl}_4]^-$ tetrahedra (Fig. 42b). As shown in Fig. 42c, the scattering bands at 63 , 87 , 99 , and 139 cm^{-1} can be assigned to the $v_4(\text{E}')$, $v_6(\text{E}')$, $v_2(\text{A}_1')$, and $v_1(\text{A}_1')$ vibrational modes of Bi_5^{3+} polycations, while the bands at 166 and 348 cm^{-1} to AlCl_4 anions. It is found that $\text{Bi}_5(\text{AlCl}_4)_3$ crystal demonstrates a broad NIR absorption band peaked at 807 nm , a weak band at 648 nm , and a UV-vis shoulder ranging from 330 to 620 nm (Fig. 42d). Under the excitation of 457.9 and 785.0 nm , the emissions of $\text{Bi}_5(\text{AlCl}_4)_3$ cover extremely broad NIR region with the FWHMs of $>510\text{ nm}$, and the PL lineshapes are nearly identical at both excitation wavelengths (Fig. 42e). The log-log dependence of the NIR emission intensity on excitation power suggests that one excitation photon is involved in the emission (Fig. 42f).

Although the assumption that Bi polycations may be optically active center can date back to earlier work carried out by Sun et al. [221,224], the direct observation of such broad absorption and emission bands in $\text{Bi}_5(\text{AlCl}_4)_3$ molecular crystal not only proves that such positively-charged Bi species indeed possess peculiar photophysical properties, but also stimulates more efforts to study the PL mechanisms in other systems. Although this work presents one simple route for the establishment of structure–property relationships of Bi species, there still remain scientific issues to be addressed, especially the asymmetric emission lineshapes. In a subsequent study, Sun and coworkers further studied the photophysical properties of $\text{Bi}_5(\text{GaCl}_4)_3$ sample synthesized through the oxidation of Bi metal by gallium chloride salt, based on the measurements of powder XRD, micro-Raman scattering and steady-state and time-resolved PL spectroscopy [35]. The thorough comparison of steady-state and time-resolved PL behaviors between $\text{Bi}_5(\text{GaCl}_4)_3$ product and $\text{Bi}_5(\text{AlCl}_4)_3$ suggests that Bi_5^{3+} is the dominant emitter in the product, which gives rise to the ultrabroad emission ranging from 1 to 2.7 μm , with a peak at ca. 1.8 μm (Fig. 43). Although the emission spectrum of $\text{Bi}_5(\text{GaCl}_4)_3$ sample is very noisy, it is obvious that its lineshape is similar to that of $\text{Bi}_5(\text{AlCl}_4)_3$, suggesting that the slight difference of the structures of $\text{Bi}_5(\text{GaCl}_4)_3$ and $\text{Bi}_5(\text{AlCl}_4)_3$ crystals does not strongly influence the photophysical properties of Bi_5^{3+} units. Detailed quantum chemistry calculation makes it possible to assign the observed excitations to some electronic transitions of Bi_5^{3+} polycation, especially at shorter wavelengths [35]. Recent work carried out by Cao et al., in which they adopted a different approach for the synthesis of $\text{Bi}_5(\text{AlCl}_4)_3$ and then took emission spectrum by using a more sensitive infrared detector, further evidences that Bi_5^{3+} is a peculiar emitter [66]. In general, the broad PL signal was directly taken after the excitation of the powdered samples enclosed between two silica pieces. In view of such broad emissions, it is suggested that the PL had better be taken by using an integrating sphere to more accurately analyze the emission lineshape, which should be feasible if such molecular crystals are sealed in a pure fused silica cell. Furthermore, synthesis of high-quality crystals is also very important to analyze their photophysical properties, as evidenced by a series of work in this regard from different groups [33–35,66]; otherwise, defects in the crystals will strongly affect the emission lineshapes.

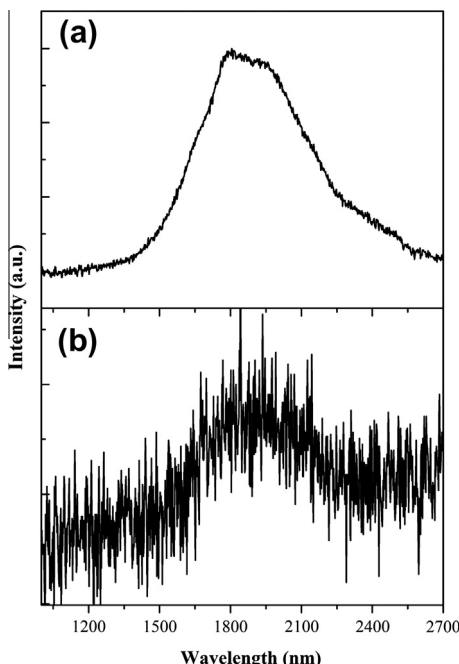


Fig. 43. PL spectra of $\text{Bi}_5(\text{AlCl}_4)_3$ (a) and $\text{Bi}_5(\text{GaCl}_4)_3$ (b) samples under 808 nm excitation. Reproduced with permission from Ref. [35].

Given that molecular crystals containing Bi have clear crystalline structures, very recently Sun et al. experimentally and theoretically studied the photophysical properties of Bi_8^{2+} polycation stabilized by $[\text{AlCl}_4]^-$ [34]. It was revealed that Bi_8^{2+} polycation results in the emission peaking at ca. 1180 nm. As displayed in Fig. 44, four peaks appear at the excitation/emission wavelengths of 290/1180, 490/1180, 636/1187, and 830/1192 nm, among which the intensity of the fourth peak is the strongest. Clearly, the PL peak does not display significant excitation-wavelength-dependent shift, which situate in the range of 1180–1200 nm under diverse excitation wavelengths. This work further evidences that Bi polycations can be smart emitters, whose emission can cover important telecommunication wavelengths.

All aforementioned Bi species were positively charged. It is noteworthy that many compounds with Bi polyanions absorb light in the visible range of the electromagnetic spectrum since they are colored, which gives promise for unique optical properties [67]. It is reasonable to anticipate that some of the polyanions may turn out to be novel optical emitters, perhaps in important spectral ranges such as biological and/or telecommunication optical windows, due to their inherent electronic transitions [69]. In 2012, Sun and coworkers first reported that a single crystal of $(\text{K-crypt})_2\text{Bi}_2$ which contains $[\text{Bi}_2]^{2-}$ polyanions displays ultrabroad NIR emission at around 1190 nm. The high-quality single crystal was characterized by single-crystal XRD, diffuse reflectance spectroscopy, and PL measurements [69]. The UV-vis-NIR diffuse reflectance spectrum demonstrates peculiar absorption bands at 471, 593, 705, 990, 1090, and 1273 nm (Fig. 45a). It is obvious that the absorption in the NIR region is much weaker than that in the visible range, suggesting that the electronic transition probabilities in the NIR and visible ranges are different. As demonstrated in Fig. 45b, the emission spectrum under 641 nm excitation has a very broad emission range, spanning from 975 to 1400 nm. The FWHM of the spectrum is 212 nm and the emission peak is at around 1190 nm. The emission spectrum by Gaussian decomposition results in three decomposed curves peaking at 1047, 1190 and 1331 nm with FWHMs of 99, 146, and 56 nm, respectively (Fig. 45b), whose emission energies are lower than the corresponding absorption energies at 990, 1090, and 1273 nm, respectively. The result of log-log dependence of the NIR emission intensity at peak wavelength as a function of the excitation power evidences that the emission is a single-photon process (Fig. 45c). Since at present the theoretical results are only approximate and do not completely agree with the experimental facts, a qualitative explanation of the observed photophysical behavior is proposed (Fig. 45d) [69]. The $[\text{Bi}_2]^{2-}$ anion absorbs photons with energies in the NIR and visible ranges. After irradiation with high-energy photons, the electrons in the upper excited levels tend to nonradiatively relax to the first three excited levels from where the NIR emissions take place. That is, NIR PL results from the radiative electronic transitions from the first

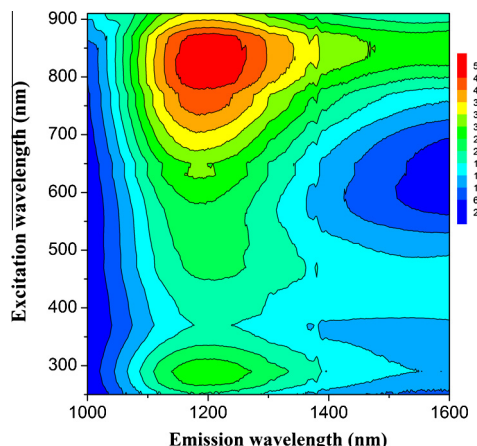


Fig. 44. Contour excitation–emission matrix plot of the obtained $\text{Bi}_8(\text{AlCl}_4)_2$ sample. Note that the jump at around 1400 nm results from measurement artefacts. Reproduced with permission from Ref. [34].

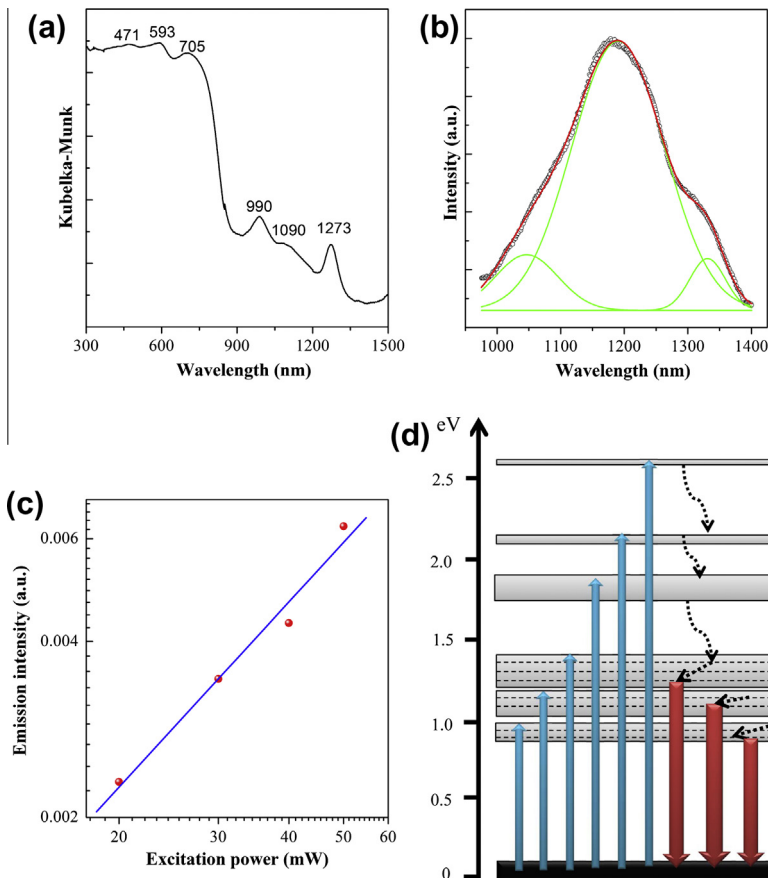


Fig. 45. (a) The UV-vis-NIR diffuse reflectance spectrum of crystalline (K-crypt)₂Bi₂. (b) The PL spectrum of (K-crypt)₂Bi₂ crystals under 641 nm excitation light. The black, red and green curves are experimental, fitted, and three decomposed Gaussian peaks, respectively. (c) Log-log dependence of the emission intensity at the peak wavelength on the excitation power of the 641 nm diode laser. (d) Simplified energy-level diagram of the [Bi₂]²⁻ emitter. The blue and red arrows represent the excitation and emission bands, respectively. The black dotted arrows label the nonradiative relaxations. The dotted horizontal lines represent the vibrational sublevels corresponding to the lowest three excited levels. Reproduced with permission from Ref. [69].

three excited levels to the ground level based on a one-photon process. The overlap of the three emission bands leads to the observed ultrabroad PL band ranging from 975 to 1400 nm. This result [69], in combination with earlier reports on PL in positively-charged Bi units [33–35,66], greatly deepens the understanding of Bi-related NIR emission behavior and leads to the reconsideration of the fundamentally important issue on Bi-related PL mechanisms in some material systems such as bulk glasses, fibers, and conventional optical crystals.

5.5. NIR PL origin: challenges and chances

Up until now, diverse material systems with peculiar NIR emission characteristics have been reported, ranging from glasses [88], conventional crystals [37,214–219,221–225,227–235], ionic liquids [61], and molecular crystals [33–35,66,69]. As shown in above sections, Bi has electron configuration of 6s²6p³, and it can exist as Bi⁰, Bi⁺, Bi²⁺, Bi³⁺ and Bi⁵⁺ valence state, and various cluster states e.g. Bi₅⁺, Bi₂²⁺, Bi₂²⁻ in crystals. This directly results in complicated electronic structures for Bi species. To convincingly explain the observed photophysical behaviors, one of the most critical issues is to establish

structure–property relationship. To realize this, one must pay particular attention to the analysis of structural features of studied systems. According to this criterion, NIR PL mechanisms in only a few systems are clear, including Bi_5^{3+} , Bi_8^{2+} , and Bi_2^{2-} polyhedra in molecular crystals [33–35,66,69] and Bi^+ substructures in zeolites Y [37]. It is necessary to note that NIR luminescence in Bi-doped glasses was first observed by Fujimoto et al. in 1999 [142]. They reported NIR emission at 1132 nm with a FWHM of 150 nm and fluorescent lifetime of 650 μs from Bi-doped silica glass with a small amount of Al_2O_3 , and the authors tentatively assigned the emission to Bi^{5+} [88]. Subsequently, a research group led by Qiu systematically investigated a broad range of multicomponent glasses activated by Bi [90–95], and they proposed some reasonable explanations of the observed NIR emission behaviors (that is, the observed PL in glasses might result from low-valence Bi), although more detailed work is required to support the assignment. After that, more results on the observation of NIR PL in various glasses have been reported by other groups [62,110,119,146,159,202,237]. Interestingly, broad NIR emissions have also been observed in a wide array of crystals, including halide, porous and oxide crystals. To explain the observed phenomena in glasses and most crystals, until now, several hypotheses concerning the origin of the NIR emission in Bi-doped glasses and some crystals were proposed, e.g., the formation Bi with low valence state and related clusters or Bi with high-valence state. However, several important challenges and questions on the proposed mechanisms remain, despite the extensive amount of research on this topic [35]. An important practical question is whether Bi with an identical oxidation state (i.e., the same type of Bi active center) contributes to the NIR emission in these materials. For most materials containing Bi, it is still a hard task to finally determine the detailed information of Bi, and it is rather unconvincing if we simply assign the NIR PL in different systems to the same type of Bi active center, considering the large difference of steady-state and time-resolved PL and of absorption spectra [35]. A second practical issue is that multi-type rather than single-type Bi active center may exist in some materials [61]. Many experimental results have clearly shown that Bi exists as multiple valence states in glasses, while only a small amount of active Bi species with special valence or clustering states which may not be easily detected by conventional techniques contributes to the NIR emission. Thus, it is reasonable to expect that multiple active centers may have chances to co-exist in some materials. A final unresolved critical issue involves the unknown local coordination environments of Bi in most materials. This is a principle obstacle to the understanding of Bi-related NIR emission behaviors, since most researchers merely reported the PL-related results and did not show definitely convincing results related to structural analysis [35]. To summarize, one key point should be recognized by researchers in this context: one should experimentally and theoretically investigate the photophysical properties of studied materials in combination with detailed structural analyses of Bi in the matrices, because there is not a model for the elucidation of NIR PL mechanisms in all systems and different emitters might possess similar emission ranges, as clearly evidenced by some previous work [33–35,37,66,69]. The physiochemical complexity of Bi makes it rather challenging to explain the experimentally observed phenomena, but presents abundant chances for future work. In the near future, further investigations on the origin of the NIR emission should be concentrated on, but not be limited to, the following five parts.

(1) Systematic investigations of NIR luminescent molecular crystals

As is well known, this class of materials has clear crystal structures, that is, the local coordination environments of Bi are well defined using single or powder XRD and Raman scattering techniques, which result in a convincing interpretation of PL behaviors, if they possess electronic transitions in the infrared [33–35,37,66,69]. This presents one of the simplest approaches to establish the structure–emitter–property relationship, which is helpful to deepen the understanding of Bi-related photophysical behaviors. However, researchers should pay attention to the synthesis of such crystals, i.e., selection of suitable synthesis routes for obtaining high-quality crystals. It is worth to note that high-sensitivity detection systems are generally required to record the PL spectrum because some molecular crystals only demonstrate very weak infrared emissions.

(2) Systematic investigations of host-emitter relationship in glasses

There have been extensive investigations on the composition and melting condition dependent NIR luminescence in Bi-doped glasses, which have given some indirect conclusions. However, to reach the final conclusion about the origin of the NIR emission, we should exactly determine the glass compositions which may be changed during the melting process, and sum up the experimental data based on

theoretical instruction of optical basicity and thermodynamics. This detailed experimental work not only ensures the reproducibility, but also is rather helpful for following identification of emitters in studied systems.

(3) Design some peculiar Bi doped crystalline systems and investigate their photophysical behaviors

Since some active Bi species have peculiar ionic radii, e.g., Bi^+ in zeolite Y has a radius of 1.465 Å [37], we can use such kind of clues to direct the selection of hosts. In recent reports, Romanov and coworkers systematically examined the photophysical properties in Bi-doped KAlCl_4 and KMgCl_3 crystals [219,220], and detailed experimental results suggest that the luminescence peaking near 1 μm belongs solely to Bi^+ ion which substitutes potassium in the crystal [219]. This result is important, based on the following considerations. The lineshape of PLE spectra at emission peaks in these systems is rather similar to experimentally determined absorption spectra of Bi^+ in molten salts previously reported [8,9]. Note that the assignment of Bi^+ -related absorption bands by Bjerrum et al. was based on careful experimental design and strict deduction from spectroscopic results [8,9]. Basically, it is a convincing and reasonable explanation of the observed phenomena, although the exact local environments of Bi have not been determined [8,9]. In view of this, the work from Romanov and coworkers helps the researchers in this regard to gain some insightful views on NIR emission mechanisms in other materials and will stimulate more concentrated efforts in this direction. By using this approach, that is, consideration of the structural features of both Bi species and crystals, it is reasonable to believe that more interesting and applicable crystalline materials will be developed in the future, and the accumulated knowledge will greatly deepen the understanding of physiochemical properties of this wonder metal.

(4) Direct and quantitative measurements of various species of Bi and their local structure in glasses and conventional crystals

Absorption, luminescence and Raman spectra may give some structural information about Bi related energy level and local structure, but cannot give direct evidences about the valences state of Bi and neighboring structures. EXAFS and XPS are powerful techniques for examining the valence state of Bi and local structure around Bi, but X-ray may induce structural change as X-ray induced valence state change has been reported in various ions doped materials, especially when multiple forms of doped ion co-exist. Careful determination of experimental conditions is necessary to get exact evidence. Time-resolved XAFS may be useful for clarifying existence of various valence state Bi species. In addition, quantitative analysis is necessary for determining the content of various species of Bi to establish an exact and precise model about the origin of the NIR emission from Bi-doped systems.

(5) Theoretical calculation and prediction based on state-of-the-art quantum-chemistry code

There have been some theoretical calculations about the energy levels and transition probabilities based on quantum-chemistry calculations [19,28,34,35,70,121]. In future work, more detailed and insightful investigation of theoretical electronic structures of some Bi species, coupled with experimentally determined Bi structures, will gain abundant meaningful perspectives on Bi-related NIR emission mechanisms.

With enough efforts in these directions, it is believed that a series of NIR emission mechanisms on Bi in various matrices will be elucidated convincingly in the near future.

6. Applications

6.1. Broadband NIR optical amplifiers

An optical amplifier is a device that amplifies an optical signal directly. In doped fiber amplifiers and bulk lasers, the stimulated emission in gain media causes amplification of incoming light. Optical amplifiers are the most essential element of modern optical fiber communication systems, continuously extending the reach of wavelength division multiplexing architectures.

Doped fiber amplifiers (DFAs) are optical amplifiers that use a doped optical fiber as a gain medium to amplify an optical signal. The signal to be amplified and a pump laser are multiplexed into the doped fiber, and the signal is amplified through interaction with the doping ions. The most common example is the Erbium Doped Fiber Amplifier (EDFA), where the core of a silica fiber is doped with

trivalent Er ions and can be efficiently pumped with a laser at a wavelength of 980 nm or 1480 nm, and exhibits gain in 1550 nm. However, the importance of 1.3 μm for optical communication is that the natural zero dispersion region of silica glass fiber and temporal distortion of transferred optical pulses can be minimized at this wavelength [89].

Fujimoto et al. first pointed out that the broad emission at 1.25 μm with 0.8 μm excitation from bismuth-doped silica glass would be useful as a core material of an optical amplifier at zero-dispersion wavelength [89]. The experimental configuration is shown in Fig. 46. A 0.8-μm semiconductor laser and 1.3-μm semiconductor laser were used as excitation and probe sources, respectively. These two beams were collimated by lens. The probe beam was chopped at 200 Hz by a chopper and was overlapped on the excitation beam. The overlapped beams were focused onto a sample by using a lens with 100-mm focal length. The amplified probe beam was detected by a germanium semiconductor detector by eliminating the excitation beam with infrared transmission filters. The detected electric pulses were displayed by a digital oscilloscope.

An oscilloscope image of the amplification experiment is shown in Fig. 47. The chopped 1.3-μm probe beam without excitation is curve (a), the beam with excitation is curve (b). Excitation power of 2.0 W was focused onto the sample and the focal spot was about 0.5 mm in diameter. The optical gain is calculated at 1.19 and, therefore, the gain coefficient g is 0.663 cm^{-1} . It is clear that the probe beam increases with excitation. Both signals between 4 and 6 ms are zero and, therefore, neither spontaneous emission nor leakage of the excitation beam was detected. The optical gain linearly increased with increasing excitation power up to 2.0 W.

After this early work, optical amplification demonstrations based on glass media were mainly shown by Qiu's group, as listed in Table 2 [145,151,238–240]. For instance, Zhou et al. reported the optical amplification from Bi-doped germanium silicate glass (GAB: 96.5GeO₂–3Al₂O₃–0.5Bi₂O₃ and GSAB: 79.5GeO₂–17SiO₂–3Al₂O₃–0.5Bi₂O₃ (in mol%) [145]. The traditional two-wave mixing configuration was adopted for internal gain measurement (inset of Fig. 48). Fig. 48 shows the wavelength-dependent internal gain from 1272 to 1348 nm and the gain at 1560 nm is also measured. The excitation power is 1.12 W. It can be observed that the measured spectral dependence of the optical gain resembles the fluorescence spectrum. The highest gain at 1272 nm of GAB and GSAB samples reaches to 3.65 and 6.73 dB, respectively. The values are larger than the reported results in Bi-doped silica glass [89]. The efficient gain from 1272 to 1348 nm demonstrates that the GAB and GSAB glasses can be used as a broadband amplifier especially at the second telecommunications window since there is no appropriate amplifier except for Pr-doped fluoride fiber amplifier in this window. Furthermore, it is significant that optical amplification at 1560 nm is also observed. The single-pass gains at 1560 nm of GAB and GSAB samples are 0.95 and 2.3 dB, respectively. It is significant since there is no report of realizing optical amplification at O and C bands simultaneously when excited by a single pumping

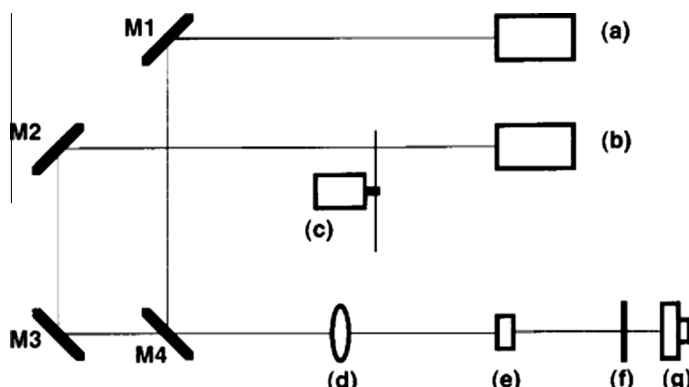


Fig. 46. An experimental configuration. (a) 0.8-μm semiconductor laser for excitation, (b) 1.3-μm semiconductor laser as a probe beam, (c) chopper, (d) lens with 100-mm focal length, (e) sample, (f) filters, and (g) germanium semiconductor detector. M1–M4 are mirrors. Reproduced from Ref. [89]. Copyright © 2003, American Institute of Physics.

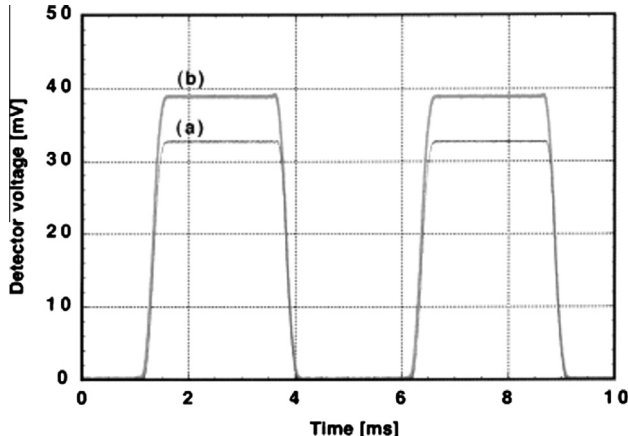


Fig. 47. An oscilloscope image of the amplification phenomenon. Reproduced from Ref. [89]. Copyright © 2003, American Institute of Physics.

Table 2
Optical amplification results in different bulk glasses.

Glass composition (mol%)	Laser source (nm)	Pumping power (W)	Emission wavelength (nm)	Max. gain	Max. gain coefficient (cm^{-1})	Refs.
1Bi ₂ O ₃ –7Al ₂ O ₃ –92SiO ₂	810	1	1307.5	1.16	0.62	[238]
1Bi ₂ O ₃ –7Al ₂ O ₃ –91SiO ₂ –Li ₂ O				1.08	0.32	
1Bi ₂ O ₃ –5Al ₂ O ₃ –20SrO–75GeO ₂	808	0.97	1315	1.23	1.03	[236]
96.5GeO ₂ –3Al ₂ O ₃ –0.5Bi ₂ O ₃	980	1.12	1272	3.65	–	[145]
79.5GeO ₂ –17SiO ₂ –3Al ₂ O ₃ –0.5Bi ₂ O ₃				6.73	–	
50SiO ₂ –30GeO ₂ –15MgO–5Al ₂ O ₃ –Bi ₂ O ₃	808	0.97	1300	1.7	–	[151]
	980	3		1.82	–	
82P ₂ O ₅ –17Al ₂ O ₃ –1Bi ₂ O ₃ –3.5Yb ₂ O ₃	980	1	1272	–	2.62	[240]

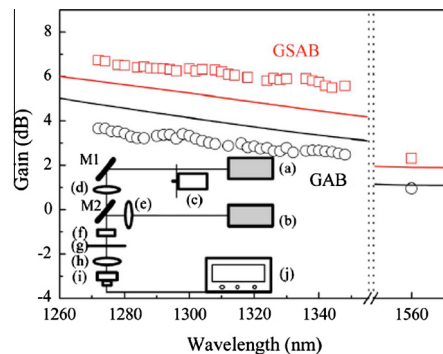


Fig. 48. Wavelength-dependent internal gain from 1272 to 1348 nm under the excitation power of 1.12 W. The gain at 1560 nm is also measured. The inset shows the schematic diagram. (a) 1300 nm tunable LD and 1560 nm LD as seed beam, (b) 980 nm LD as excitation resource (the dimension of the beam waist is $68.2 \times 61.6 \mu\text{m}^2$), (c) chopper, (d) lens with 100 mm focal length, (e) lens with 50 mm focal length, (f) sample, (g) filter, (h) lens with 25 mm focal length, (i) InGaAs p-i-n detector, and (j) digital oscilloscope. M1 and M2 are mirrors. Reproduced from Ref. [145]. Copyright © 2007, American Institute of Physics.

source in Bi-doped materials. According to the broadband emission and wavelength-dependent gain properties of the samples, the acquired gain at O and C bands was just limited by the available seed source and broader gain covering the whole O, E, S, C, and L bands is expected. Such a broadband amplification characteristic is seldom observed in other kinds of gain materials.

Besides, on-off gains in the Bi-doped alumina-free phosphogermanosilicate fibers [186] and aluminosilicate fiber [190] have been demonstrated for the first time by Dianov's group. In the case of aluminosilicate fiber, the maximum net gain obtained in the piece of the fiber of 38 m length with approximately of 300 mW of launched pump power is presented in Fig. 49 [190]. The positive net gain was observed in the range 1430–1495 nm which is promising for development of Bi-doped fiber amplifiers operating in S and E telecommunication bands.

6.2. Fiber laser

Fiber lasers are part of the family of solid state lasers. In the fiber laser, the lasing medium is an optical fiber doped with low levels of a rare earth element, such as yttrium, erbium or thulium, which determine the wavelength of the output light. Diode lasers are used to couple infrared light into the cladding of the doped fiber and act as the pump source. This pumping action excites the dopant atoms, stimulating them to emit photons at a specific wavelength. Diffraction gratings are used as the rear mirror and output coupler, which form the resonator. Fiber lasers have excellent beam quality and the highest efficiency among solid-state lasers.

Fig. 50 shows the spectral regions of the existing efficient fiber lasers based of RE ions. It is seen that there is a spectral region of 1150–1500 nm where no fiber lasers (and any other efficient lasers) exist. But this spectral region is very promising for a number of important applications, such as advanced optical communication systems, medicine, and astrophysics. Fortunately, as discussed in Section 5.2.1, there are a number of Bi-doped glasses emit luminescence in an exceptionally wide region of 1100–1600 nm. These results showed a possibility for the development of fiber lasers in this spectral region.

6.2.1. New wavelength laser

The first Bi-doped fiber laser was demonstrated in 2005 using aluminosilicate glass fiber by Dianov et al. [71]. CW lasing was obtained at wavelengths 1146, 1215, 1250, and 1300 nm upon pumping at $\lambda_p = 1064$ nm. The cut-off wavelength of the active fiber was $\sim 1 \mu\text{m}$, the absorption coefficient at the pump wavelength in a fiber used was 55 dB. Pairs of Bragg gratings with the reflectivities of 3 and 20 dB for the above wavelengths were written in germano-silicate fibers with the cut-off wavelength at 1.1 μm . The two-mode character of propagation of radiation in these fibers resulted in partial optical losses in splices with the active fiber. The lasing parameters were measured at wavelengths

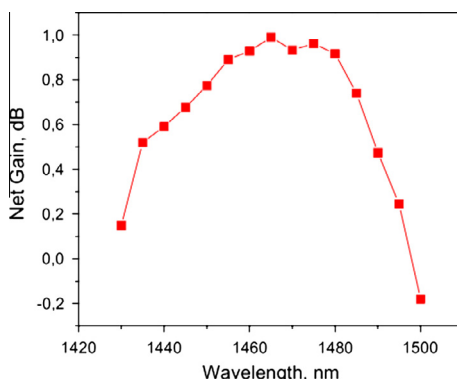


Fig. 49. Net gain for the Bi-doped fiber piece of 38 m length pumped at 1343 nm wavelength. Reproduced from Ref. [190]. Copyright © 2008 Optical Society of America.

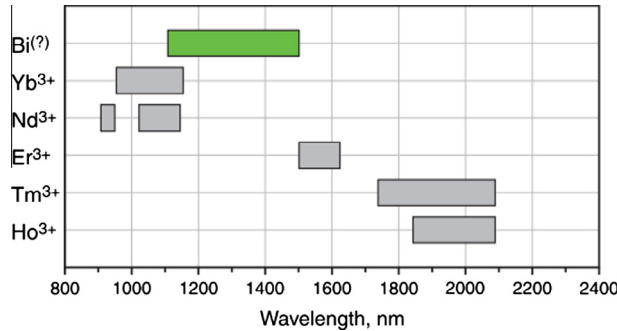


Fig. 50. Spectral regions of the existing efficient rare earth fiber lasers. The upper rectangle indicates the wavelength region that can be potentially covered by Bi fiber lasers. Reproduced from Ref. [183]. Copyright © 2009, WILEY-VCH Verlag GmbH & Co. KGaA, Weinheim.

1146 nm and 1215 nm. The maximum output power obtained upon pumping by ~5 W was 460 mW at 1146 nm and 400 mW at 1215 nm. The lasing threshold at 1146 nm was 420 mW, and the slope efficiency recalculated to the input power was 10.2%. The lasing threshold at 1215 nm was 890 mW and the slope efficiency was 14.3%.

Later on, new-wavelength fiber lasers based on Bi-doped fibers were developed gradually [183–186,188,241,242]. A review of these efforts for developing Bi-doped fiber lasers is presented in Ref. [183]. The development of Bi-doped fiber lasers were summarized in Fig. 51 [243]. The vertical axis shows the maximum output power of the continuous wave fiber lasers operating at corresponding wavelengths. The circles on the horizontal axis show the pumping wavelengths, with the color of the circles indicating the corresponding wavelengths generated. At present, Bi-doped fiber lasers operate in the spectral region of 1140–1550 nm. However, given the wider spectral region associated with Bi-doped glasses and fibers, new wavelength lasers is hopeful to be developed.

6.2.2. Tunable fiber laser

The broadband emission feature of Bi-doped fibers makes them probable for the fabrication of tunable fiber laser by using certain elements (such as grating) to change laser wavelength. In Ref. [185], fiber Bragg gratings (FBGs) were written directly in the alumina-free Bi-doped phosphogermanosilicate (PGSB) fibers, in order to reduce the intracavity optical loss. Lasing in the gain band of the PGSB fiber in three schemes of fiber lasers with different FBG resonance wavelengths and different pump

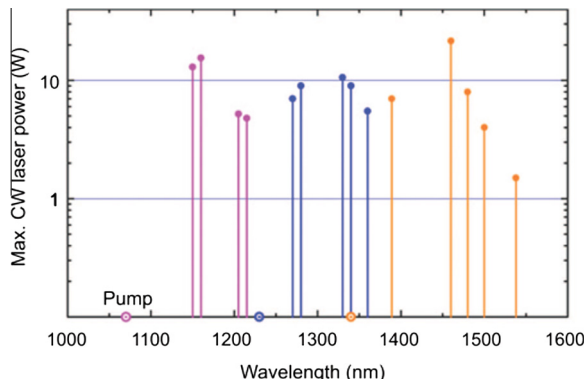


Fig. 51. The output power of various Bi-doped fiber lasers operating in the spectral region of 1150–1550 nm. CW, continuous wave. Reproduced from Ref. [243]. Copyright © 2012, Changchun Institute of Optics, Fine Mechanics and Physics.

wavelengths were obtained, as shown in Fig. 52 [185]. Laser 1 pumped at 1230 nm emitted at 1310 nm. The threshold pump power P_{th} was ~ 150 mW. The slope efficiency of the laser with respect to the absorbed pump power was $\sim 3.2\%$ at room temperature and pump power $P_p < 1$ W. Laser 2 pumped at 1230 nm emitted at 1345 nm. The slope efficiency of this laser was considerably lower, being 0.8% at $T = 300$ K. The pump threshold was ~ 200 mW and P_{max} was 30 mW at $P_p = 3.7$ W. Laser 3 was pumped at 1205 nm, while the cavity of laser 3 was tuned to a wavelength of 1310 nm. The slope efficiency of laser 3 was 1.4% at room temperature for $P_{\text{th}} \sim 200$ mW.

In the case of Bi-doped aluminosilicate fiber, laser action exhibits high sensitivity to the temperature [190]. The efficiency of the laser action when pumped at 1356 nm was about 0.15% with a threshold of 230 mW (Fig. 53). Cooling of the active fiber to -90 °C resulted in an insignificant change of the laser efficiency but the threshold became two times smaller, about 110 mW. The laser emission moved to the wavelength of 1445 nm and became narrower (Fig. 54). The difference in the peak position and the FWHM of laser line in these experiments can be associated with possible change of the gain shape and magnitude with the change of the pump wavelength and temperature.

6.2.3. Pulsed fiber laser

Two types of pulsed Bi-doped fiber lasers have been demonstrated by Dianov et al. – a mode-locked Bi-doped fiber laser [244] and a Q-switched Yb-Bi fiber laser [245].

6.2.3.1. A mode-locked Bi-doped fiber laser. The schematic of bismuth doped fiber laser is shown in Fig. 55 [183]. The laser cavity comprised 12 m of Bi-doped silicate glass fiber with absorption of ~ 1.2 dB/m at the pump wavelength of 1062 nm, a 1062/1165 pump coupler, and a fiber loop output mirror with $\sim 95\%$ reflectivity at the lasing wavelength. The laser was core-pumped with a 1 W Yb-doped single-mode fiber laser. The laser emitted nearly transform-limited 50 ps pulses with a width of 0.02 nm at 1161.6 nm, a pulse-repetition rate of 13 MHz and 2 mW average power. An optimized cavity design and alignment allows stable short-pulse operation with a repetition rate of 7.5 MHz. A typical pulse train observed with an oscilloscope is shown in Fig. 56. Autocorrelation trace in Fig. 57 reveals pulse duration of 0.94 ps.

6.2.3.2. A Q-switched Yb–Bi fiber laser. In Q-switched Yb–Bi fiber laser, the Yb fiber laser is Q-switched by use of a saturable absorber, a Bi-doped fiber placed in its own resonator, and pulsed lasing is obtained in both fiber lasers [245]. The Yb-doped fiber of 20 m length had a cutoff wavelength of 1.4 μm and a core-cladding refractive index difference of 0.009. The Bi-doped fiber had a cutoff at

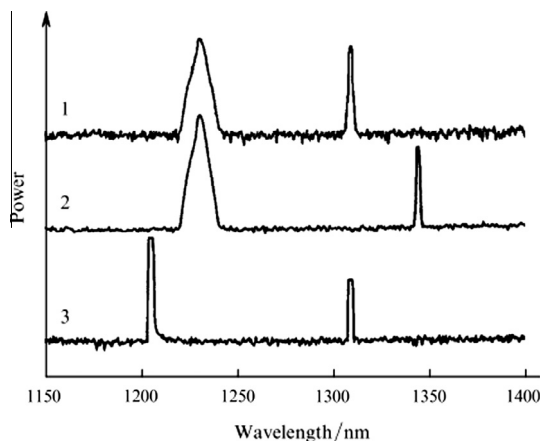


Fig. 52. Spectra of a Bi-doped fiber laser emitting at $\lambda_g = 1310$ nm and pumped at $\lambda_p = 1230$ nm (laser 1), $\lambda_g = 1345$ nm and $\lambda_p = 1230$ nm (laser 2), $\lambda_g = 1310$ nm and $\lambda_p = 1205$ nm (laser 3). Reproduced from Ref. [185]. Copyright © 2008, Kvantovaya Elektronika and Turpion Ltd.

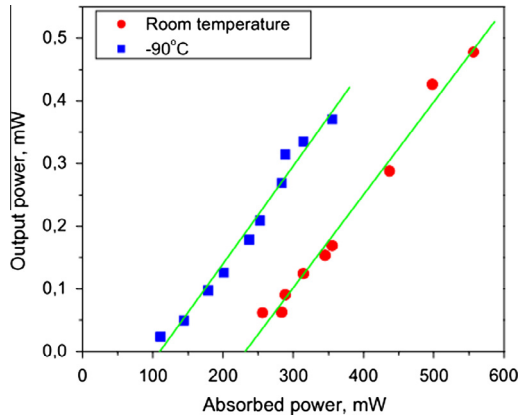


Fig. 53. Output power vs. absorbed pump power for the ring Bi-doped fiber laser pumped at 1356 nm wavelength. Reproduced from Ref. [190]. Copyright © 2008, Optical Society of America.

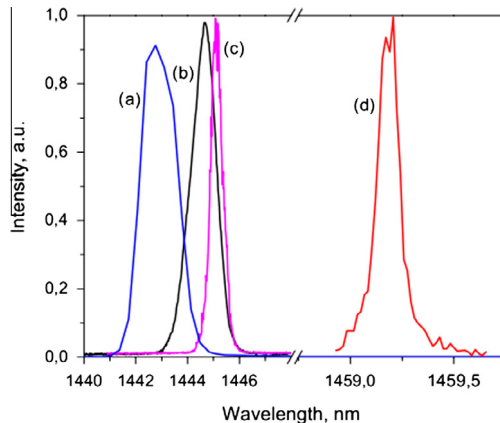


Fig. 54. Spectra of the laser emission: (a) 1343 nm pump wavelength, ring cavity, room temperature, (b) 1356 nm pump wavelength, ring cavity, room temperature, (c) 1356 nm pump wavelength, ring cavity, -90°C , (d) 1356 nm pump wavelength, linear cavity, -30°C . Reproduced from Ref. [190]. Copyright © 2008, Optical Society of America.

0.9 μm and a refractive index difference of 0.005. The laser cavities were made by fusion splicing the active fibers with fiber BGs. The BGs were written in germano-silicate fibers with parameters close to those of the active fibers. Cladding pumping of the Yb-doped fiber was performed by a diode laser operating at a 975 nm wavelength with a fiber output.

The performance of this fiber as a saturable absorber (SA) for the Yb fiber laser was first studied in a typical single-cavity scheme (one could get it from Fig. 58 by eliminating elements 2 and 3). The stable pulsed laser action was obtained at a 1050 nm wavelength with an efficiency of $\sim 10\%$ relative to the input pump power. The pulsed action occurred only near the threshold ($\sim 750 \text{ mW}$), and at the excess of $\sim 1.5 \text{ W}$ the laser action turned to a CW mode. It was not possible to obtain stable pulsed action at longer wavelengths (1064 and 1080 nm) owing to the laser's quick switching to the CW operation mode. But placing the Bi-doped fiber in the additional cavity (as shown in Fig. 58) led to a large spectral and pump power range expansion of the stable pulsed action and significant increases in the laser efficiency, pulse energy, and peak power of the Yb fiber laser. The laser action in the Bi-doped fiber was obtained at 1150 and 1215 nm wavelengths with 8 and 9 dB output coupler reflection, respectively. Stable pulsed action was obtained at the wavelengths of 1050, 1064, 1066, 1070, and

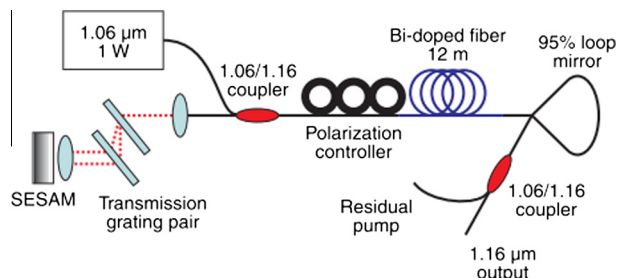


Fig. 55. Cavity setup of the mode-locked Bi-doped fiber laser. Reproduced from Ref. [183]. Copyright © 2009, WILEY-VCH Verlag GmbH & Co. KGaA, Weinheim.

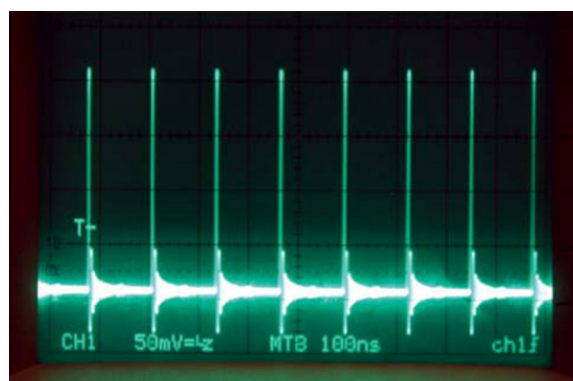


Fig. 56. Oscilloscope picture of the stable pulse train. Reproduced from Ref. [183]. Copyright © 2009, WILEY-VCH Verlag GmbH & Co. KGaA, Weinheim.

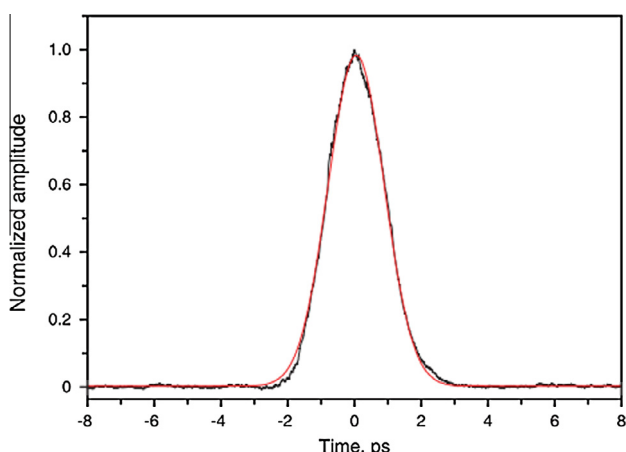


Fig. 57. Autocorrelation trace of Bi-doped fiber pulses. Reproduced from Ref. [183]. Copyright © 2009, WILEY-VCH Verlag GmbH & Co. KGaA, Weinheim.

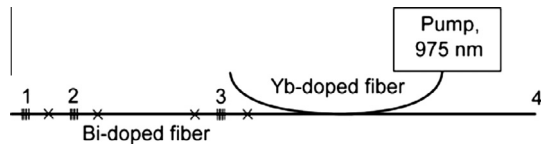


Fig. 58. Scheme of Yb–Bi fiber laser. 1, high-reflective coupler of Yb-doped fiber cavity; 2, output coupler of Bi-doped fiber cavity; 3, high-reflective coupler of Bi-doped fiber cavity; 4, output coupler of Yb-doped fiber cavity (cleaved fiber end). The single-cavity scheme did not contain elements 2 and 3. Reproduced from Ref. [245]. Copyright © 2007, Optical Society of America.

Table 3

Parameters of Yb–Bi Fiber Lasers. Reproduced from Ref. [245]. Copyright © 2007, Optical Society of America.

	Wavelength (nm)					
	1050 ^a	1050	1064	1066	1070	1080
Pulse energy (μJ)	3	17	65	100	90	75
Pulse width (μs)	3	~1	1.5	1	1.2	3.7
Peak power (W)	1	15	40	65	55	18
Bi-doped fiber length (m)	20	20	20	35	35	20

^a Single-cavity scheme.

1080 nm; see Table 3. The laser efficiency in the pulsed operation mode was about 50% relative to the input pump power and about 80% of the CW mode efficiency in the absence of the SA. For example, the pulsed laser efficiency was about 47% for 59% efficiency in the CW mode when lasing at 1070 nm. A typical pulse train is shown in Fig. 59.

6.3. Bioimaging

Bismuth has long been associated with medicine [43]. The recommended oral dosage for the different bismuth salts is 100–450 mg 3–4 times a day for several days/weeks [246]. However, little attention has been paid on the application of bismuth doped photonic materials for bioimaging. In 2011, Sun et al. demonstrated that the combined advantages of Bi and aluminosilicates lead to the finding of a new type of nanosized biolabel, i.e., NIR emitting silica coated bismuth doped aluminosilicate nanoparticles, which is simple to prepare, and exhibit highly efficient fluorescence covering the second biological window, high photostability, low cytotoxicity, and easy penetration into living tissues [72]. The SiO_2 coating results in a higher surface potential (-51.07 mV) of nanoparticles in comparison to -42.64 mV of uncoated ones, which suggests that it is helpful to enhance the dispersibility of

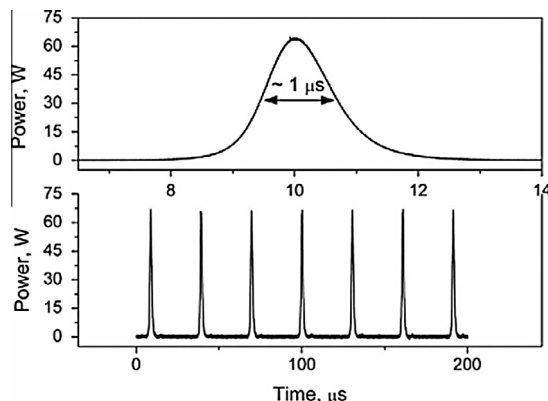


Fig. 59. Pulse train of Yb–Bi laser lasing at 1066 nm. Reproduced from Ref. [245]. Copyright © 2007, Optical Society of America.

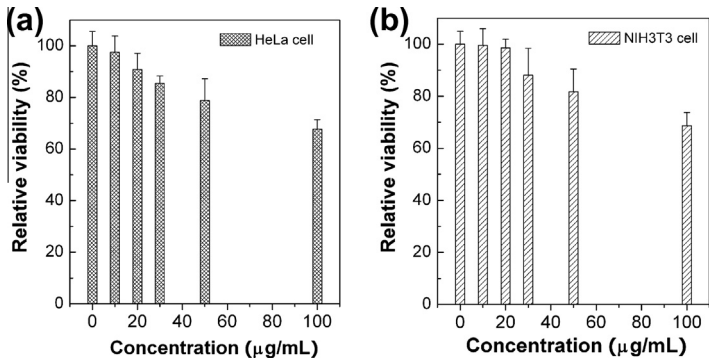


Fig. 60. Viability of (a) HeLa and (b) NIH3T3 cells after 24 h exposure to increasing doses of silica-coated nanoparticles, as evaluated with MTT assay. Values are mean standard deviation from four independent experiments. Reproduced with permission from Ref. [72].

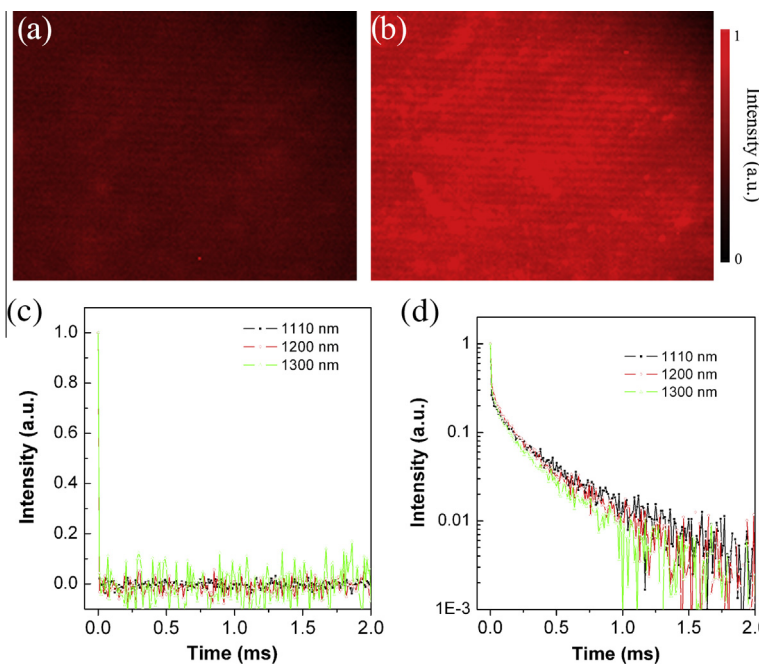


Fig. 61. *In vivo* NIR PL imaging of a mouse: (a) before and (b) after nanoparticles injection. Intensities are coded in false color, with red as the highest value. One mouse was injected subcutaneously in the neck region of a mouse with 100 μL solution. A microscope, equipped with NIR extended digital camera (Hamamatsu, Digital camera ORCA-R²), was used for NIR fluorescence imaging. A 690 nm LD was externally mounted to provide epi-illumination of the mouse. PL decay curves at 1110, 1200 and 1300 nm (c) before and (d) after nanoparticles injection. One mouse was injected subcutaneously in the neck region of a mouse with 50 μL solution, and 650 nm light (5 ns width, 20 Hz) was focused on the injection position. The excitation power is around 0.3 mW. Reproduced with permission from Ref. [72].

nanoparticles in assay buffers. *In vitro* cytotoxicity effects of the core–shell NPs on HeLa and NIH3T3 cells after 24 h exposure to increasing doses of nanoparticles was evaluated with MTT assay. It can be seen that the NPs do not show notable adverse effects on HeLa and NIH3T3 cell viability in concentrations to 10 and 20 $\mu\text{g}/\text{mL}$, respectively (Fig. 60). Even at a higher dose of 100 $\mu\text{g}/\text{mL}$, 60% cell viabilities can be maintained.

To further explore the potential of these NPs for deep tissue imaging, *in vivo* NIR PL imaging in mice is performed [72]. The false-color coded image in Fig. 61a shows that mouse tissue shows weak auto-fluorescence. NIR PL image was taken 30 min following hypodermical injection (Fig. 61b). The NIR signal assigned to the emission of Bi active centers, is extremely strong in the NIR region beyond 1 μm relative to the autofluorescence. This result clearly indicates that these NPs have great potential for deep tissue imaging. Owing to the long-lived emission characteristics, the possibility of PL lifetime imaging using these nanoparticles was further investigated. One mouse was injected hypodermically near the neck area of the body with 50 μL solution. The 650 nm light, with a power of ~ 0.3 mW, from an optical parametric oscillator pumped by the third harmonic of a Nd:YAG laser, was focused on the injection position. Fig. 61c and d displays the PL decays monitored at 1110, 1200 and 1300 nm before and after nanoparticles injection, respectively. The animal tissues show a rather short lifetime ($<1 \mu\text{s}$) (Fig. 61c). In contrast, the *in vivo* PL decay transients were found to be nonexponential at all emission wavelengths (Fig. 61d), consisting of a fast and slow components, which are attributed to the contributions of the tissue autofluorescence and of the nanoparticles, respectively. These initial data provide strong evidence that these nanoparticles are sufficient for *in vivo* lifetime imaging in the wide NIR region, suggesting that this nanocomposite might be a promising alternative to existing NIR luminescent nanomaterials.

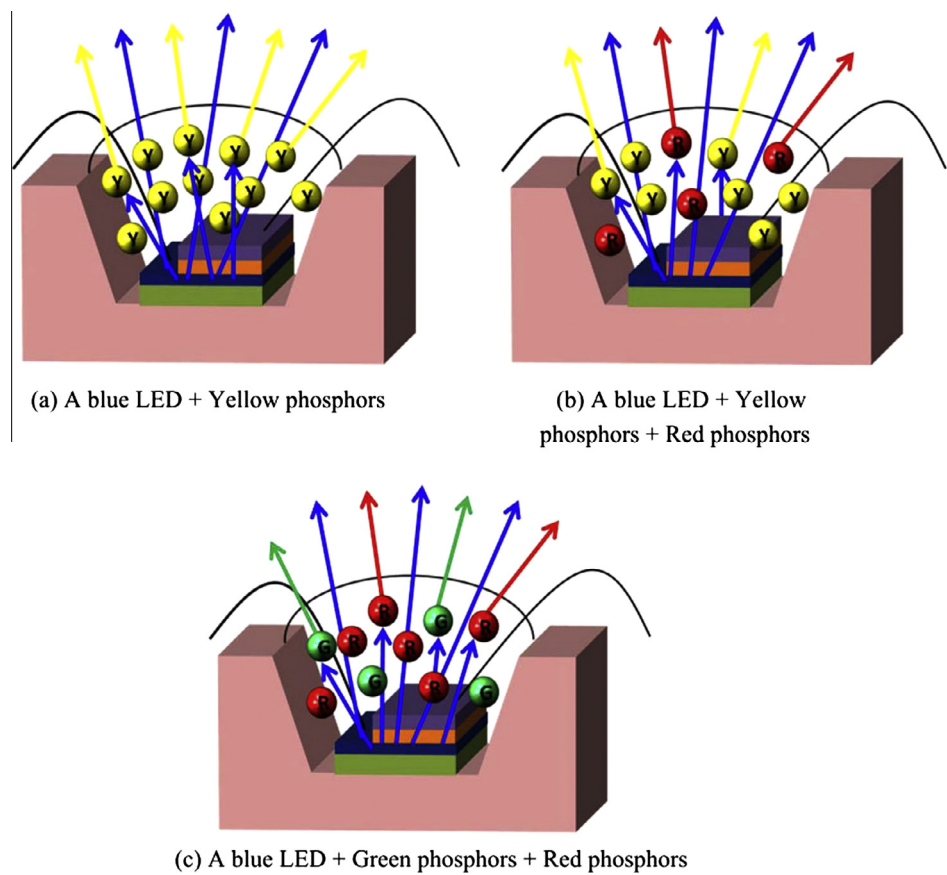


Fig. 62. Different ways of generating white light with blue LED and phosphors. Reproduced from Ref. [247]. Copyright © 2010, MDPI Publishing (Basel, Switzerland).

6.4. Phosphors for LEDs

Energy-efficient solid-state lighting and high-power white LEDs have been subjects of significant research efforts over the past decade. From the view point of industrialization, most commercially available white LEDs are prepared by pre-coating phosphors onto blue diode chips, because the luminous efficiency of blue chip based white LEDs is far higher than that of near-UV/UV type. According to the phosphors adopted in LEDs, the methods of generating white light can be summarized in three different types, as shown in Fig. 62 [247]. Thereby, special interest is given to materials that broadly emit in the yellow-to-red spectral range. Presently, the phosphors that can be adopted for commercial white LEDs are mainly rare-earth ions used. However, aside efficiency and total output power, color quality (the warm perception of incandescent light) remains a major challenge. For example, the biggest drawback of the well-known YAG:Ce³⁺-based dichromatic systems is their poor color rendering index (CRI). A warmer color perception can only be generated if an additional phosphor that emits at longer wavelengths like orange or red is included. Alternatively, Bi²⁺-doped materials have recently been proposed to be used as a novel white LED (WLED) phosphors [56,57,137,138]. Bi²⁺ represents the intermediate species of Bi, which typically absorb in the UV-visible region, and emit in the orange or red region with a lifetime of ~10 μs [57]. The optical property of Bi²⁺ suggests that Bi²⁺-doped phosphors may find the application in white LEDs.

Many kinds of oxide phosphors suitable for stabilizing Bi²⁺ to generate orange or red luminescence have been studied [53–57,137,138]. Here the typical optical properties of Bi²⁺ in SrB₄O₇ and SrB₆O₁₀ reported by Peng et al. are introduced [137]. In Fig. 63, the energy level diagrams (Fig. 63a) and corresponding optical excitation and emission spectra of both compounds (Fig. 63b) are illustrated. The derived spectra can readily be assigned according to above arguments: in SrB₄O₇:Bi, three excitation peaks and one emission peak are observed at 245, 478, 578, and 588 nm, corresponding to the transitions ²P_{1/2} → ²S_{1/2}, ²P_{1/2} → ²P_{3/2}(2), ²P_{1/2} → ²P_{3/2}(1), and ²P_{3/2}(1) → ²P_{1/2}, respectively. Similar results are observed in Bi²⁺-doped SrB₆O₁₀ with excitation peaks at 286, 380, and 560 nm and emission at 660 nm. The external quantum efficiency of 46% for SrB₄O₇:Bi²⁺ at excitation wavelength of 245 nm, and 88% for SrB₆O₁₀:Bi²⁺ at 286 nm is estimated from the excitation/emission data.

The spectroscopic properties of SrB₄O₇:Bi²⁺ and SrB₆O₁₀:Bi²⁺ suggest their potential application for improving CRI of WLED. Because of significant absorption at ~478 nm, SrB₄O₇:Bi²⁺ can be used to directly convert blue light to orange ones. Substitution of Sr²⁺ with other alkaline earth species, particularly Ca²⁺ in concentrations of up to 10 mol%, can be performed to further improve excitation

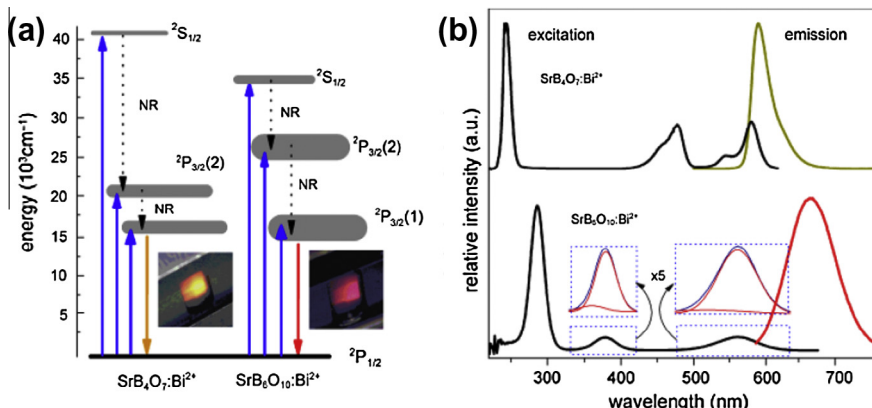


Fig. 63. Simplified energy level diagrams of SrB₄O₇:Bi²⁺ and SrB₆O₁₀:Bi²⁺, respectively and photographs of these samples luminescing in the sample holder (a; NR: nonradiative relaxation process) and corresponding excitation and emission spectra (b). Excitation spectra are given by monitoring emission wavelengths of 630 nm (SrB₄O₇:Bi²⁺) and 690 nm (SrB₆O₁₀:Bi²⁺); emission is plotted for excitation with 245 and 380 nm, respectively. Inset: zoom at the deconvoluted excitation to ²P_{3/2} in SrB₆O₁₀:Bi²⁺. Reproduced from Ref. [137]. Copyright © 2010, The American Ceramic Society.

efficiency in this spectral range. While $\text{SrB}_6\text{O}_{10}:\text{Bi}^{2+}$ cannot be excited in the blue, yellow light such as emitted by YAG:Ce³⁺ phosphors can be partly converted to red (660 nm), providing a warmer color perception and improved CRI. On the other hand, due to absorption in the soft UV (~ 380 nm), combination $\text{SrB}_6\text{O}_{10}:\text{Bi}^{2+}$ phosphor with a UV-emitting LED represents another potential application.

7. Conclusions and outlook

As traditional optical materials and devices are approaching the physical limits, there remains a constant push to develop novel material systems with new functionalities. In this regard, materials activated by heavier p-block elements become a rising star because of their fundamentally different electronic properties from the lighter congeners. In particular, Bi, the wonder metal, has been gradually recognized as one of the most important elements that can form a wide array of optically active centers, with emission spectral domain from UV, visible to NIR. This article has provided a comprehensive review on the synthesis, characterization, and functional applications of a broad range of Bi-activated photonic materials, with a particular emphasis on materials and devices possessing peculiar NIR emission behaviors. Obviously, great progress has been made in recent years for the synthesis of novel materials activated by Bi active centers including Bi^+ , Bi^{2+} , Bi^{3+} , Bi_5^{3+} , Bi_8^{2+} , and Bi_2^{2-} , to name just a few, owing to the continuous efforts from many research groups. Concurrently, novel fabrication approaches have been successfully developed in order to create the desired Bi species not only for solving fundamentally important issues such as PL mechanisms, but also for practical applications such as developing new-wavelength fiber lasers and high-efficiency phosphors. Furthermore, although many kinds of analytical methods are already available for the evaluation of the physicochemical and photophysical properties of Bi, some intriguing techniques, especially ^{209}Bi NMR and quantum chemistry calculations using state-of-the-art codes, have been emerged as new powerful tools for gaining revolutionary perspectives of Bi in some materials. The abundant accumulation of knowledge in this exciting field of sciences directly results in wide applications of Bi activated materials as well as devices in the domains of optical amplifiers, fiber lasers, bioimaging and phosphors.

The intensity of research interest in this field is still increasing [248,249], as evidenced by a count of the number of papers published in a given year. However, in this domain it is noteworthy that there still remain lots of scientific problems required to be addressed. Firstly, the main advantage of Bi lies in the multiple electronic structures of different Bi species, which results in emissions in a broad spectral range. Although it is recognized that hosts used strongly influence the oxidation states of Bi, that is, the local environments of Bi dominate its photophysical properties, unfortunately in many cases there is not a clear and convincing elucidation of the host-emitter relationship. Therefore, an evident trend is that research gradually shifts to the establishment of host-emitter relationships. To successfully realize this, one must pay more attention to structural analyses of studied systems by employing some advanced characterization techniques. This will lead to a better understanding of how to obtain materials with improved and desired optical properties or of how to reduce luminescence quenching caused by clustering of Bi ions. Secondly, compared with experimental works reported, theoretical works on the elucidation of photophysical behaviors of Bi species are rather insufficient. Although in recent years ab initio and DFT approaches have been used to calculate electronic structures of some Bi units, there still remains large difference between experimental and theoretical results. Thus, it is believed that more detailed work in this direction can help establish convincing structure-emitter-property relationships, resulting in clearer pictures on PL mechanisms of Bi species. Thirdly, Bi activated NIR emitting nanoparticles and films have great potential for *in vivo* bioimaging and integrated photonics, respectively. However, to reach these purposes, researchers in this community must develop more revolutionary approaches to fabricate them; for *in vivo* bioimaging, the method for the preparation of well-dispersed nanoparticles is urgently required, while for photonic films, developing a room-temperature method is of vital importance for the integration of such systems with Si platform. This is challenging but should be feasible in view of rapid advance in the understanding and control of Bi oxidation states in diverse material systems. Fourthly, although fiber lasers have been successfully demonstrated over the past several years, the fibers used are usually tens of meters, indicating that the concentration of Bi active centers is rather low. Finding a route for increasing the concentration of Bi

centers, while suppressing the concentration quenching in fibers, will greatly shorten the fiber length needed. Given that multicomponent glasses possess high solubility of active ions, the study of Bi activated multicomponent glass fibers presents a new research trend, although lots of challenges remain when drawing preforms prepared by these glasses into fibers. Obviously, one of the future focuses is the development of new-wavelength, high-power or ultrashort pulsed laser using newly-developed multicomponent or microstructured glass fibers, in addition to continuous optimization of silica-based fiber laser.

A great number of material systems activated by Bi are still in the research stage, and it is believed that more exciting phenomena as well as novel applicable materials can be found in the near future. Thorough investigation of Bi-activated materials will not only benefit Bi photonics community itself, but also may be helpful for developing new types of photonic materials activated by other p-block elements [250,251].

Acknowledgements

H.-T. Sun gratefully acknowledges the financial support from Soochow University, China, a project of Jiangsu Specially Appointed Professor Program (SR10900214) and a project funded by the Priority Academic Program Development of Jiangsu Higher Education Institutions. J. Zhou acknowledges the financial support from Zhejiang Provincial Natural Science Foundation of China. J. Qiu acknowledges the financial support from the National Natural Science Foundation of China (Grant Nos. 51072054, 51132004), fundamental research funds for the Central Universities (Grant No. 2011ZP0002), Natural Science Foundation of Guangdong Province (S2011030001349) and National Basic Research Program of China (2011CB808102). The authors thank corresponding publishers/authors for the kind permissions to reproduce their materials, especially figures, used in this review.

References

- [1] Jüstel T, Nikol H, Ronda C. New developments in the field of luminescent materials for lighting and displays. *Angew Chem Int Ed* 1998;37:3084–103.
- [2] Binnemans K. Lanthanide-based luminescent hybrid materials. *Chem Rev* 2009;109:4283–374.
- [3] van der Ende BM, Aarts L, Meijerink A. Lanthanide ions as spectral converters for solar cells. *Phys Chem Chem Phys* 2009;11:11081–95.
- [4] Hershaft A, Corbett JD. The crystal structure of bismuth subchloride. Identification of the ion Bi_5^{5+} . *Inorg Chem* 1963;2:979–85.
- [5] Gaft M, Reisfeld R, Panczer G. Luminescence spectroscopy of minerals and materials. Berlin: Springer; 2005.
- [6] Davis HL, Bjerrum NJ, Smith JP. Ligand field theory of $p^{3,4}$ configurations and its application to the spectrum of Bi in molten salt media. *Inorg Chem* 1967;6:1172–8.
- [7] Bjerrum NJ, Smith JP. Lower oxidation states of bismuth. Bi_5^{2+} formed in $\text{AlCl}_3\text{-NaCl}$ melts. *Inorg Chem* 1967;6:1968–72.
- [8] Bjerrum NJ, Davis HL, Smith JP. The optical spectrum of bismuth(I) in the molten aluminum bromide-sodium bromide eutectic. *Inorg Chem* 1967;6:1603–4.
- [9] Bjerrum NJ, Boston CR, Smith JP. Lower oxidation states of bismuth. Bi^+ and Bi_5^{3+} in molten salt solutions. *Inorg Chem* 1967;6:1162–72.
- [10] Corbett J. Homopolyatomic ions of the heavy post-transition elements. the preparation, properties, and bonding of $\text{Bi}_5(\text{AlCl}_4)_3$ and $\text{Bi}_4(\text{A1Cl}_4)$. *Inorg Chem* 1968;7:198–208.
- [11] Ruck M. From the metal to the molecule-ternary bismuth subhalides. *Angew Chem Int Ed* 2001;40:1182–93.
- [12] Ruck M. Bi_7RhBr_8 : a subbromide with molecular $[\text{RhBi}_7]\text{Br}_8$ clusters. *Angew Chem Int Ed Engl* 1997;36:1971–3.
- [13] Ruck M. $\text{Bi}_3\text{Ir}_3\text{Br}_{37}$: a pseudo-symmetric subbromide with Bi_5^+ and Bi_6^{2+} polycations, and $[\text{IrBi}_6\text{Br}_{12}]^-$ and $[\text{IrBi}_6\text{Br}_{12}]^{2-}$ cluster anions. *Z Anorg Allg Chem* 1998;624:521–8.
- [14] Ruck M, Hampel S. Stabilization of homonuclear Bi_5^+ and Bi_6^{2+} polycations by cluster anions in the crystal structures of $\text{Bi}_{12-x}\text{IrCl}_{13-x}$, $\text{Bi}_{12-x}\text{RhCl}_{13-x}$ and $\text{Bi}_{12-x}\text{RhBr}_{13-x}$. *Polyhedron* 2002;21:651–6.
- [15] Ruck M, Dubenskyy V, Söhnle T. Structure and bonding of $\text{Pd}@\text{[Bi}_{10}]^{4+}$ in the subbromide $\text{Bi}_{14}\text{PdBr}_{16}$. *Angew Chem Int Ed* 2003;42:2978–82.
- [16] Dubenskyy V, Ruck M. The subchloride $\text{Bi}_{16}\text{PdCl}_{22}\text{:Pd}@\text{Bi}_{10}^{4+}$ polycations inside a framework of chloro-bismuthate(III) anions. *Z Anorg Allg Chem* 2004;630:2458–62.
- [17] Wahl B, Kloo L, Ruck M. The molecular cluster $[\text{Bi}_{10}\text{Au}_2](\text{SbBi}_3\text{Br}_9)_2$. *Angew Chem Int Ed* 2008;47:3932–5.
- [18] Ahmed E, Köhler D, Ruck M. Room-temperature synthesis of bismuth clusters in ionic liquids and crystal growth of $\text{Bi}_5(\text{AlCl}_4)_3$. *Z Anorg Allg Chem* 2009;635:297–300.
- [19] Kuznetsov AN, Kloo L, Lindsjö M, Rosdahl J, Stoll H. Ab initio calculations on bismuth cluster polycations. *Chem Eur J* 2001;7:2821–8.
- [20] Ulvenlund S, Kloo LB. Formation of subvalent bismuth cations in molten gallium trichloride and benzene solutions. *J Chem Soc Faraday Trans* 1995;91:4223–34.

- [21] Ulvenlund S, Ståhl K, Kloo LB. Structural and quantum chemical study of Bi_5^{3+} and isoelectronic main-group metal clusters. The crystal structure of pentabismuth(3+) tetrachlorogallate(III) refined from X-ray powder diffraction data and synthetic attempts on its antimony analogue. *Inorg Chem* 1996;35:223–30.
- [22] Lindsjö M, Fischer A, Kloo L. Improvements of and insights into the isolation of bismuth polycations from benzene solution – single-crystal structure determinations of $\text{Bi}_8[\text{GaCl}_4]_2$ and $\text{Bi}_5[\text{GaCl}_4]_3$. *Eur J Inorg Chem* 2005;2005:670–5.
- [23] Kuznetsov AN, Popovkin BA, Ståhl K, Lindsjö M, Kloo L. Synthesis of main group polycations in molten and pseudo-molten GaBr_3 media. *Eur J Inorg Chem* 2005;2005:4907–13.
- [24] Wosylus A, Dubenskyy V, Schwarz U, Ruck M. Dynamic disorder of Bi_2^{2+} clusters in the plastic phase ($\text{Bi}_8)_3\text{Bi}[\text{InI}_4]_9$. *Z Anorg Allg Chem* 2009;635:1030–5.
- [25] Akerstedt J, Zaffaroni R, Kloo L. Dichloromethane as solvent for the synthesis of polycationic clusters at room temperature – a link to standard organometallic chemistry. *Dalton Trans* 2010;39:8132–4.
- [26] Xu L, Bobev S, El-Bahraoui J, Sevov SC. A naked diatomic molecule of bismuth, $[\text{Bi}_2]^{2-}$, with a short Bi–Bi bond: synthesis and structure. *J Am Chem Soc* 2000;122:1838–9.
- [27] Gascoin F, Sevov SC. Synthesis and characterization of A_3Bi_2 ($\text{A} = \text{K}, \text{Rb}, \text{Cs}$) with isolated diatomic dianion of bismuth, $[\text{Bi}_2]^{2-}$, and an extra delocalized electron. *J Am Chem Soc* 2000;122:10251.
- [28] Dai D, Whangbo MH, Ugrinov A, Sevov SC, Wang F, Li LM, et al. Analysis of the effect of spin-orbit coupling on the electronic structure and excitation spectrum of the Bi_2^{2-} anion in $(\text{K-crypt})_2\text{Bi}_2$ on the basis of relativistic electronic structure calculations. *J Phys Chem A* 2005;109:1675–83.
- [29] Goicoechea JM, Hull MW, Sevov SC. Heteroatomic deltahedral clusters: synthesis and structures of closo- $[\text{Bi}_3\text{Ni}_4(\text{CO})_6]^{3-}$, closo- $[\text{Bi}_4\text{Ni}_4(\text{CO})_6]^{2-}$, the open cluster $[\text{Bi}_3\text{Ni}_6(\text{CO})_9]^{3-}$, and the intermetallic closo- $[\text{Nix}@\{\text{Bi}_6\text{Ni}_6(\text{CO})_8\}]^{4-}$. *J Am Chem Soc* 2007;129:7885–93.
- [30] Goicoechea JM, Sevov SC. $[\text{Zn}_9\text{Bi}_{11}]^{5-}$: a ligand-free intermetallic cluster. *Angew Chem Int Ed* 2006;45:5147.
- [31] Dubenskyy V, Ruck M. $\text{Bi}_{32}\text{InBr}_{48}$: a polar subhalide with Bi_9^{5+} polycations, complex bromobismuthate(III) anions $[\text{Bi}_3\text{Br}_{13}]^{4-}$ and $[\text{Bi}_3\text{Br}_{30}]^{9-}$, and pentabromoindate(III) anions $[\text{InBr}_5]^{2-}$. *Z Anorg Allg Chem* 2003;629:375–80.
- [32] Kuznetsov AN, Naumenko PI, Popovkin BA, Kloo L. New representative of Bi_5^{5+} containing phases: synthesis and crystal structure of the Nb^{IV} -containing $\text{Bi}_{10}\text{Nb}_3\text{Cl}_{18}$ compound. *Russ Chem Bull, Int Ed* 2003;52:2100–4.
- [33] Sun HT, Sakka Y, Gao H, Miwa Y, Fujii M, Shirahata N, et al. Ultrabroad near infrared photoluminescence from $\text{Bi}_5(\text{AlCl}_4)_3$ crystal. *J Mater Chem* 2011;21:4060–3.
- [34] Sun HT, Sakka Y, Shirahata N, Gao H, Yonezawa T. Experimental and theoretical studies of photoluminescence from Bi_8^{3+} and Bi_5^{3+} stabilized by $[\text{AlCl}_4]^-$ in molecular crystals. *J Mater Chem* 2012;22:12837–41.
- [35] Sun HT, Xu BB, Yonezawa T, Sakka Y, Shirahata N, Fujii M, et al. Photoluminescence from $\text{Bi}_5(\text{GaCl}_4)_3$ molecular crystal. *Dalton Trans* 2012;41:11055–61.
- [36] Krebs B, Hucke M, Brendel CJ. Structure of the octabismuth (2+) cluster in crystalline $\text{Bi}_8(\text{AlCl}_4)_2$. *Angew Chem Int Ed Engl* 1982;21:445–6.
- [37] Sun HT, Matsushita Y, Sakka Y, Shirahata N, Tanaka M, Katsuya Y, et al. Synchrotron X-ray, photoluminescence and quantum chemistry studies of bismuth embedded dehydrated zeolite Y. *J Am Chem Soc* 2012;134:2918–21.
- [38] Blasse G, Bril A. Study of energy transfer from Sb^{3+} , Bi^{3+} , Ce^{3+} to Sm^{3+} , Eu^{3+} , Tb^{3+} , Dy^{3+} . *J Chem Phys* 1967;47:1920–6.
- [39] Blasse G, Meijerink A, Zuidema J. Unusual bismuth luminescence in strontium tetraborate ($\text{SrB}_4\text{O}_7\text{:Bi}$). *J Phys Chem Solids* 1994;55:171–4.
- [40] Blasse G. Classical phosphors: a Pandora's box. *J Lumin* 1997;72–74:129–34.
- [41] Boulon G, Moine B, Bourcet JC. Spectroscopic properties of ${}^3\text{P}_1$ and ${}^3\text{P}_0$ excited states of Bi^{3+} ions in germanate glass. *Phys Rev B* 1980;22:1163–9.
- [42] Partington JR. A history of chemistry. London: Macmillan; 1961.
- [43] Sadler PJ, Li H, Sun H. Coordination chemistry of metals in medicine: target sites for bismuth. *Coordin Chem Rev* 1999;185–186:689–709.
- [44] Reisfeld R, Lieblich N, Boehm L. Energy transfer between $\text{Bi}^{3+} \rightarrow \text{Eu}^{3+}$, $\text{Bi}^{3+} \rightarrow \text{Sm}^{3+}$, and $\text{UO}_2^{2+} \rightarrow \text{Eu}^{3+}$ in oxide glasses. *J Lumin* 1976;12(13):749–53.
- [45] Reisfeld R, Kalisky Y. Energy transfer between Bi^{3+} and Nd^{3+} in germanate glass. *Chem Phys Lett* 1977;50:199–201.
- [46] Nikl M, Novoselov A, Mihoková E, Polák K, Dusek M, McClune B, et al. Photoluminescence of Bi^{3+} in $\text{Y}_3\text{Ga}_5\text{O}_{12}$ single-crystal host. *J Phys: Condens Matter* 2005;17:3367–75.
- [47] Su Q, Barthou C, Denis JP, Pelle F, Blanzat B. Luminescence and energy transfer in Y_2O_3 co-doped with Bi^{3+} and Eu^{3+} . *J Lumin* 1983;28:1–11.
- [48] Blasse G. Luminescence of inorganic solids: from isolated centres to concentrated systems. *Prog Solid State Chem* 1988;18:79–171.
- [49] Wang M, Fan XP, Xiong GH. Luminescence of Bi^{3+} ions and energy transfer from Bi^{3+} ions to Eu^{3+} ions in silica glasses prepared by the sol-gel process. *J Phys Chem Solids* 1995;56:859–62.
- [50] Srivastava AM. On the luminescence of Bi^{3+} in the pyrochlore $\text{Y}_2\text{Sn}_2\text{O}_7$. *Mater Res Bull* 2002;37:745–51.
- [51] Zorenko Y, Pashkovsky M, Voloshinovskii A, Kuklinski B, Grinberg M. The luminescence of CaWO_4 : Bi single crystals. *J Lumin* 2006;116:43–51.
- [52] Sontakke AD, Tarafder A, Biswas K, Annapurna K. Sensitized red luminescence from Bi^{3+} co-doped Eu^{3+} : $\text{ZnO}-\text{B}_2\text{O}_3$ glasses. *Physica B* 2009;404:3525–9.
- [53] Hamstra MA, Folkerts HF, Blasse G. Materials chemistry communications. Red bismuth emission in alkaline-earth-metal sulfates. *J Mater Chem* 1994;4:1349–50.
- [54] Gaft M, Reisfeld R, Panczer G, Boulon G, Saraiarov T, Erlish S. The luminescence of Bi, Ag and Cu in natural and synthetic barite BaSO_4 . *Opt Mater* 2001;16:279–90.
- [55] Srivastava A. Luminescence of divalent bismuth in $\text{M}^{2+}\text{BPO}_5$ ($\text{M}^{2+} = \text{Ba}^{2+}$, Sr^{2+} and Ca^{2+}). *J Lumin* 1998;78:239–43.
- [56] Peng MY, Wondraczek L. Bi^{2+} -doped strontium borates for white-light-emitting diodes. *Opt Lett* 2009;34:2885–7.
- [57] Peng MY, Wondraczek L. Photoluminescence of $\text{Sr}_2\text{P}_2\text{O}_7:\text{Bi}^{2+}$ as a red phosphor for additive light generation. *Opt Lett* 2010;35:2544–6.

- [58] Topol LE, Yosim SJ, Osteryoung RA. E.M.F. measurements in molten bismuth–bismuth trichloride solutions. *J Phys Chem* 1961;65:1511–6.
- [59] Boston CR, Smith GP. Spectra of dilute solutions of bismuth metal in molten bismuth trihalides. I. Evidence for two solute species in the system bismuth–bismuth trichloride. *J Phys Chem* 1962;66:1178–81.
- [60] Boston CR, Smith GP, Howick LC. Spectra of dilute solutions of bismuth metal in molten bismuth trihalides. II. Formulation of solute equilibrium in bismuth trichloride. *J Phys Chem* 1963;67:1849–52.
- [61] Sun HT, Sakka Y, Fujii M, Shirahata N, Gao H. Ultrabroad near-infrared photoluminescence from ionic liquids containing subvalent bismuth. *Opt Lett* 2011;36:100–2.
- [62] Romanov AN, Fattakhova ZT, Veber AA, Usovich OV, Haula EV, Korchak VN, et al. On the origin of near-IR luminescence in Bi-doped materials (II). Subvalent monocation Bi^+ and cluster Bi_5^{3+} luminescence in $\text{AlCl}_3/\text{ZnCl}_2/\text{BiCl}_3$ chloride glass. *Opt Express* 2012;20:7212–20.
- [63] Keller OL, Nestor CWJ, Fricke B. Predicted properties of the superheavy elements. III. Element 115, eka-bismuth. *J Phys Chem* 1974;78:1945–9.
- [64] Bergerhoff G, Kilger B, Withauer C, Hundt R, Sievers R. User's Manual ICSD – CRYSTIN. Bonn: Institut für Anorganische Chemie der Universität; 1986.
- [65] Mingoe DMP. Polyhedral skeletal electron pair approach. *Acc Chem Res* 1984;17:311–9.
- [66] Cao RP, Peng MY, Wondraczek L, Qiu JR. Superbroad near-to-mid-infrared luminescence from Bi_5^{3+} in $\text{Bi}_5(\text{AlCl}_4)_3$. *Opt Express* 2012;20:2562–71.
- [67] Scharfe S, Kraus F, Stegmaier S, Schier A, Fässler TF. Zintl ions, cage compounds, and intermetallic clusters of group 14 and group 15 elements. *Angew Chem Int Ed* 2011;50:3630–70.
- [68] Corbett JD, Adolphson DG, Merryman DJ, Edwards PA, Armatis FJ. Synthesis of stable homopolyatomic anions of antimony, bismuth, tin, and lead. Crystal structure of a salt containing the heptaantimonide(3-) anion. *J Am Chem Soc* 1975;97:6267–8.
- [69] Sun HT, Yonezawa T, Gillett-Kunnath MM, Sakka Y, Shirahata N, Gui SCR, et al. Ultra-broad near-infrared photoluminescence from crystalline $(\text{K-crypt})_2\text{Bi}_2$ containing $[\text{Bi}_2]^{2-}$ dimers. *J Mater Chem* 2012;22:20175–8.
- [70] Sokolov VO, Plotnichenko VG, Koltashev VV, Dianov EM. Centres of broadband near-IR luminescence in bismuth-doped glasses. *J Phys D Appl Phys* 2009;42:095410.
- [71] Dianov EM, Dvoyrin VV, Mashinsky VM, Umnikov AA, Yashkov MV, Guryanov AN. CW bismuth fiber laser. *Quant Electron* 2005;35:1083–4.
- [72] Sun HT, Yang JJ, Fujii M, Sakka Y, Zhu Y, Asahara T, et al. Highly fluorescent silica-coated bismuth doped aluminosilicate nanoparticles for near infrared bioimaging. *Small* 2011;7:199–203.
- [73] Fink EH, Setzer KD, Ramsay DA, Vervloet M. A new band spectrum of BiO in the near-infrared region. *Chem Phys Lett* 1991;179:103–8.
- [74] Fink EH, Setzer KD, Ramsay DA, Vervloet M. The $\text{X}_2\text{I} \rightarrow \text{X}_1\text{O}^+$ electronic band systems of bismuth monohalides in the near infrared. *Chem Phys Lett* 1991;179:95–102.
- [75] Fink EH, Shestakov O. The a ${}^3\Sigma^*(\text{a}_1\text{I})-\text{X}^1\Sigma^*(\text{X}\text{O}^+)$ transition of BiN . *Chem Phys Lett* 1993;211:473.
- [76] Fink EH, Setzer KD, Ramsay DA, Towle JP, Brown JM. High-resolution study of the $\text{X}_2\text{I} \rightarrow \text{X}_1\text{O}^+$ fine-structure transition of BiF . *J Mol Spectrosc* 1996;178:143–56.
- [77] Fink EH, Shestakov O, Setzer KD. Fine structure transitions of BiOH in the near-infrared region. *J Mol Spectrosc* 1997;183:163–7.
- [78] Shestakov O, Demes H, Setzer KD, Fink EH. Electronic states and spectra of BiO . *J Mol Spectrosc* 1998;190:28–77.
- [79] Setzer KD, Uibel C, Zyrnicki W, Pravilov AM, Fink EH, Liebermann HP, et al. Experimental and theoretical study of the electronic states and spectra of BiNa . *J Mol Spectrosc* 2000;204:163–75.
- [80] Gerber G, Broida HP. Electronic states and molecular constants of Bi_2 . *J Chem Phys* 1976;64:3423–37.
- [81] Gerber G, Sakurai K, Broida HP. Laser photoluminescence of Bi_2 . *J Chem Phys* 1976;64:3410–22.
- [82] Teichman III RA, Nixon ER. Some new states of matrix-isolated diatomic bismuth. *J Chem Phys* 1977;67:2470–2.
- [83] West WP, Broida HP. Optically pumped vapor phase Bi_2 laser. *Chem Phys Lett* 1978;56:283–5.
- [84] Wellegehausen B, Friede D, Steger G. Optically pumped continuous Bi_2 and Te_2 lasers. *Opt Commun* 1978;26:391–5.
- [85] Bondybey VE, English JH. Laser fluorescence studies of metal clusters: spectroscopy of molecular bismuth. *J Chem Phys* 1980;73:42–8.
- [86] Ahmed F, Nixon ER. Matrix-isolated bismuth. II. New fluorescence band systems and resonance Raman spectra of Bi_2 and Bi_4 in solid argon. *J Chem Phys* 1981;75:110–3.
- [87] Zhou SF, Jiang N, Zhu B, Yang H, Ye S, Lakshminarayana G, et al. Multifunctional Bi-doped nanoporous silica glass: from blue-green, orange, red and white light sources to ultra broadband infrared amplifiers. *Adv Funct Mater* 2008;18:1407–13.
- [88] Fujimoto Y, Nakatsuka M. Infrared luminescence from bismuth-doped silica glass. *Jpn J Appl Phys* 2001;40:L279–81.
- [89] Fujimoto Y, Nakatsuka M. Optical amplification in bismuth-doped silica glass. *Appl Phys Lett* 2003;52:3325–7.
- [90] Peng MY, Qiu JR, Chen DP, Meng XG, Zhu CS. Broadband infrared luminescence from $\text{Li}_2\text{O}-\text{Al}_2\text{O}_3-\text{ZnO}-\text{SiO}_2$ glasses doped with Bi_2O_3 . *Opt Express* 2005;13:6892–8.
- [91] Meng XG, Qiu JR, Peng MY, Chen DP, Zhao QZ, Jiang XW, et al. Infrared broadband emission of bismuth-doped barium-aluminum-borate glasses. *Opt Express* 2005;13:1635–42.
- [92] Meng XG, Qiu JR, Peng MY, Chen DP, Zhao QZ, Jiang XW, et al. Near infrared broadband emission of bismuth-doped aluminophosphate glass. *Opt Express* 2005;13:1628–34.
- [93] Peng MY, Qiu JR, Chen DP, Meng XG, Zhu CS. Superbroadband 1310 nm emission from bismuth and tantalum codoped germanium oxide glasses. *Opt Lett* 2005;30:2433–5.
- [94] Peng MY, Qiu JR, Chen DP, Meng XG, Yang LY, Jiang XW, et al. Bismuth- and aluminum-codoped germanium oxide glasses for super-broadband optical amplification. *Opt Lett* 2004;29:1998–2000.
- [95] Peng MY, Dong GP, Wondraczek L, Zhang LL, Zhang N, Qiu JR. Discussion on the origin of NIR emission from Bi-doped materials. *J Non-Cryst Solids* 2011;357:2241–5.
- [96] West AR. Solid state chemistry and its applications. New York: John Wiley and Sons LTD; 1991.

- [97] Hagenmuller P. Preparative methods in solid state chemistry. New York: Academic Press; 1972.
- [98] Zhang QY, Huang XY. Recent progress in quantum cutting phosphors. *Prog Mater Sci* 2010;55:353–427.
- [99] Sun HT, Shimaoka F, Miwa Y, Ruan J, Fujii M, Qiu JR, et al. Sensitized superbroadband near-IR emission in bismuth glass/Si nanocrystal superlattices. *Opt Lett* 2010;35:2215–7.
- [100] Miwa Y, Sun HT, Imakita K, Fujii M, Teng Y, Qiu JR, et al. Sensitized broadband near-infrared luminescence from bismuth-doped silicon-rich silica films. *Opt Lett* 2011;36:4221–3.
- [101] Kim Y, Seff K. The Octahedral hexasilver molecule: seven crystal structures of variously vacuum-dehydrated fully Ag⁺-exchanged zeolite A. *J Am Chem Soc* 1978;100:6989–97.
- [102] Meyers RA. Encyclopedia of analytical chemistry. Chichester: John Wiley & Sons Ltd; 2000.
- [103] Rietveld HM. A profile refinement method for nuclear and magnetic structures. *J Appl Crystallogr* 1969;2:65–71.
- [104] David WIF, Shankland K, McCusker LB, Baerlocher C. Structure determination form powder diffraction data. *Int Union Crystallogr Monogr Crystallogr* 2002;10.
- [105] Larson AC, Von Dreele RB. General structure analysis system (GSAS). Los Alamos National Laboratory; 1994.
- [106] Coelho AA. TOPAS v2.0: general profile and structure analysis software for powder diffraction data. Karlsruhe; 2000.
- [107] David WIF, Shankland K, van de Streek J, Pidcock E, Motherwell WDS, Cole JC. DASH: a program for crystal structure determination from powder diffraction data. *J Appl Crystallogr* 2006;39:910–5.
- [108] Morgan WE, Stec WJ, Van Wazer JR. Inner-orbital binding-energy shifts of antimony and bismuth compounds. *Inorg Chem* 1973;12:953–5.
- [109] Grunwaldt JD, Wildberger MD, Mallat T, Baiker A. Unusual redox properties of bismuth in sol-gel Bi-Mo-Ti mixed oxides. *J Catal* 1998;177:53–9.
- [110] Qian M, Yu CL, Cheng JM, Li KF, Hu LL. The broadband NIR emission properties of Bi doped La₂O₃–Al₂O₃–SiO₂ glass. *J Lumin* 2012;132:2634–8.
- [111] Stern EA. Musing about the development of XAFS. *J Synchrotron Rad* 2001;8:49–54.
- [112] Witkowska A, Rybicki J, Di Cicco A. EXAFS analysis of bismuth atom neighbourhood in reduced bismuth silicate glass. *Phys Chem Glasses* 2002;43C:124–7.
- [113] Kuznetsov AN, Popovkin BA, Henderson W, Taylor MJ, Bengtsson-Kloo L. Monocations of bismuth and indium in arene media: a spectroscopic and EXAFS investigation. *J Chem Soc Dalton Trans* 2000;1777–81.
- [114] Naslund J, Persson I, Sandstrom M. Solvation of the bismuth(III) ion by water, dimethyl sulfoxide, N,N'-dimethylpropyleneurea, and N,N-dimethylthioformamide. An EXAFS, large-angle X-ray scattering, and crystallographic structural study. *Inorg Chem* 2000;39:4012–21.
- [115] Lyczko K, Bilewicz A, Persson I. Stabilization of a subvalent oxidation state of bismuth in N,N-dimethylthioformamide solution: an EXAFS, UV-Vis, IR, and cyclic voltammetry study. *Inorg Chem* 2004;43:7094–100.
- [116] Ikemoto H, Deto K, Miyanaga T. EXAFS study of the local structure for semimetal–semiconductor transition in bismuth clusters. *e-J Surf Sci Nanotech* 2005;3:370–2.
- [117] Ohkura T, Fujimoto Y, Nakatsuka M. Local structures of bismuth ion in bismuth-doped silica glasses analyzed using Bi L_{III} X-ray absorption fine structure. *J Am Ceram Soc* 2007;90:3596–600.
- [118] Hamaed H, Laschuk MW, Terskikh VV, Schurk RW. Application of solid-state ²⁰⁹Bi NMR to the structural characterization of bismuth-containing materials. *J Am Ceram Soc* 2009;131:8271–9.
- [119] Khonthon S, Morimoto S, Arai Y, Ohishi Y. Luminescence characteristics of Te- and Bi-doped glasses and glass-ceramics. *J Ceram Soc Jpn* 2007;115:259–63.
- [120] Day G, Glaser R, Shimomura N, Takamuku A, Ichikawa K. Electronic excitations in homopolyatomic bismuth cations: spectroscopic measurements in molten salts and an ab initio Cl-singles study. *Chem Eur J* 2000;6:1078–86.
- [121] Yuan HK, Chen H, Kuang AL, Miao Y, Xiong ZH. Density-functional study of small neutral and cationic bismuth clusters Bi_n and Bi_n⁺ (n = 2–24). *J Chem Phys* 2008;128:094305.
- [122] Blasse G, Bril A. Investigations on Bi³⁺-activated phosphors. *J Chem Phys* 1968;48:217–22.
- [123] Jørgensen CK. Absorption spectra and chemical bonding in complexes. New York: Pergamon Press Inc; 1962. p. 186.
- [124] Simons PY. Luminescence of Bi³⁺-activated LaOCl under X-ray excitation. *J Electrochem Soc* 1971;118:148–9.
- [125] Jacquier B, Boulon B, Sallavuard G, Gaume-Mahn F. Bi³⁺ center in a lanthanum gallate phosphor. *J Solid State Chem* 1972;4:374–8.
- [126] Weber MJ, Monchamp RR. Luminescence of Bi₄Ge₃O₁₂: spectral and decay properties. *J Appl Phys* 1973;44:5495–9.
- [127] Dickinson SK, Hilton RM, Lipson HG. Czochralski synthesis and properties of rare-earth-doped bismuth germanate (Bi₄Ge₃O₁₂). *Mater Res Bull* 1972;7:181–91.
- [128] Boulon G, Moine B, Bourcet JC. Time resolved spectroscopy about ³P₁ and ³P₀ levels in Bi³⁺ doped germanate glasses. *J Lumin* 1979;18(19):924–8.
- [129] Boulon G, Moine B, Bourcet JC. Spectroscopic properties of ³P₁ and ³P₀ excited states of Bi³⁺ ions in germanate glass. *Phys Rev B* 1980;22:1163–9.
- [130] Wang MQ, Fan XP, Xiong GH. Luminescence of Bi³⁺ ions and energy transfer from Bi³⁺ ions to Eu³⁺ ions in silica glasses prepared by the sol-gel process. *J Phys Chem Solids* 1995;56:859–62.
- [131] Xu WB, Peng MY, Ma ZJ, Dong GP, Qiu JR. A new study on bismuth doped oxide glasses. *Opt Express* 2012;20:15692–702.
- [132] Kroeger FA, Overbeek JTG, Goorissen J, van den Boomgaard J. Bismuth as activator in fluorescent solids. *J Electrochem Soc* 1949;96:132–41.
- [133] Meijerink A, Nuyten J, Blasse G. Luminescence and energy migration in (Sr, Eu) B₄O₇, a system with a 4f⁷–4f⁶5d crossover in the excited state. *J Lumin* 1989;44:19–31.
- [134] Blasse G, Dirksen GJ, Meijerink A. The luminescence of ytterbium (II) in strontium tetraborate. *Chem Phys Lett* 1990;167:41–4.
- [135] Lacam A, Chateau C. Highpressure measurements at moderate temperatures in a diamond anvil cell with a new optical sensor: SrB₄O₇:Sm²⁺. *J Appl Phys* 1989;66:366–72.
- [136] Verwey JWM, Dirksen GJ, Blasse G. The luminescence of divalent and trivalent rare earth ions in the crystalline and glass modifications of SrB₄O₇. *J Phys Chem Solids* 1992;53:367–75.

- [137] Peng MY, Wondraczek L. Orange-to-red emission from Bi^{2+} and alkaline earth codoped strontium borate phosphors for white light emitting diodes. *J Am Ceram Soc* 2010;93:1437–42.
- [138] Peng MY, Da N, Krolikowski S, Stiegelschmitt A, Wondraczek L. Luminescence from Bi^{2+} -activated alkali earth borophosphates for white LEDs. *Opt Express* 2009;17:21169–78.
- [139] Brown ID, Calvo C. The crystal chemistry of large cation dichromates, pyrophosphates, and related compounds with stoichiometry $\text{X}_2\text{Y}_2\text{O}_7$. *J Solid State Chem* 1970;1:173–9.
- [140] Ye S, Liu ZS, Wang JG, Jing XP. Luminescent properties of $\text{Sr}_2\text{P}_2\text{O}_7$: Eu, Mn phosphor under near UV excitation. *Mater Res Bull* 2008;43:1057–65.
- [141] Reisfeld R, Boehm L. Optical properties of bismuth in germanate, borax and phosphate glasses. *J Non-Cryst Solids* 1974;16:83–92.
- [142] Murata K, Fujimoto Y, Kanabe T, Fujita H, Nakatsuka M. Bi-doped SiO_2 as a new laser material for an intense laser. *Fusion Eng Des* 1999;44:437–9.
- [143] Ren JJ, Yang LY, Qiu JR, Chen DP, Jiang XW, Zhu CS. Effect of various alkaline-earth metal oxides on the broadband infrared luminescence from bismuth-doped silicate glasses. *Solid State Commun* 2006;140:38–41.
- [144] Peng MY, Chen DP, Qiu JR, Jiang XW, Zhu CS. Bismuth-doped zinc aluminosilicate glasses and glass-ceramics with ultra-broadband infrared luminescence. *Opt Mater* 2007;29:556–61.
- [145] Zhou SF, Dong HF, Feng HP, Feng GF, Yang HC, Zhu B, et al. Broadband optical amplification in Bi-doped germanium silicate glass. *Appl Phys Lett* 2007;91:061919–61921.
- [146] Xia HP, Wang XJ. Near infrared broadband emission from Bi^{5+} -doped $\text{Al}_2\text{O}_3\text{-GeO}_2\text{-X}$ ($\text{X} = \text{Na}_2\text{O}, \text{BaO}, \text{Y}_2\text{O}_3$) glasses. *Appl Phys Lett* 2006;89:051917–51920.
- [147] Suzuki T, Ohishi Y. Ultrabroadband near-infrared emission from Bi-doped $\text{Li}_2\text{O}\text{-Al}_2\text{O}_3\text{-SiO}_2$ glass. *Appl Phys Lett* 2006;88:191912–4.
- [148] Arai Y, Suzuki T, Ohishi Y, Morimoto S, Khonthon S. Ultrabroadband near-infrared emission from a colorless bismuth-doped glass. *Appl Phys Lett* 2007;90:261110–2.
- [149] Hughes MA, Akada T, Suzuki T, Ohishi Y, Hewak DW. Ultrabroad emission from a bismuth doped chalcogenide glass. *Opt Express* 2009;17:19345–55.
- [150] Yang G, Chen DP, Ren J, Xu YS, Zeng HD, Yang YX, et al. Effects of melting temperature on the broadband infrared luminescence of Bi-doped and Bi/Dy co-doped chalcohalide glasses. *J Am Ceram Soc* 2007;90:3670–2.
- [151] Ren JJ, Dong GP, Xu SQ, Bao RQ, Qiu JR. Inhomogeneous broadening, luminescence origin and optical amplification in bismuth-doped glass. *J Phys Chem A* 2008;112:3036–9.
- [152] Peng MY, Wu BT, Da N, Wang C, Chen DP, Zhu CS, et al. Bismuth-activated luminescent materials for broadband optical amplifier in WDM system. *J Non-Cryst Solids* 2008;354:1221–5.
- [153] Peng MY, Zollfrank C, Wondraczek L. Origin of broad NIR photoluminescence in bismuthate glass and Bi-doped glasses at room temperature. *J Phys Condens Matter* 2009;21:285106–11.
- [154] Denker Bl, Galagan Bl, Osiko VV, Sverchkov SE, Dianov EM. Luminescent properties of Bi-doped boro-alumino-phosphate glasses. *Appl Phys B* 2007;87:135–7.
- [155] Sokolov VO, Plotnichenko VG, Dianov EM. Origin of broadband near-infrared luminescence in bismuth-doped glasses. *Opt Lett* 2008;33:1488–90.
- [156] Denker Bl, Galagan Bl, Osiko VV, Shulman IL, Sverchkov SE, Dianov EM. Absorption and emission properties of Bi-doped Mg-Al-Si oxide glass system. *Appl Phys B* 2009;95:801–5.
- [157] Denker Bl, Galagan Bl, Shulman IL, Sverchkov SE, Dianov EM. Spectral and luminescent properties of Bi-doped bulk glasses and factors acting on them. *Opt Compon Mater VII* 2010;7598:759805–10.
- [158] Denker Bl, Galagan Bl, Osiko VV, Shulman IL, Sverchkov SE, Dianov EM. Factors affecting the formation of near infrared-emitting optical centers in Bi-doped glasses. *Appl Phys B* 2010;98:455–8.
- [159] Romanov AN, Haula EV, Fattakhova ZT, Veber AA, Tsvetkov VB, Zhigunov DM, et al. Near-IR luminescence from subvalent bismuth species in fluoride glass. *Opt Mater* 2011;34:155–8.
- [160] Peng MY, Zhang N, Wondraczek L, Qiu JR, Yang ZM, Zhang QY. Ultrabroad NIR luminescence and energy transfer in Bi and Er/Bi co-doped germinate glasses. *Opt Express* 2011;19:20799–807.
- [161] Xu BB, Zhou SF, Guan MJ, Tan DZ, Teng Y, Zhou JJ, et al. Unusual luminescence quenching and reviving behavior of Bi-doped germinate glasses. *Opt Express* 2011;19:23436–43.
- [162] Tong LM, Gattass RR, Ashcom JB, He SL, Lou JY, Shen MY, et al. Subwavelength-diameter silica wires for low-loss optical wave guiding. *Nature* 2003;426:816–9.
- [163] Carmon T, Vahala Kj. Visible continuous emission from a silica microphotonic device by third-harmonic generation. *Nat Phys* 2007;3:430–5.
- [164] Del'Haye P, Schliesser A, Arcizet O, Wilken T, Holzwarth R, Kippenberg TJ. Optical frequency comb generation from a monolithic microresonator. *Nature* 2007;450:1214–7.
- [165] Zhou SF, Lei WQ, Jiang N, Hao JH, Wu E, Zeng HP, et al. Space-selective control of luminescence inside the Bi-doped mesoporous silica glass by a femtosecond laser. *J Mater Chem* 2009;19:4603–8.
- [166] Zhang LL, Dong GP, Wu JD, Peng MY, Qiu JR. Excitation wavelength-dependent near-infrared luminescence from Bi-doped silica glass. *J Alloy Compd* 2012;531:10–3.
- [167] Duffy JA, Ingram MD. An interpretation of glass chemistry in terms of the optical basicity concept. *J Non-Cryst Solids* 1976;21:373–410.
- [168] Guan MJ, Wang X, Zhuang YX, Lin G, Xie JH, Smedskjr MM, et al. Abnormal luminescence behavior in Bi-doped borosilicate glasses. *J Electrochem Soc* 2011;158:G151–4.
- [169] Ruan J, Dong GP, Liu XF, Zhang Q, Chen DP, Qiu JR. Enhanced broadband near-infrared emission and energy transfer in Bi-Tm-codoped germanate glasses for broadband optical amplification. *Opt Lett* 2009;34:2486–8.
- [170] Merkulov EB, Logoveev NA, Goncharuk VK, Yaroshenko RM. Glass formation in the $\text{ZrF}_4\text{-BiF}_3\text{-MeF}$ ($\text{Me} = \text{Li}, \text{Na}, \text{K}$) fluoride systems. *Glass Phys Chem* 2007;33:106–8.
- [171] Merkulov EV, Goncharuk VK, Logoveev NA, Tararako EA, Michteeva EY. New lead-fluorozirconate glasses containing BiF_3 . *J Non-Cryst Solids* 2005;351:3607–9.

- [172] Ignat'eva LN, Merkulov EB, Stremousova EA, Plotnichenko VG, Koltashev VV, Buznik VM. Effect of bismuth trifluoride on the characteristics of fluoroindate glasses: the $\text{InF}_3\text{-BiF}_3\text{-BaF}_2$ system. *Russ J Inorg Chem* 2006;51:1641–5.
- [173] Razdobreev I, Hamzaoui HE, Ivanov VY, Kustov EF, Capoen B, Bouazaoui M. Optical spectroscopy of bismuth-doped pure silica fiber preform. *Opt Lett* 2010;35:1341–3.
- [174] Razdobreev I, Bigot L. On the multiplicity of bismuth active centres in germano-aluminosilicate preform. *Opt Mater* 2011;33:973–7.
- [175] Gumenyuk R, Golant K, Okhotnikov OG. Energy transition characterization of 1.18 and 1.3 μm bands of bismuth fiber by spectroscopy of the transient oscillations. *Appl Phys Lett* 2011;98:191108–10.
- [176] Schweizer T, Samson BN, Hector JR, Brocklesby WS, Hewak DW, Payne DN. Infrared emission from holmium doped gallium lanthanum sulphide glass. *Infrared Phys Technol* 1999;40:329–35.
- [177] Hughes M, Rutt H, Hewak D, Curry R. Spectroscopy of vanadium (III) doped gallium lanthanum sulphide chalcogenide glass. *Appl Phys Lett* 2007;90:031108–10.
- [178] Hughes MA, Curry RJ, Hewak DW. Spectroscopy of titanium-doped gallium lanthanum sulfide glass. *J Opt Soc Am B* 2008;25:1458–65.
- [179] Dong GP, Xiao XD, Ren JJ, Ruan J, Liu XF, Qiu JR, et al. Broadband infrared luminescence from bismuth-doped $\text{GeS}_2\text{-GaS}_3$ chalcogenide glasses. *Chin Phys Lett* 2008;25:1891–4.
- [180] Dvoyrin VV, Mashinsky VM, Dianov EM, Umnikov AA, Yashkov MV, Guryanov AN. Absorption, fluorescence and optical amplification in MCVD bismuth-doped silica glass optical fibres. In: European conference on optical communications 2005, Glasgow; September 25–29, 2005. paper Th 3.3.5.
- [181] Haruna T, Kakui M, Taru T, Ishikawa S, Onishi M. Silica-based bismuth-doped fiber for ultra broad band light-source and optical amplification around 1.1 μm . In: Optical amplifiers and their applications topical meeting, Budapest; August 7–10, 2005. paper MC3.
- [182] Dvoyrin VV, Mashinsky VM, Bulatov LI, Bufetov IA, Shubin AV, Melkumov MA, et al. Bismuth-doped-glass optical fibers—a new active medium for lasers and amplifiers. *Opt Lett* 2006;31:2966–8.
- [183] Bufetov IA, Dianov EM. Bi-doped fiber lasers. *Laser Phys Lett* 2009;6:487–504.
- [184] Razdobreev I, Bigot L, Pureur V, Bouwmans G, Douay M. Broadband and efficient bismuth fiber laser around 1.2 μm . 15th International laser physics workshop (LPHYS'06), Lausanne, Switzerland; July 24–28, 2006.
- [185] Dianov EM, Firstov SV, Khopin VF, Guryanov AN, Bufetov IA. Bi-doped fibre lasers and amplifiers emitting in a spectral region of 1.3 μm . *Quant Electron* 2008;38:615–7.
- [186] Bufetov IA, Firstov SV, Khopin VF, Medvedkov OI, Guryanov AN, Dianov EM. Bi-doped fiber lasers and amplifiers for a spectral region of 1300–1470 nm. *Opt Lett* 2008;33:2227–9.
- [187] Truong VG, Bigot L, Lerouge A, Douay M. Study of thermal stability and luminescence quenching properties of bismuth-doped silicate glasses for fiber laser applications. *Appl Phys Lett* 2008;92:041908–10.
- [188] Dianov EM, Firstov SV, Medvedkov OI, Bufetov IA, Khopin VF, Guryanov AN. Luminescence and laser generation in Bi-doped fibers in a spectral region of 1300–1520 nm. In: Optical fiber communication conference (OFC'2009), San Diego, CA, USA; March 22–26, 2009. paper OWT3.
- [189] Fistov SV, Bufetov IA, Khopin VF, Umnikov AA, Guryanov AN, Dianov EM. Time-resolved spectroscopy and optical gain of silica-based fibers co-doped with Bi, Al and/or Ge, P, and Ti. *Laser Phys* 2009;19:894–901.
- [190] Dvoyrin VV, Medvedkov OI, Mashinsky VM, Umnikov AA, Guryanov AN, Dianov EM. Optical amplification in 1430–1495 nm range and laser action in Bi-doped fibers. *Opt Express* 2008;16:16971–6.
- [191] Qiu YQ, Shen YH. Investigation on the spectral characteristics of bismuth doped silica fibers. *Opt Mater* 2008;31:223–8.
- [192] Qiu YQ, Shen YH. Fluorescence emission centers and the corresponding infrared fluorescence saturation in a bismuth-doped silica fibre. *Chin Phys Lett* 2008;25:2527–30.
- [193] Kir'yanov AV, Dvoyrin VV, Mashinsky VM, Barmenkov YO, Dianov EM. Nonsaturable absorption in alumino-silicate bismuth-doped fibers. *J Appl Phys* 2011;109: 023113–10.
- [194] Kir'yanov AV, Dvoyrin VV, Mashinsky VM, Il'ichev NN, Kozlova NS, Dianov EM. Influence of electron irradiation on optical properties of bismuth doped silica fibers. *Opt Express* 2011;19:6599–608.
- [195] Bufetov IA, Melkumov MA, Firstov SV, Shubin AV, Semenov SL, Vel'miskin VV, et al. Optical gain and laser generation in bismuth-doped silica fibers free of other dopants. *Opt Lett* 2011;36:166–8.
- [196] Razdobreev I, El Hamzaoui H, Bigot L, Arion V, Bouwmans G, Le Rouge A, et al. Optical properties of bismuth-doped silica core photonic crystal fiber. *Opt Express* 2010;18:19479–84.
- [197] Fistov SV, Khopin VF, Bufetov IA, Firstova EG, Guryanov AN, Dianov EM. Combined excitation–emission spectroscopy of bismuth active centers in optical fibers. *Opt Express* 2011;19:19551–61.
- [198] Zlenko AS, Dvoyrin VV, Mashinsky VM, Denisov AN, Iskhakova LD, Mayorova MS, et al. Furnace chemical vapor deposition bismuth-doped silica-core holey fiber. *Opt Lett* 2011;36:599–601.
- [199] Hasegawa T. Design and fabrication of bismuth-silicate photonic crystal fiber. *Opt Commun* 2012;285:3939–44.
- [200] Thomas GA, Shraiman BI, Glodis PF, Stephen MJ. Towards the clarity limit in optical fibre. *Nature* 2000;404:262–4.
- [201] Morimoto S, Fujii M, Sun HT, Miwa Y, Imakita K, Qiu JR, et al. Broadband near-infrared emission from bismuth-doped multilayer films. *J Appl Phys* 2012;112:073511.
- [202] Dai NL, Luan H, Xu B, Yang LY, Sheng Y, Liu Z, et al. Effect of Si doping on near-infrared emission and energy transfer of bismuth in silicate glasses. *J Non-Cryst Solids* 2011;358:261–4.
- [203] Lim YT, Kim S, Nakayama A, Stott NE, Bawendi MG, Frangioni JV. Selection of quantum dot wavelengths for biomedical assays and imaging. *Mol Imaging* 2003;2:50–64.
- [204] Velázquez M, Ferrier A, Doualan J-L, Moncorgé R. In: Al-Khursan Amin, editor. Rare-earth-doped low phonon energy halide crystals for mid-infrared laser sources, solid state laser. InTech. ISBN 978-953-51-0086-7 <<http://www.intechopen.com/books/solid-state-laser/rare-earth-doped-lowphonon-energy-halide-crystals-for-mid-infrared-laser-sources>>.
- [205] Doualan J-L, Moncorgé R. Laser crystals with low phonon frequencies. *Ann Chim Sci Mater* 2003;28:5–20.
- [206] Isaenko L, Yeliseyev A, Tkachuk A, Ivanova S. New monocrystals with low phonon energy for mid-IR lasers. In: Ebrahim-Zadeh M, Sorokina IT, editors. Mid-infrared coherent sources and applications. New York: Springer; 2008. p. 3–65.

- [207] Egger P, Burkhalter R, Hulliger J. Czochralski growth of $\text{Ba}_2\text{Y}_{1-x}\text{Er}_x\text{Cl}_7$ ($0 < x \leq 1$) using growth equipment integrated into a dry-box. *J Cryst Growth* 1999;200:515–20.
- [208] Kaminska A, Cybińska J, Zhydachevskii Ya, Sybilska P, Meyer G, Suchocki A. Luminescent properties of ytterbium-doped ternary lanthanum chloride. *J Alloy Compd* 2011;509:7993–7.
- [209] Nitsch K, Cihlář A, Malková Z, Rodová M, Vaněček M. The purification and preparation of high-purity lead chloride and ternary alkali lead chloride single crystals. *J Cryst Growth* 1993;131:612–5.
- [210] Nitsch K, Dušek M, Nikl M, Polák K, Rodová M. *Prog Cryst Growth Charact* 1995;30:1–22.
- [211] Nitsch K, Cihlář A, Nikl M, Rodová M. Growth of lead bromide and ternary alkali lead bromide single crystals. *J Electr Eng* 1995;46:82–4.
- [212] Nitsch K, Cihlář A, Rodová M. Molten state and supercooling of lead halides. *J Cryst Growth* 2004;264:492–8.
- [213] Nitsch K, Rodová M. Influence of thermal treatment on supercooling of molten potassium lead chloride. *J Electr Eng* 1999;50:35–7.
- [214] Okhrimchuk AG, Butvina LN, Dianov EM, Lichkova NV, Zagorodnev VN, Boldyrev KN. Near-infrared luminescence of $\text{RbPb}_2\text{Cl}_5:\text{Bi}$ crystals. *Opt Lett* 2008;33:2182–4.
- [215] Ruan J, Su LB, Qiu JR, Chen DP, Xu J. Bi-doped BaF_2 crystal for broadband near-infrared light source. *Opt Express* 2009;17:5163–9.
- [216] Su LB, Zhao HY, Li HJ, Zheng LH, Ren GH, Xu J, et al. Near-infrared ultrabroadband luminescence spectra properties of subvalent bismuth in CsI halide crystals. *Opt Lett* 2011;36:4551–3.
- [217] Su LB, Zhao HY, Li HJ, Zheng LH, Fian X, Jiang XT, et al. Near-infrared photoluminescence spectra in Bi-doped CsI crystal: evidence for Bi-valence conversions and Bi ion aggregation. *Opt Mater Express* 2012;2:757–64.
- [218] Li C, Song ZG, Qiu JB, Yang Z, Yu X, Zhou D, et al. Broad band yellow–white and near infrared luminescence from Bi-doped $\text{Ba}_{10}(\text{PO}_4)_6\text{Cl}_2$ prepared in reductive atmosphere. *J Lumin* 2012;132:1807–11.
- [219] Romanov AN, Veber AA, Fattakhova ZT, Usovich OV, Haula EV, Trusov LA, et al. Subvalent bismuth monocation Bi^+ photoluminescence in ternary halide crystals KAlCl_4 and KMgCl_3 . *J Lumin* 2013;134:180–3.
- [220] Veber AA, Romanov AN, Usovich OV, Fattakhova ZT, Haula EV, Korchak VN, et al. *Appl Phys B: Laser Opt* 2012;108:733–6.
- [221] Sun HT, Hosokawa A, Miwa Y, Shimaoka F, Fujii M, Mizuhata M, et al. Strong ultra-broadband near-infrared photoluminescence from bismuth-embedded zeolites and their derivatives. *Adv Mater* 2009;21:3694–8.
- [222] Sun HT, Miwa Y, Shimaoka F, Fujii M, Hosokawa A, Mizuhata M, et al. Superbroadband near-IR nano-optical source based on bismuth doped high-silica nanocrystalline zeolites. *Opt Lett* 2009;34:1219–21.
- [223] Sun HT, Fujii M, Sakka Y, Bai ZH, Shirahata N, Zhang LY, et al. Near infrared photoluminescence and Raman characterization of bismuth embedded sodalite nanocrystals. *Opt Lett* 2010;35:1743–5.
- [224] Sun HT, Sakka Y, Miwa Y, Shirahata N, Fujii M, Gao H. Spectroscopic characterization of bismuth embedded Y zeolites. *Appl Phys Lett* 2010;97:131908.
- [225] Sun HT, Hasegawa T, Fujii M, Shimaoka F, Bai Z, Mizuhata M, et al. Significantly enhanced superbroadband near infrared emission in bismuth/aluminum doped high-silica zeolite derived nanoparticles. *Opt Express* 2009;17:6239–44.
- [226] Denisov VN, Ivlev AN, Lipin AS, Mavrin BN, Orlov VG. Raman spectra and lattice dynamics of single-crystal $\alpha\text{-Bi}_2\text{O}_3$. *J Phys Condens Matter* 1997;9:4967–78.
- [227] Bai ZH, Sun HT, Hasegawa T, Fujii M, Shimaoka F, Miwa Y, et al. Efficient near-infrared luminescence and energy transfer in erbium/bismuth codoped zeolites. *Opt Lett* 2010;35:1926–8.
- [228] Bai ZH, Sun HT, Fujii M, Miwa Y, Hasegawa T, Mizuhata M, et al. Bismuth-sensitized efficient near-infrared luminescence from ytterbium in zeolites. *J Phys D: Appl Phys* 2011;44:155101.
- [229] Bai ZH, Fujii M, Mori Y, Miwa Y, Mizuhata M, Sun HT, et al. Efficient near-infrared emission from neodymium by broadband sensitization of bismuth in zeolites. *Opt Lett* 2011;36:1017–9.
- [230] Bai ZH, Fujii M, Mori Y, Miwa Y, Mizuhata M, Sun HT, et al. Efficient near-infrared luminescence and energy transfer in Nd–Bi codoped zeolites. *Mater Res Soc Symp Proc* 2011;1342:61–6.
- [231] Su LB, Zhou P, Yu J, Li HJ, Zheng LH, Wu F, et al. Spectroscopic properties and near-infrared broadband luminescence of Bi-doped SrB_2O_7 glasses and crystalline materials. *Opt Express* 2009;17:13554–60.
- [232] Su LB, Yu J, Zhou P, Li HJ, Zheng LH, Yang Y, et al. Broadband near-infrared luminescence in γ -irradiated Bi-doped $\alpha\text{-BaB}_2\text{O}_4$ single crystals. *Opt Lett* 2009;34:2504–6.
- [233] Xu J, Zhao HY, Su LB, Yu J, Zhou P, Tang HL, et al. Study on the effect of heat-annealing and irradiation on spectroscopic properties of Bi: $\alpha\text{-BaB}_2\text{O}_4$ single crystal. *Opt Express* 2010;18:3385–91.
- [234] Peng MY, Sprenger B, Schmidt MA, Schwefel HGL, Wondraczek L. Broadband NIR photoluminescence from Bi-doped $\text{Ba}_2\text{P}_2\text{O}_7$ crystals: insights into the nature of NIR-emitting bismuth centers. *Opt Express* 2010;18:12852–63.
- [235] Xu BB, Zhou DZ, Guan MJ, Teng Y, Zhou JJ, Qiu JR, et al. Broadband near-infrared luminescence from γ -ray irradiated bismuth-doped 4YGeO_3 crystals. *J Electrochem Soc* 2011;158:G203–6.
- [236] Zhou SF, Dong HF, Zeng HP, Hao JH, Chen JX, Qiu JR. Infrared luminescence and amplification properties of Bi-doped $\text{GeO}_2\text{-Ga}_2\text{O}_3\text{-Al}_2\text{O}_3$ glasses. *J Appl Phys* 2008;103:103532–5.
- [237] Chi G, Zhou DC, Song ZG, Qiu JB. Effect of optical basicity on broadband infrared fluorescence in bismuth-doped alkali metal germanate glasses. *Opt Mater* 2009;31:945–8.
- [238] Seo YS, Fujimoto Y, Nakatsuka M. Optical amplification in a bismuth-doped silica glass at 1300 nm telecommunications window. *Opt Commun* 2006;266:169–71.
- [239] Ren JJ, Qiao YB, Zhu CS, Jiang XW, Qiu JR. Optical amplification near 1300 nm in bismuth-doped strontium germanate glass. *J Opt Soc Am B* 2007;24:2597–600.
- [240] Ruan J, Wu E, Zeng HP, Zhou SF, Lakshminarayana G, Qiu JR. Enhanced broadband near-infrared luminescence and optical amplification in Yb-Bi codoped phosphate glasses. *Appl Phys Lett* 2008;92:101121–3.
- [241] Razdobreev I, Bigot L, Pureur V, Favre A, Bouwmans G, Douay M. Efficient all-fiber bismuth-doped laser. *Appl Phys Lett* 2007;90:031103–5.
- [242] Firstov SV, Shubin AV, Khopin VF, Mel'kumov MA, Bufetov IA, Medvedkov OI, et al. Bismuth-doped germanosilicate fiber laser with 20-W output power at 1460 nm. *Quant Electron* 2011;41:581–3.

- [243] Dianov EM. Bismuth-doped optical fibers: a challenging active medium for near-IR lasers and optical amplifiers. *Light: Sci Appl* 2012;1. <http://dx.doi.org/10.1038/lsci.2012.1>.
- [244] Dianov EM, Krylov AA, Dvoyrin VV, Mashinsky VM, Kryukov PG, Okhotnikov OG, et al. Mode-locked Bi-doped fiber laser. *J Opt Soc Am B* 2007;24:1807–8.
- [245] Dvoyrin VV, Mashinsky VM, Dianov EM. Yb–Bi pulsed fiber lasers. *Opt Lett* 2007;32:451–3.
- [246] Summary report of bismuth subnitrate, subcarbonate, subgallat, subsalicylate from Committee for Veterinary Medical Products (CVMP). <<http://www.ema.europa.eu/pdfs/vet/mrls/020197en.pdf>>.
- [247] Chen L, Lin CC, Yeh CW, Liu RS. Light converting inorganic phosphors for white light-emitting diodes. *Materials* 2010;3:2172–95.
- [248] Xu BB, Tan DZ, Zhou SF, Hong ZL, Sharafudeen KN, Qiu JR. Enhanced broadband near-infrared luminescence of Bi-doped oxyfluoride glasses. *Opt Mater Express* 2012;20:29105–10.
- [249] Li C, Li YJ, Wang X, Wang Q, Song ZG, Qiu JB, et al. Study on the effect of apatite structure on spectroscopic properties of bismuth activated alkaline earth metal chlorophosphate [M₅(PO₄)₃Cl; M = Ca, Sr and Ba]. *Mater Chem Phys* 2013;139:220–4.
- [250] Sun HT, Sakka Y, Shirahata N, Yonezawa T. Near-infrared photoluminescence from molecular crystals containing tellurium. *J Mater Chem* 2012;22:24792–7.
- [251] Dianov EM, Alyshev SV, Shubin AV, Khopin VF, Gur'yanov AN. IR luminescence of tellurium-doped silica-based optical fibre. *Quant Electron* 2012;42:189–91.